The University of Osaka
Institutional Knowledge Archive

Title	Short-term Predictions of Added Resistance in Waves Considering Wave Steepness Nonlinearity with Probability Density Function Method
Author(s)	Jawa, Sahil
Citation	大阪大学, 2023, 博士論文
Version Type	VoR
URL	https://doi.org/10.18910/92967
rights	
Note	

The University of Osaka Institutional Knowledge Archive : OUKA

https://ir.library.osaka-u.ac.jp/

The University of Osaka

DOCTORAL THESIS

Short-term Predictions of Added Resistance in Waves Considering Wave Steepness Nonlinearity with Probability Density Function Method

（波岨度影響を考慮した確率密度関数法による波浪中抵抗増加の短期予測）

Sahil Jawa

June 2023

Dept. of Naval Architecture & Ocean Engineering
Division of Global Architecture
Graduate School of Engineering
OSAKA UNIVERSITY

Short-term Predictions of Added Resistance in Waves Considering Wave Steepness Nonlinearity with Probability Density Function Method

(1) Development of mathematical model based on probabilistic theory, (2) an estimation of added resistance in which the non-linear effect of wave height can be applied with the proposed probability density function method, (3) this statistical model has been validated by the estimation of added resistance through tank tests and direct CFD numerical simulations in irregular head and oblique sea conditions.

Sahil Jawa, 2023

Supervisor: Professor Munehiko Minoura, Ocean Space Development Subarea, Osaka University

Review Committee:

Professor Atsuo Maki, Ship Intelligentization Subarea, Osaka University

Professor Munehiko Minoura, Ocean Space Development subarea, Osaka University

Professor Hiroyoshi Suzuki, Marine Hydro-Science and Engineering, Osaka University

Doctoral Dissertation

Department of Naval Architecture & Ocean Engineering

Division of Global Architecture

Graduate School of Engineering

Osaka University

2-1 Yamadaoka, Suita, Osaka 565-0871

大阪大学 OSAKA UNIVERSITY

Abstract

The added resistance in waves, which is an important component in the estimation of actual sea performance of ships, is evaluated as the average value by short-term prediction methods. There is a spectrum method as a method for estimating the added resistance in waves. As ship becomes larger, the influence of short wavelength region increases, and it tends to have higher wave steepness. According to linear theory, the added resistance in waves is proportional to square of the wave height, but in reality, it deviates from linear theory and linear superposition principal cannot be applied. Hence, a novel probabilistic method is established to account for non-linearities of added resistance with respect to wave height in short-term sea conditions with the aim of contributing to the accurate evaluation of ship safety and economy. We establish a method named Probability Density Function (PDF) method for estimating the added resistance in irregular waves using the joint occurrence probability distribution of wave height and period based on modified Longuet-Higgins model and added resistance response in the frequency region. It is a method of averaging the combination of crest and trough that ships encounter in irregular waves, which is considered as one wave of the stationary regular waves, and the resulting added resistance is combined stochastically based on the proposal by Hsu method. The non-linearity with respect to wave height is empirically expressed as a "correction coefficient", the relative ratio of nonlinearity to linearity, which is obtained from the comparison of CFD data at few representative frequencies. The comparison was made between the conventional spectrum method and PDF method. The results of the proposed non-linear PDF method have a reasonable agreement in the acceptable range of accuracy with results of RANSE based CFD numerical simulations and the experimental model tests in long crested irregular head waves. Moreover, ships rarely travel in head waves in actual seas as this condition encounter highest added resistance in waves. Thus, short term predictions of added resistance in oblique waves with taking into account the wave steepness non-linearity are obtained with PDF method to properly evaluate a hull form design and to get a realistic idea of its behavior during the actual sailing. Obtained results are compared with the spectrum method and is validated using direct estimation of added resistance using CFD in oblique irregular waves. As a result, the proposed method is applicable for obtaining the added resistance in irregular head and oblique waves having the non-linearity with respect to wave height with a scope of further improvement in the method. Furthermore, in this paper, we have discussed the multivariate joint probability occurrence of a single wave encountered under stationary sea conditions and the ship's response to the wave and verification by numerical analysis. Chapter 7 and 8 summarize this study.

Acknowledgements

This thesis work is accomplished in the International Program of Maritime and Urban Engineering of Osaka University, which is fully supported by the Japan International Cooperation Agency (JICA) Innovative Asia program It is submitted in the fulfilment of the Doctor of Philosophy at the Department of Naval Architecture and Ocean Engineering, Osaka University, Japan. I dedicated to those who have supported me along the Ph.D. Journey.

First and foremost, I would like to thank from the bottom of my heart and show gratitude to my supervisor, Professor Munehiko Minoura, whose expertise, perseverance, and vision made the completion of this dissertation possible in the end and gave me the chance to pursue my doctoral research under his supervision. I am indebted too much for his generosity and kindness during my study. He guided me with some good research papers for deeper understanding of the topic. He cared a lot about my research progress, the difficulties I faced and also helped in solving problem with his innovative ideas and gave me additional time in our discussion meetings. His ideas and his writing skills made me possible to publish good quality of research papers. I am so grateful to have him as my supervisor. I also admire his support and continuous encouragement for participating in the international conferences. I want to thank him for helping me complete the graduation requirements on time and replying to my emails whenever I need him for discussion on my doubts. Without his guidance and persistent help, this dissertation would not have been possible.

I would also like to give thanks to Professor Takahito Iida as Assistant Professor, who kindly gave constructive advice during laboratory meetings and helped me whenever I had any doubts. Further, I would like to thank Mr. Idomoto San, working in Imabari shipbuilding who has guided me in the initials days of learning the commercial software FINE/Marine used in my research. I would like to thank Ms. Tamae Miyabe who helped me in the administrative things.

I would like to thank Sreenath Subramaniam with whom I had a lot of discussions regarding research and job hunting. His motivation and constructive comments on my doubts were really helpful. Also, I could participate in seminars with students from other majors to experience the knowledge and inspiration gained from interdisciplinary learning in cross boundary seminars. These seminars are organized under the International Program of Maritime and Urban Engineering of Osaka University.

I am also indebted to all the lab mates who involved in my towing tank experiments conducted at Osaka University tank facility. I am delighted to belong to a fantastic laboratory with enjoyment and supporting members. I should appreciate considerably the positive atmosphere of pursuing a doctorate study. For all lab members and university colleagues, I would like to thank for the lively friendship. At the end of the foremost important, I am always indebted to my dearest parents, my sister for constant support. I also thank Momoko Tsuji for her constant support and making my life easier and full of fun in Japan. I sincerely thank everyone without exception.

June 2023, Osaka

Sahil Jawa

Contents

List of Figures

List of Tables

Symbols

In **chapter 2**,

L_{OA}	Overall ship length
L_{pp}	Length between perpendiculars
ΔT	Sampling time
ω	Wave frequency
ω_p	Peak wave frequency
Fn	Froude number
$H_{1/3}$	Significant wave height
T_{01}	Mean wave period
$H_{1/3m}$	Significant wave height
T_{01m}	Mean wave period
FFT	Fast Fourier Transformation
RIOS	Research Initiate on Oceangoing Ships
$S(\omega)$	Wave spectrum
$S(\omega_e)$	Encounter wave spectrum
γ	Spectral peak enhancement factor
α	Dimensionless constant
σ	Spectral peak width parameter.
τ	Constant
μ_s	Wave encounter angle with ship

In **chapter 3**,

$k-\omega$	k–omega (k–ω) turbulence model
L_{ref}	Reference length
dx	Mesh cell size in longitudinal direction
dz	Mesh cell size in vertical direction
H_{wm}	Model scale wave height
λ_m	Model scale wavelength
T_e	Encounter wave period

H_{ws}	Actual ship scale wave height
R_{aw}	Added resistance in regular waves
R_{Total}	Total resistance in regular waves
R_{Calm}	Calm water resistance
λ_E	Effective wavelength
β	Oblique wave angle
ζ_3	Heave motion amplitude
θ	Pitch motion amplitude
ψ	Roll motion amplitude
$C(s,V)$ or $C(s)$	Correction coefficient
s	Wave steepness
g	Gravity
V	Ship speed
K_{aw}	Added resistance coefficient
ζ_a	Wave amplitude

In **chapter 4**,

T_{pm}	Model scale peak wave period
m_n	n^{th} order Spectral moment
m_0	Zeroth order spectral moment
m_1	Ist order spectral moment
Δt	Time step size
K	Spring constant
T_0	Spring initial tension

In **chapter 5**,

H	Wave height of one wave
T	Time period of one wave
$H_{1/3}$	Significant wave height
T_{01}	Mean wave period
T_{02}	Zero up crossing mean wave period

$\rho(t)$	Envelope wave height
$\phi(t)$	Phase shift
ω_m	Mean wave frequency
$x(t)$	Stochastic process
$H(t)$	Instantaneous wave height
$T(t)$	Instantaneous Wave Period
$f(\zeta, \eta)$	Objective probability density function
ν	Spectral width parameter
ζ	Dimensionless wave height
η	Dimensionless wave height
ε_n	Uniform random phase
$C_{xx}(\tau)$	Autocorrelation function
$S_{xx}(\omega)$	Power spectrum of the wave
ω_c	Certain wave frequency
x_c	Cosine wave component
$\dot{x}_c$	Time derivative of Cosine wave component
x_s	Sin wave component
$\dot{x}_s$	Time derivative of sin wave component
$\mathbf{\Sigma}$	Covariance matrix
$\rho(t)$	Instantaneous wave amplitude
$f(\zeta)$	Probability density function of wave height
$f(\eta)$	Probability density function of wave period
L	Normalizing factor for original L-H model
L_p	Normalizing factor for modified L-H model by peak period
L_c	Normalizing factor for modified L-H model by peak period and spread reduction
η_p	Peak period of the wave spectrum
η_{02}	Mean period due to the wave spectrum
η_m	Mean wave period by the probability density function
α	Correction factor for peak period
β	Correction factor for tail spread distribution

In **chapter 6**,

ω_{em}	Mean wave frequency of the encounter wave

$y(t)$	Wave equation
K	Wave number at infinite depth
θ	Encounter angle between the ship and the wave
$z(t)$	Motion displacement of the advancing ship
$H(\omega)$	Frequency response function of the motion to the wave
H_a	Response amplitude and
ψ_{n}	Phase lag
ζ_y	Instantaneous dimensionless wave height
ζ_z	Instantaneous dimensionless ship motion height
$I_0(z)$	Zeroth order Modified Bessel function
$f(\zeta_y, \zeta_z)$	Objective probability density function

In **chapter 7**,

T_L	Non-dimensionalized wave period

Chapter 1

Introduction

In actual seas, ships are always affected by the waves and there is a growing demand for a highly accurate evaluation of the actual sea performance of ships taking into account the effect of waves in resistance calculations from the viewpoint of the operational economy and environmental protection. The added resistance has a substantial effect on the engine or propulsion system selection and ship's performance in terms of sustain a service speed optimizing fuel consumption in a realistic seaway. Although many studies have been conducted to improve fuel consumption of ships in seaway to meet the requirement for minimum energy efficiency level measured by an Energy Efficiency Design Index (EEDI) and Energy Efficiency Operational Indicator (EEOI) which are regulated by the International Maritime Organization's (IMO) Marine Environment Protection Committee (MEPC). But the current problem is the estimated added resistance in short wavelength region, where actual ships navigates, deviates from experimental data. According to EEDI under the mandate by 2025 regulations, it aims to improve the efficiency of 30% of the damage to the ship due to environmental loads such as winds and waves. As zero emissions are the goal for marine vessels in the future, it is essential to accurately estimate the added resistance when navigating in actual seas. Fig. 1.1 (a), (b) shows the containership travelling in calm water and in real ocean random waves.

FIGURE 1.1: (a) Ships navigating in calm water (b) Ship navigating in random waves

Many approaches have been developed to predict and estimate the added resistance such as using experimental fluid dynamics (EFD) and potential flow (PF) and lately computational fluid dynamics (CFD). It is very important to introduce new development methods for designing precise marine performance in actual seas. Also, accurate predictions of the added resistance are necessary for the implementation of the modern on-board ship routing systems. The added resistance's value is relatively small when compared to the amplitude of the excitation force because it is of second order nature and is dependent on the mean value of wave force as shown by Faltinsen, 1990 [8]. Thus, a high degree of accuracy is required both in the experiments and calculations. On the other hand , the studies of added resistance has revealed that it is dependent on factors such as ship motion, ship speed, wave duration, wave height, wave heading, hull form, bow shape, and bow relative motion. The motivation to write this thesis stems from the wish of the author to consolidate his knowledge in seakeeping in particular getting deep into the added resistance in waves investigating the wave height effect phenomena using stochastic, CFD and EFD methods. This thesis provide uniform and concise theory on stochastic analysis and probabilistic predictions of random ocean waves. The scope of the thesis is to seek to apply a series of improvements to the representation of the joint distribution of wave heights and periods in deep water. Authors tried to modify the Longuet-Higgins model by allowing a more realistic mathematical description of the random ocean waves in terms of estimating precise added resistance in irregular waves. Authors also discussed about the probability of simultaneous occurrence of wave and ship motion response.

1.1 Background

Conventionally the added resistance in irregular waves has been treated by spectral analysis using added resistance transfer function and wave spectrum that corresponds to statistical values in a short term. Meaning using the estimation of frequency response transfer function of added resistance in regular waves, the total amount is predicted by the moment of response spectrum criterion for calculating added resistance in short-term sea conditions. This is correct in the linear approach based on potential theory using linear superposition principal. Most of the studies have focused on calculating the added resistance transfer function accurately in regular waves. Seo et al. (2014)[45] predicted the added resistance using potential-based methods. However, due to its limitations which make it difficult in considering the nonlinearity and viscosity effects. In particular, the added resistance in waves is greatly affected by the hydrodynamic force acting near the waterline at the bow, but the hull form above the waterline is not considered in the linear theory. So, this approach does not reflect wave-body interactions above the waterline, an important aspect in considering nonlinear hydrodynamic effects.

In short waves, typical potential flow methods fail due to a variety of reasons. If a typical strip/slender body theory is applied to solve the seakeeping problem, the abrupt hull form changes in the bow region cannot be captured correctly, and this is a reason for the underestimation. Predictions using EUT method by Kashiwagi (1992)[20] 3D panel methods have often shown significant improvement. However, even then, there is a considerable underestimation when applying these methods discussed by Liu et al. (2011)[29] to the prediction of the added resistance. Another issue in this respect is beyond the basic assumptions of potential flow theory, namely the wave breaking/viscous effect. As confirmed recently by several experimental studies by Valanto & Hong (2015)[50] and laborious CFD calculations by Ley et al (2014)[28], viscous effects appear to play a significant role in the prediction of added resistance in very short waves. In tank tests, the accurate measurement of the added resistance in short waves is a big challenge due to the very small, measured values, breaking wave/spray phenomena etc. This leads the tank operators to use steeper incident short waves for respective measurements, which may put the quadratic dependency of the added resistance on wave height under question.

In this respect, many researchers have tried to include the effect of wave height in the prediction of added resistance in actuals seas like Lang and Mao (2020)[25] also tried to propose a non -linear wave height correction factor in terms of significant wave height in the conventional formula. He infused the factor by integrating wave spectrum with the semi-empirical added resistance in regular waves (based on potential theory results), to estimate the nonlinear increase of fuel consumption when a ship is sailing in harsh sea environments. Kobayashi (2007)[20] and Kuroda et al. (2016)[23] tried to construct the time histories of added resistance in irregular seas by using the higher-order approximation response model in regular waves. Despite this model being partially satisfactory in mild sea conditions, discrepancies were inevitable in high wave heights or harsh seas. It has been examined through experimental studies by Lee et al. (2017)[27] that the added resistance transfer function is dependent on the wave steepness of regular waves and shows non-linearity with respect to wave height. Yasukawa et al. (2016)[10] conducted model tests in regular waves at two different wave heights as well as in irregular waves. They measured the quadratic transfer function of the wave added resistance for three ship models. Their results clearly demonstrate that nonlinearity is important especially for $\lambda/L_{pp} < 0.7$ and the added resistance is proportional to power of wave height less than two for these wavelengths. Hence, the spectral analysis is incomplete enough to estimate the added resistance in actual irregular seas appropriately and that the quadratic transfer function of wave added resistance is dependent on wave height. Sigmund et al. (2018)[47] also investigated the effect of the wave steepness on the added wave resistance coefficient for the containership (DTC) and the tanker (KVLCC2) using CFD. The investigation shows similar trends that were shown using experimental study by Yasukawa et al. (2016)[10] except for very short wavelength case $\lambda/L_{pp} < 0.5$ where the added wave resistance coefficient has strong influence by the high wave steepness in very short waves and decreased with decreasing wave steepness. Yoo et al., (2020)[53] carried out the experimental and CFD studies to estimate the added resistance in irregular waves and compared it with the conventional spectrum method. The study demonstrated that the spectrum method underestimates the values and proved the necessity of direct estimation of added resistance in irregular waves to account the non-linear interaction between the ship and waves. Similarly, Lee et al., (2022)[25] showed that direct estimation of average added resistance in irregular waves differs from the spectrum method results.

The cross-Bispectral analysis proposed by Dalzell (1974)[2] is effective for analyzing the nonlinear effects related to wave height and wave steepness as second-order nonlinear responses, but it is difficult to ensure accuracy practically because it requires long measurement data. On the other hand, Hirayama and Wang (1993)[9], based on Hsu's method (1970)[11], analyzed the added resistance in irregular waves by regarding irregular waves as continuous half-waves of regular waves. It was shown that the analytical results generally agree with the results obtained from the added resistance in regular waves in the linear region with small wave heights and small wave steepness. Unlike the spectrum analysis method, this method specifies the wave height and the wave steepness, so that the added resistance in irregular waves can be formulated considering the nonlinearity of them. Jawa et al. (2022)[15] proposed a probability density function method based on the mathematical model by Hirayama et al. (1993) [9] and Hsu (1970) [11] in the estimation of added resistance in irregular waves to incorporate the non-linear effect of wave height. But results showed discrepancy with the conventional method based on spectral analysis i.e., wave period of the maximum added resistance was evaluated longer than the result of the spectrum method. Further improvement in the method was needed.

1.2 Methodology flowchart

This section describes about the detailed research methodology used in this paper. The process of examining the short-term prediction of non-linear added resistance is divided into five main steps: 1) goal and scope, 2) Experimental analysis in the Towing tank 3) numerical modelling, 4) CFD Simulations results 5) Prediction of average added resistance in irregular waves by non-linear PDF method and validate the method by the CFD and experimental results directly in irregular waves. The outline of each step is presented in Fig. 1.2.

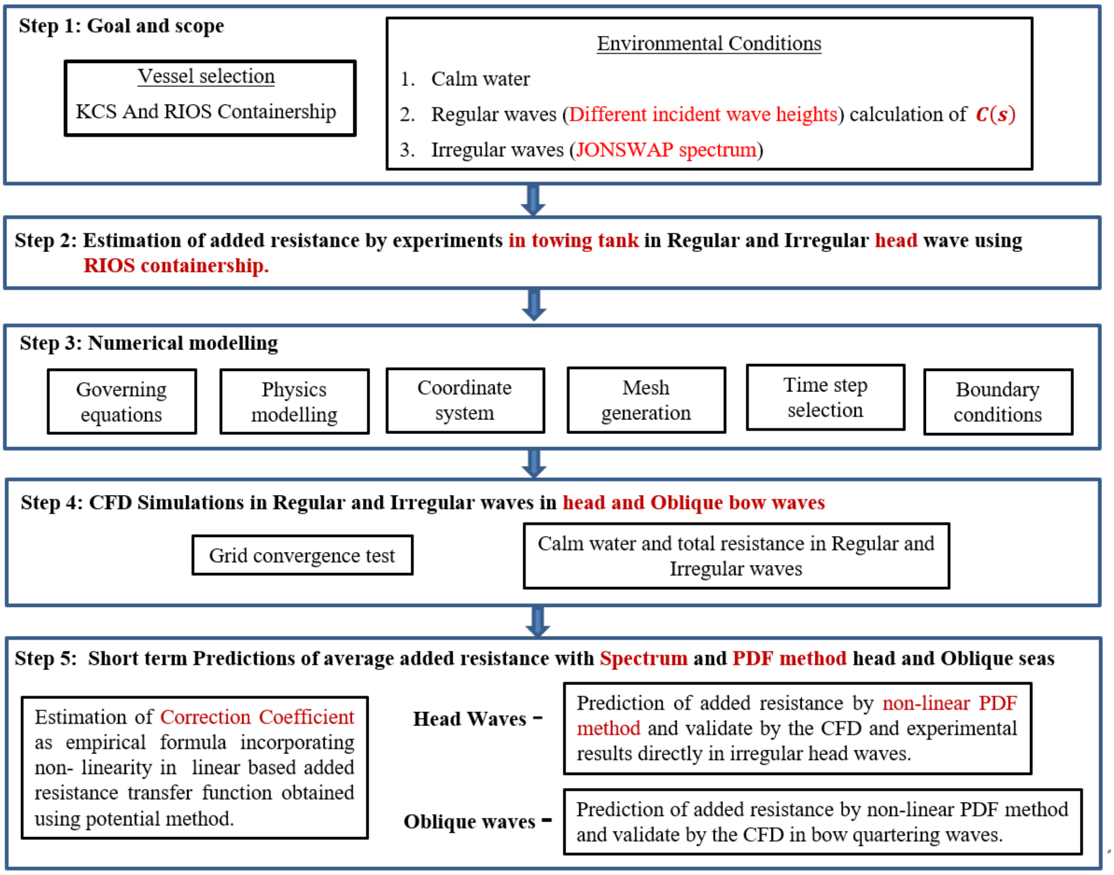

FIGURE 1.2: Flow chart showing the methodology adopted in the study.

The first step describes the research aim and objectives studied to achieve them. The hull of two types KCS and RIOS containership are selected in this study. The second step is the experimental analysis of average added resistance conducted in the towing tank in the regular and irregular waves with RIOS containership. The third step explains about the details of the numerical simulation set up applied to added wave resistance calculations to the CFD physical model including governing equations, mesh generation, time step selection, etc. In the fourth step describes about grid convergence study and wave calibration tests done in regular and irregular head and oblique waves and obtaining the added wave calculation results from the obtained time series data of total resistance and calm water resistance and the last step 5 is the using the non-linear correction coefficient from the added wave resistance CFD data in the regular waves and finally compare the short term prediction results of average wave added resistance (in the irregular wave field scenario) through conventional spectral method and PDF method which includes on-linearity due to wave height and validate the non-linear PDF method by the CFD and experimental results directly estimated in head and oblique irregular waves.

1.3 Objectives

Commercial ships frequently operate under irregular sea conditions; hence, their performance must be estimated through simulations in a more realistic environment. As ships becomes larger, the influence of short wavelength region increases. According to linear theory, the added resistance in waves is proportional to square of the wave height, but it has pointed out it deviates from linear theory and linear superposition principal cannot be applied. Since the conventional spectrum method is not applicable for nonlinear responses that can include nonlinearities that occur due to wave height. Therefore, we have proposed and validated a new mathematical model in which the wave height is explicitly considered so that the effect of nonlinearity due to wave height can be taken into account when calculating added resistance in actual seas.

Due to its wide use for research purposes, the KCS and RIOS vessel has been selected as a test case for this study. Furthermore, the RIOS vessel has recently been tested towing tank as well as with RIOS system motions inhouse potential theory-based solver. In the present study, wave height effect on the added resistance in waves is investigated in head and oblique sea regular waves by the CFD RANSE method and experiments in towing tank on RIOS (http://www.rios.eng.osaka-u.ac.jp) containership under the different wave heights. That effect illustrates the characteristic of nonlinearity with respect to wave height in added resistance calculations and is shown as a ratio of added resistance at higher wave heights to linear condition at small wave height and small wave steepness. Next, a mathematical model for estimating added resistance with specified wave heights to which this nonlinear characteristic can be applied is based on statistical theory. This statistical model has been validated by the direct estimation of added resistance through tank tests and CFD numerical simulations in irregular head and oblique sea conditions.

In Chapter 2, the experimental set up conducted in 2022 using the RIOS (Research Initiative on Oceangoing Ships) containership in the towing tank facility of Osaka University is described. The analysis of motion free tests is performed for 3 degree of freedom ship motions to estimate the added resistance in regular and irregular head waves of RIOS containership to validate the proposed probabilistic theoretical short term prediction model. Long crested irregular waves are generated using the JONSWAP wave spectrum and compare with the measured values for most of the investigated sea states. Comparison between target and realized wave spectra is shown and satisfied to confirm the measurement accuracy. Experiments has been performed for different significant wave heights to estimate and validate the wave steepness non-linearity in added resistance calculations with the proposed non-linear Pdf method.

In Chapter 3, wave height effect on the added resistance in waves is investigated in head and oblique regular waves by the CFD RANSE method. Numerical modelling and boundary conditions for CFD numerical simulations for estimation of added resistance in regular waves and irregular waves are outlined. All the numerical simulations are performed using a commercial CFD software, FINE/Marine V 8.2. [36], which is based on the ISIS-CFD flow solver developed at Ecole Centrale de Nantes (ECN). The simulation set-up refers to the recommended value in the user manual of FINE/Marine for the computation in the present study. Firstly, the simulations are performed in regular waves on 5 servers of HPC system of 32 cores each to estimate the added resistance in regular waves of different incident wave heights at different wavelengths and based on the results, the non-linear correction coefficient is determined, the relative ratio of nonlinearity to linearity, which is calculated at a few representative frequencies. This wave height effect illustrates the characteristic of nonlinearity with respect to wave height in added resistance calculations and is shown as a ratio of added resistance at higher wave heights to linear condition at small wave height and small wave steepness. Simulation set up and calculation of non-linear correction has been discussed in this chapter thoroughly.

In Chapter 4, the direct estimation of added resistance in irregular waves using CFD RANSE based method is being outlined to validate the proposed statistical theory. The RANSE method has an advantage of including non-linearity due to wave height observed in irregular waves and supposed to consider their interactions that is the severe coupled ship motions in harsher sea conditions. Prior to the investigation of the added resistance using the CFD numerical setup, mesh independency tests are performed to capture the accurate wavelength and free surface elevation. A series of calibrations are performed to satisfy the input wave spectrum with the energy distribution of target wave spectrum by the parametric study of grid refinement and time step. After obtaining the optimum grid size and time step to be used to generate irregular waves accurately, then all the computations are performed equivalent to towing tank experiments set up. It is solved for 3 degrees of freedom (heave, pitch, and surge motion) using virtual spring attached with the hull with the help of user defined function in the dynamic library which made the computational setup complex. Hence, the overset mesh technique is used in the irregular wave cases to calculate the added resistance results more accurately and compared with experimental results.

In Chapter 5, The modified versions of the linear theoretical model of Longuet-Higgins (1975, 1983)[30][31] are derived in this work and also compared with the numerical simulations of time series model of waves under linear assumptions from the given wave spectrum. The main feature of modifications is to replace the mean wave period with the modal wave period (wave spectrum peak period) on the Zhang et al.'s (2016)[55] model and further improvement is done by reducing the tail spread of the probability distribution to get the reasonable added resistance results in irregular waves. This chapter gives a short review and concise derivation on the theoretical models adopted in the paper.

In Chapter 6, the multivariate joint probability occurrence of a single wave encountered under stationary sea conditions and the ship's response to the wave is discussed. Determination of the joint probability density function of the wave height encountered by the ship and the ship response expressed by a multivariate Rayleigh probability distribution. First, the relationship between the spectrum of waves and ship motion spectra and their time series model is determined, and then the relationship between the time series model and the joint probability density function is determined. Furthermore, we determined the numerical solution by successive integration of the probability density function of wave carrier model and heave motion response. This proposed multivariate probability density function is further verified by the necessary numerical analysis related to the superposition model for time-series generation of wave height and heave motion height for containership was carried out according to the zero-up crossing definition to determine the occurrence frequency of the ship motion height in conjunction with the wave height. It is confirmed that the ship response motions are synchronized as the average wave period increased.

In Chapter 7, describe the proposed new mathematical model based on the original and modified statistical models proposed in this thesis in different random sea states by integrating the linear added resistance responses. The wave height effect is explicitly considered so that the effect of nonlinearity due to wave height can be taken into account when calculating added resistance in head and oblique seas. Obtained results and discussion in the present study are summarized

In Chapter 8, General conclusions and recommendations

Chapter 2

Motion free tank experiments

2.1 Introduction

This chapter describes the detailed experimental study to estimate the added resistance in irregular waves. The tank experiments are conducted in the Osaka University towing tank facility with RIOS containership model of $L_{ppm} = 2.5\text{m}$ at the Froude number $\text{Fn} = 0.25$. The length ,width and depth of tank are 100, 7.8 and 4.35 m, respectively. The motion-free test condition is conducted in which the ship model was free to surge, heave, and pitch. In this condition, wave-induced ship motions and hydrodynamic forces acting longitudinal direction for the added resistance are measured simultaneously. Calibration of irregular waves is done at the wave probe location in the wave basin prior to the estimation of added resistance. Target and measured wave spectra are satisfied to have accurate generation of irregular waves using wave spectrum analysis by FFT. The wave conditions set in the irregular wave resistance test are significant to validate the non-linear PDF method at smaller and larger significant wave heights. Added resistance is estimated on the sea states belong to significant wave height $H_{1/3} = \ 2\text{m}\ , 5\text{m}$ and mean wave period [T_{01}] from 7 to 15s on full ship scale in the long-crested irregular waves.

2.2 Ship model and experiment set up

The ship model used in experiments is container ship provided by the Research Initiative of Oceangoing Ships (RIOS), which is being researched and developed at Osaka University, and models' principal particulars are shown in Table 2.1. Fig. 2.4 shows the schematic view of the experimental facility and its main dimension for RIOS's containership model. The body plan and the ship model is shown in the Fig. 2.1 and Fig. 2.2, respectively. In the experiment, wave displacement, surge, heave, and pitch, and the sampling time was set to $\Delta T = 0.01\text{s}$.The conditions are determined based on the actual ship scale of L_{pp}= 209.3 m (overall length L_{OA} = 220.0 m) published in RIOS. It is equipped with a plunger type wave maker which generates the irregular waves of different wave spectrums of maximum height 500mm and wavelengths ranging from 0.5 to 15m. Wave absorbers are fitted on both sides of the tank to dampen the waves after each run.

The model is towed with light weight carriage connected to main carriage by means of weak spring to allow the ship model to be free in surge motion. The potentiometer attached to the model measure pitch, the one at the top of the guide rods measure heave as shown in the Fig 2.4. Force is applied to back-and-forth motion in longitudinal direction as it does not have stability and can hit the rail ends while doing experiments in waves. So, the surge motion needs to be adjusted. In the resistance test, the surge motion was relatively hold by an external force F_0 received by the hull generated by the spring system. The external force F_0 is proportional to the displacement and is applied to the ship model to avoid large stretch for spring. It is restricted by a spring in the experimental set up of spring constant $K = 70\mathrm{N/m}$ and initial tension of $\Delta F = 4.32$ N.

TABLE 2.1: Principle particulars of RIOS containership

Particulars	Full scale	Model scale
Length between perpendiculars, L_{pp} [m]	209.3	2.5
Maximum beam of waterline, B [m]	32.2	0.3846
Draft, d [m]	11.5	0.14
Displacement volume , ∇ [m^3]	48037.469	0.08128
Block Coefficient, C_b	0.6040	
LCB (%L_{pp}) (from Mid. Aft+)	2.12	
VCG (from keel) , KG [m]	13.2593	0.158
Gyration radius, K_{xx} /B	0.35	
Gyration radius, $K_{zz}/L_{pp}, K_{yy}/L_{pp}$	0.2508	

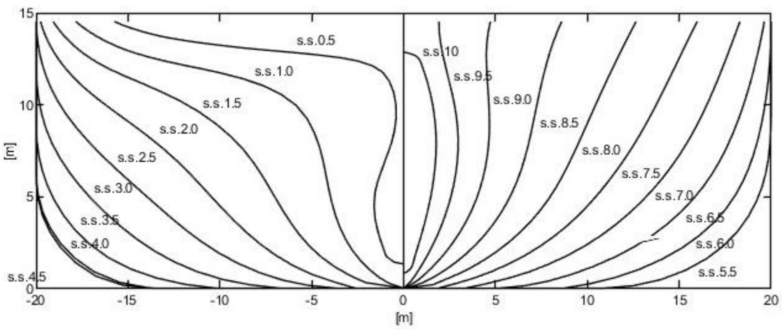

FIGURE 2.1: Body plan of RIOS containership below waterline of full load condition

FIGURE 2.2: RIOS containership model at Osaka University Towing tank facility

FIGURE 2.3: Adjustment of the Radius of Gyration

During the test, sway and yaw motions were constrained in this study. The dynamometers at the middle of the guide rods measures the longitudinal force including surge force and added resistance. Radius of Gyration and VCG was confirmed and adjusted by this swinging equipment (Fig. 2.3). Through this guide rod, the carriage tows the model at a given speed of $\mathrm{Fn} = 0.25$. Waves were measured by capacitance type wave probes in the experiments in which set up one probe was in front of the bow of the model ship, and another one at the side of the model.

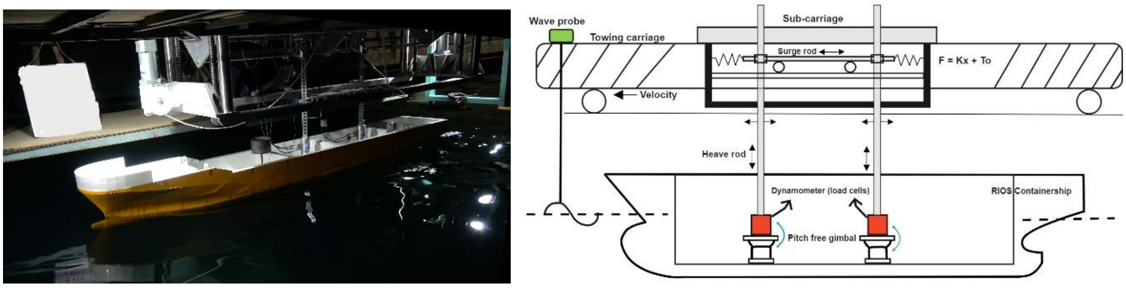

FIGURE 2.4: Experimental set up in towing tank facility and its schematic view for motion free test for measuring resistance in waves.

2.3 Wave generation and experimental condition

The long-crested irregular head waves were generated using the JONSWAP wave spectrum from the wave generator which is calculated by the approximate equation with the input parameters as significant wave height and mean wave period and can be expressed as given in the Eq. 2.1. The calibration coefficient was calculated from the obtained capacitance type wave probe system. By multiplying the obtained coefficient to experimental data, the actual wave measurements can be obtained. We decided to simulate the sea states belong to significant wave height [$H_{1/3} = 2\mathrm{m}, 5\mathrm{m}$] and mean wave period [$T_{01}$] from 7 to 15s are on full ship scale in the long-crested irregular waves.

$$S(\omega|H_{1/3},T_{01}) = \alpha H_{1/3}^2 \frac{\omega^{-5}}{\omega_p^{-4}} exp\left[-\frac{5}{4}\left(\frac{\omega}{\omega_p}\right)^{-4}\right] \gamma^{exp\left[-\frac{(\omega-\omega_p)^2}{2\tau^2\omega_p^2}\right]} \tag{2.1}$$

Where,

$$\alpha = \frac{0.0624}{0.230 + 0.0336\gamma - 0.185(1.9+\gamma)^{-1}}$$

$$T_P = \frac{T_{01}}{0.7303 + 0.04936\gamma - 0.006556\gamma^2 + 0.0003610\gamma^3} \quad , \quad \omega_p = 2\pi/T_p$$

$$\gamma = 3.3$$

$$\tau = 0.07 \quad for \quad \omega \le \omega_p$$

$$\tau = 0.09 \quad for \quad \omega > \omega_p$$

Where γ is the spectral peak enhancement factor, α is the dimensionless constant , and σ is the spectral peak width parameter.

In order to obtain a sufficient number of encounter waves, the phase term (which was defined by different random seed numbers) at the time of irregular wave generation was varied for all wave conditions to obtain the larger time series of wave components without repetition in different realizations of the irregular seas. Total of 3 runs were made. The experimental condition is shown in Tables 2.2.

TABLE 2.2: Model tank tests in head sea conditions for RIOS containership

(a) Calm water test	
Fn	0.25
Motion allowed	free surge, heave, and pitch
(b) Regular wave conditions	
Fn	0.25
Motion allowed	free surge, heave, and pitch
λ/L_{pp}	0.2 to 3
H_{wm} (m)	0.020
(c) Irregular wave Conditions	
Fn	0.25
Motion allowed	free surge, heave, and pitch
$H_{1/3m}$ (m)	0.024, 0.060
T_{01m} (s)	0.765, 0.874, 0.984, 1.093, 1.202, 1.311, 1.421, 1.530, 1.639

2.4 Results and discussions

Time series data of calm water and total drag resistance is obtained for all the test cases. The section in the time series data is analyzed when it becomes a constant speed after accelerating the towing vehicle and the clamp is released. Total analysis period was about 50s including the transient response in each run. In each 50s of run, transient response subsided after 20 secs of accelerating the carriage and releasing of clamp as shown in Fig. 2.5. Hence, approximately 30s of each run was considered for analysis for the calculation of average added resistance, then taking an average of all the 3 runs of converged time window for each sea state case mentioned in Table 2.2 which are different test conditions in model ship scale. Towing tank tests were performed under the calm water and waves conditions. Measured time series data of wave elevation in long-crested irregular waves obtained in model tank tests for case $H_{1/3m} = 0.024m$, $\mathrm{T}_{01\mathrm{m}} =$ 1.093s as shown in Fig. 2.8. Wave spectrum of the generated waves was obtained by applying fast Fourier transformation to the time series of the wave elevation attached in front of the ship in the tank tests and it was compared with the target wave spectrum as shown in Fig. 2.6.

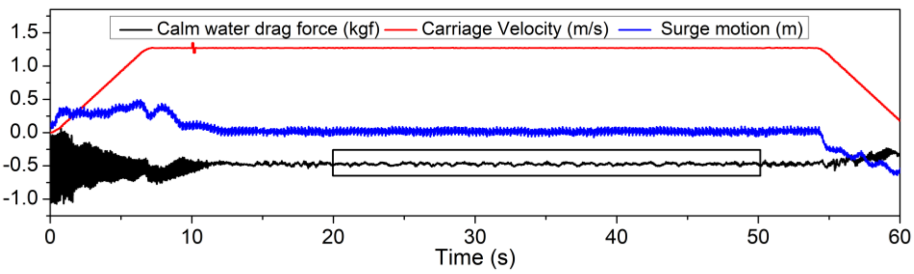

FIGURE 2.5 Measured experimental data in calm water conditions to find valid time range for converged solution

Average significant wave height and average wave spectrum energy is calculated by using Eq. 2-3.

$$\bar{H}_{1/3m} = \sqrt{\left\{\left(H'_{1/3m}\right)^2 + \left(H''_{1/3m}\right)^2 + \left(H'''_{1/3m}\right)^2\right\} / 3} \tag{2.2}$$

$$\bar{S}_\omega = (S'_\omega + S''_\omega + S'''_\omega) / 3 \tag{2.3}$$

where $', '', '''$ represents the first test , second test and third test run.

Table 2.3 shows a comparison of the significant wave height and average period obtained by the wave test. Although there is a slight difference between the measured significant wave height and the mean wave period in the tank tests from the target value as visible in Table 2.3 because there is always uncertainty attached in conducting the experiments. however, it is considered that there is no problem in practical use.

TABLE 2.3: Measured vs target $H_{1/3}$ and T_{01} in irregular wave experiment

Test run	$H_{1/3m}$(mm)		T_{01m}(s)	
	Target	Measured	Target	Measured
1	24	27.29	1.093	0.985
2	24	24.98	1.093	1.052
3	24	27.90	1.093	0.971

In order to obtain the sea wave spectrum $S(\omega)$ from the encountered wave spectrum of the ship $S(\omega_e)$ from the time series data of encountered wave by the ship and change the encounter frequency ω_e to the wave frequency ω , Eqs. 2.4 and 2.5 are used.

$$\omega_e = \omega - \frac{\omega^2}{g} U \cos \mu_s \tag{2.4}$$

$$S(\omega) = S(\omega_e) \left|\frac{d\omega_e}{d\omega}\right| \tag{2.5}$$

where ships' moving direction for head seas(μ_s) is 180° .

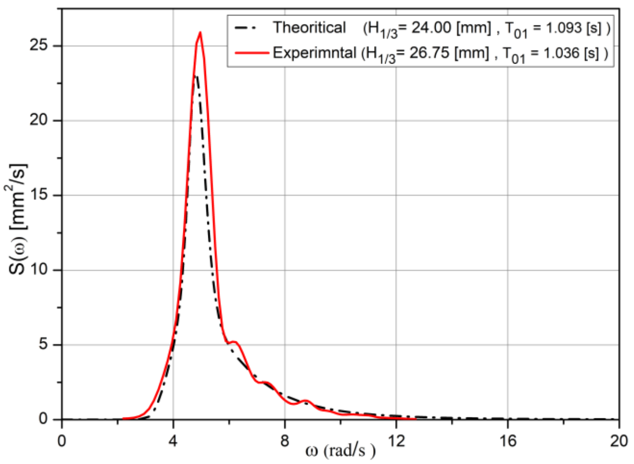

FIGURE 2.6 A comparison of target JONSWAP wave spectrum with measured wave spectrum at $H_{1/3} = 2m$, $T_{01} =$ 10s on full ship scale.

The measured time-series data of total longitudinal resistance as shown in Fig. 2.7 was averaged for the time range after stabilizing the initial model responses and subtracted the mean value of calm water resistance to obtain the significant values for average added resistance. Final comparison of results are shown in Chapter 7.

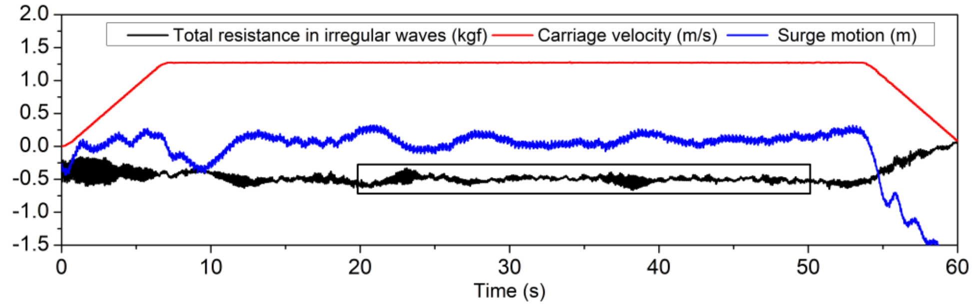

FIGURE 2.7 Time history of measured total resistance force in irregular waves ($H_{1/3}$ = 2m, T_{01} = $10s$, $Fn = 0.25$ on full ship scale).

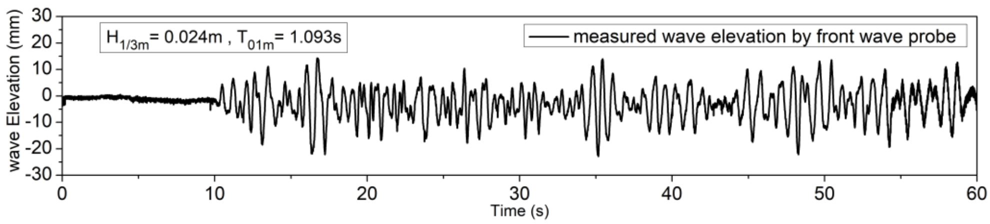

FIGURE 2.8 Time history of measured encountered long-crested irregular waves. Assuming long-crested irregular waves ($H_{1/3}$ = 2m, $T_{01} = 10s$, $Fn = 0.25$ on full ship scale).

2.5 Conclusion

This chapter described the detailed experimental study to estimate the added resistance in irregular waves. The motion-free test conditions were conducted in which the ship model was free to surge, heave, and pitch. In this condition, wave-induced ship motions and hydrodynamic forces acting longitudinal direction for the added resistance are measured simultaneously. After calibration of irregular waves, Target and measured wave spectra are satisfied to have accurate generation of irregular waves using wave spectrum analysis by FFT. The wave conditions set in the irregular wave resistance test are significant to validate the non-linear PDF method at smaller and larger significant wave heights. Added resistance is estimated on the sea states belong to significant wave height [$H_{1/3}$] = 2m, 5m and mean wave period [T_{01}] from 7 to 15s on full ship scale in the long-crested irregular waves.

Chapter 3

Formulation of correction coefficient due to wave height effect

3.1 Introduction

In this chapter, wave height effect on the added resistance in waves is investigated in head and oblique sea regular waves by the CFD RANSE method on KCS and RIOS containership under the different wave heights. That effect illustrates the characteristic of nonlinearity with respect to wave height in added resistance calculations and is shown as a ratio of added resistance at higher wave heights to linear condition at small wave height and small wave steepness. The non-linearity with respect to wave height squared is empirically expressed as a "correction coefficient $C(s, V)$ or $C(s)$" using CFD simulations in head and oblique regular waves and incorporated this non-linear wave height effect into linear added wave resistance transfer function. It is determined as the relative ratio of nonlinearity to linearity, which is calculated at a few representative frequencies. This correction coefficient is used in the proposed stochastic mathematical model to obtain the added resistance response function that considers the non-linearity with respect to the wave height. It includes the formulation and computational methods used in this study. Non-linearity due to wave steepness (wave height to wavelength ratio), which is more pronounced in the short wavelength region, has been pointed out, and such wave height effects (or wave steepness effects) can be incorporated into short-term predictions.

3.2 Why computational fluid dynamics method is used.

In order to investigate the wave height effect and obtain the correction coefficient, we have used a commercial CFD software, FINE/Marine V 10.2.2, which is based on the ISIS-CFD flow solver developed at Ecole Centrale de Nantes (ECN). It solves the incompressible RANS equations with an unstructured finite volume method and Volume-of-Fluid (VOF) type interface capturing method for detecting the free surface between air and water. The Mathematical details in the development of ISIS-CFD are described by Queutey and Visonneau[41]. In this paper, we have mentioned the formulation of CAD ship model geometry and configurational set up for defining boundary conditions in regular waves of different wavelengths with varying wave heights/wave steepness.

For simulating free-surface flows and their interactions with an advancing ship, the use of interface capturing methods is effective. In order to enhance the sharpness of the interface to have better results, many studies have been made. For a review of the development of various interface capturing techniques, we can refer to Wackers et al.,(2011)[52] which also describes the details of ISIS-CFD flow solver together with validation results. Application of ISIS-CFD flow solver to unsteady seakeeping problems was shown by Guo et al.(2012)[1] and careful and systematic study on uncertainty and convergence using 4 different meshes was performed, which shows the reliability and accuracy of computed results for the prediction of ship motions and added resistance. Judging from these results obtained so far regarding the reliability of the ISIS-CFD flow solver, it may be appropriate to use FINE/Marine as an analysis tool for seakeeping problems and longitudinal drag resistance forces to compare with the theoretical and experimental results to be obtained in the present study.

This CFD code solves the incompressible unsteady RANS equations using the finite volume method to generate the spatial discretization of the equations. The governing equations for an incompressible flow are the Navier-Stokes and continuity equations. In treating turbulent flows, The k - ω SST model is adopted for the simulation with FINE/Marine. Table 3.1 shows the summary of the schemes used in the present CFD simulation. Details refer to FINE/Marine V,10.2.2 [36].

TABLE 3.1: Schemes used in the present CFD simulation

Item	Scheme used
Grid system	Unstructured, non-conformal, fully hexahedral grid
Spatial discretization	Finite volume method
Time marching	Backward difference, sub-iteration with virtual time
Free-surface capturing	VOF method (BRICS scheme)
Body-surface Boundary Condition	Logarithmic function as wall function
Turbulence model	k - ω SST

3.3 Numerical modeling in regular head waves.

KCS hull model, Korea Research Institute of Ships and Ocean Engineering (KRISO) and RIOS (Research Initiative on Oceangoing Ships) containership hull types are selected as a case study to predict the added resistance at different wavelength and wave steepness. The principle particulars of the ships are given in the Table 3.2. The 3D model and body plans of KCS and RIOS container ship are shown in Fig. 3.1 and Fig. 3.2, respectively. The hull model used is symmetrical, so the only half of the ship hull is used in the calculations for head waves conditions, thus a symmetry boundary condition is adopted at the center plane boundary. The origin of the computational domain is the hull centerline and the midship on the draft line. The coordinate system, dimensions of computational domain used in this calculation and boundary conditions for each external boundary as shown in Fig. 3.3. The computational domain is $-2.0\ L_{ppm} \leq$ x $\leq 4.5\ L_{ppm}$ in length, $-2.0\ L_{ppm} \leq$ y $\leq 0\ L_{ppm}$ in width and $-2.0\ L_{ppm} \leq$ z $\leq 1.5\ L_{ppm}$ in height. Here, L_{ref} is set to either max(λ or L_{ppm}).

To accurately represent the regular waves, a grid refinement region of different dimensions and mesh size was set near the free surface as shown in Fig. 3.4. Box 1 represents the domain of the incident wave coming from inlet wave generator, ship-hull, and vortex. In region 1 near the hull, the grid was made fine so that the regular waves would not be attenuated, but in the other regions, the grid was made gradually coarser in regions 2, 3, and 4 because it was necessary to consider damping zone for attenuating the waves to reduce reflections at the exit boundaries. Within this zone, a sponge layer.

TABLE 3.2: Principle particulars of ships

Particulars	Symbols	KCS	RIOS containership
Length between perpendiculars	L_{ppm} [m]	3.2000	2.5
Maximum beam of waterline	B [m]	0.4480	0.3846
Draft	d [m]	0.1503	0.14
Displacement volume	∇ [m3]	0.1401	0.08128
Block Coefficient	C_b	0.6505	0.6040
LCB (from Mid. Aft+)	$(\%L_{pp})$	1.48	2.12
VCG (from keel)	KG [m]	0.1994	0.158
Gyration radius	$K_{xx}/$B	0.40	0.35
Gyration radius	$K_{zz}/L_{pp}, K_{yy}/L_{pp}$	0.25	0.2508

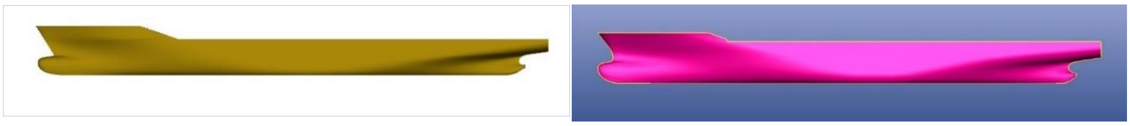

FIGURE 3.1: 3D model of KCS (left) and RIOS containership (Right)

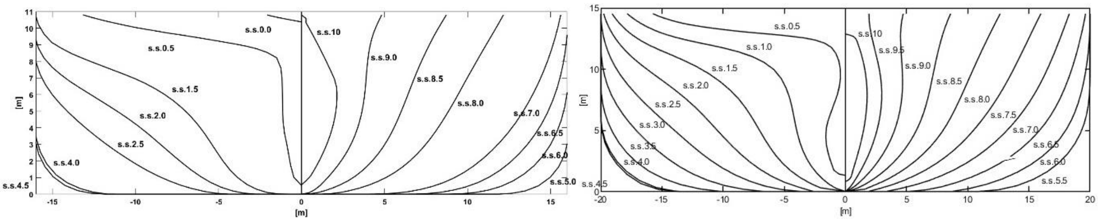

FIGURE 3.2: Body plan of KCS (left) and RIOS containership (Right) below waterline of full load condition

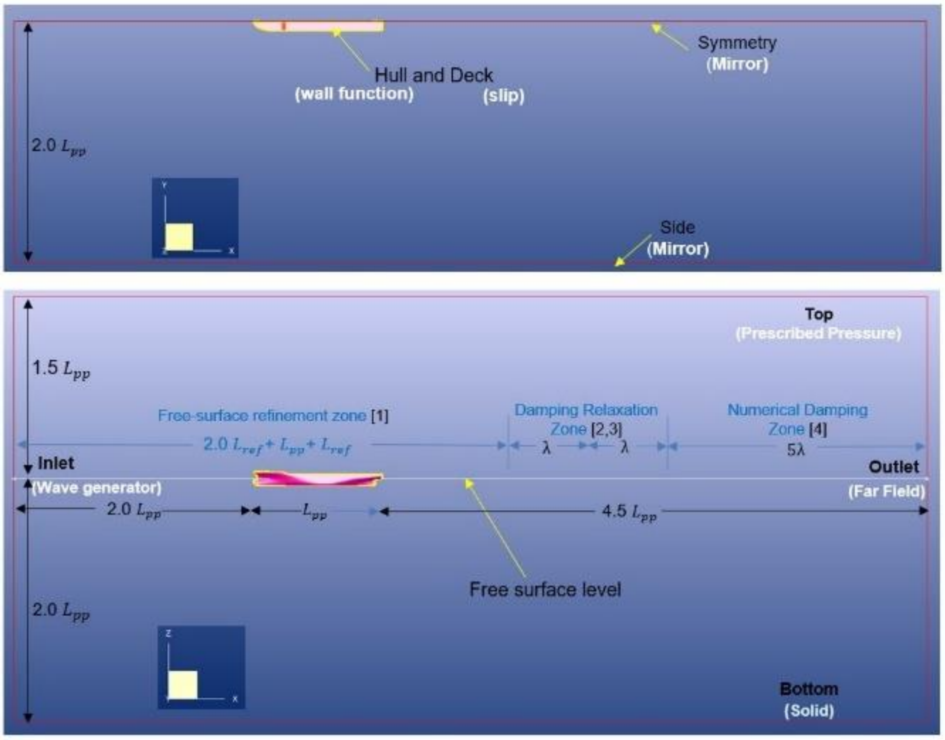

FIGURE 3.3: Dimensions of computational domain and free surface refinement regions.

acts as a damping medium in z-direction. Since the Kelvin waves created by the ship will be dampened by the damping zone behind the body hence no particular sidewise.The grid sizes in each region are set $dx = \lambda_{\mathrm{m}}/80$ and $dz = H_{wm}/16$. Generation of regular waves requires 80 cells per model wavelength(λ_m) in the x and y directions and 16 cells per model wave height (H_{wm}) in the z-direction to propagate the waves on the free surface appropriately and applying a constant grid cell size for both x and y directions in the refined grid area for the free surface ITTC (2011)[12]. Local mesh refinements were applied around the hull and free surface area to capture the proper incident wave field as shown in Fig. 3.5. The added resistance in short waves is dominantly affected by the diffraction waves around the ship bow region. Thus, the bow shapes and wave amplitude of the incident wave significantly affect the added resistance in short waves. The inlet boundary was set to external as a wave generator. Both sides of the boundary were set to mirror for the case of head waves to suppress the wave reflection on the side boundary. The outlet boundary was set to external, and the speed was 0 m/s at the outer far field. Stokes waves from 1st to 3rd order can be applied and the estimation of the wave order is automatically performed according to Fig. 3.6. In most of the cases, the 2nd order Stokes waves were used in this simulation considering the tendency in the experimental wave profiles for the head waves simulation with a half body, an imposed motion was applied in the surge direction (negative x direction) with 1/2 sinusoidal ramp condition while heave and pitch motions were solved, and all other degrees of freedom (sway, roll, and yaw) remained constraint due to symmetry condition.

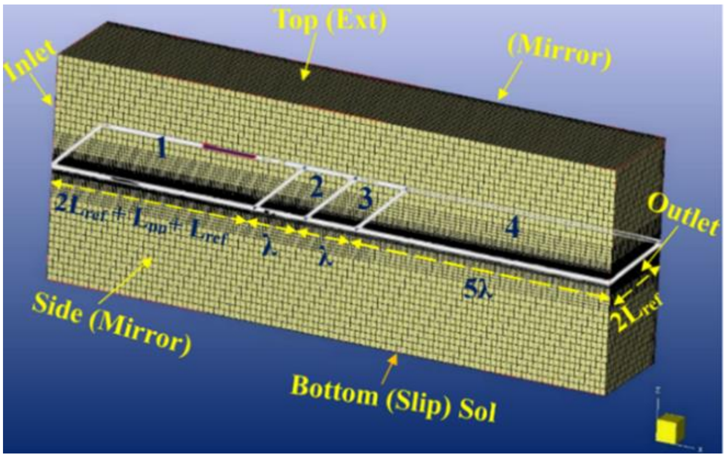

FIGURE 3.4: Meshed computational domain with box refinement and boundary conditions for regular waves.

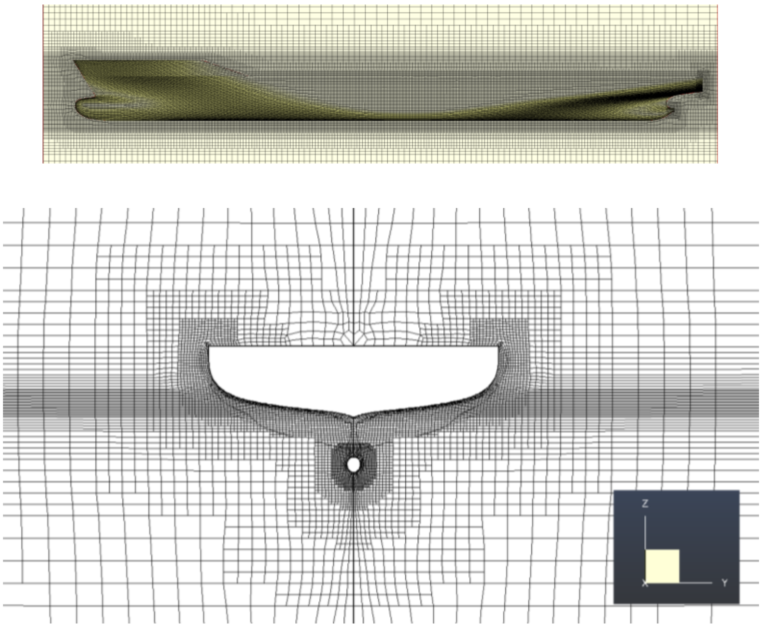

FIGURE 3.5: Mesh around bow and extra mesh refinement at shaft end and transom (Top and Bottom)

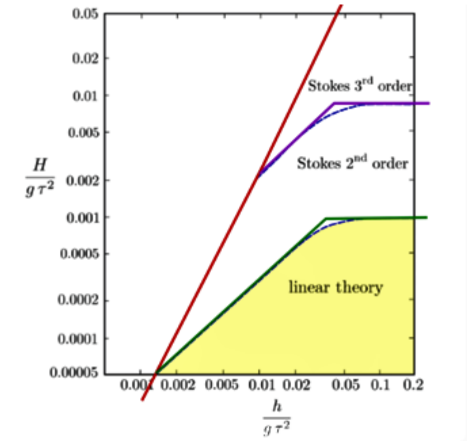

FIGURE 3.6: Order of stokes wave generation

Two approaches i.e., the overset grid method (Chimera approach) and the mesh deformation technique can be differentiated in terms of how the mesh behaves when the ship is moving. Former the overset grid method can manage larger ship motions than the mesh deformation technique, but it has the drawback of some numerical errors caused by the interpolation exchange in the overlapping cells. However, Fine marine gives good and accurate results with weighted mesh deformation technique in calm water and regular wave conditions (heave and pitch motion) in less computational time. If the amount of deformation is not so large, a single grid is recommended with excellent calculation accuracy. In regular waves, ship motions are solved for heave and pitch only, other degrees of freedom are constrained. Hence, it is not complex configuration unlike irregular waves case. For the current settings, the morphing mesh technique is up to two times faster as compared with the overset mesh for similar number of cells. The simulation time needs to be divided into discrete time steps. A time step of at least 100 steps per wave period is recommended by the ITTC (2011)[12]. For implicit solver like ISIS-CFD the Courant number condition does not apply as the explicit solver and hence the BRICS scheme is applied instead. For each time step, the solver carries out some non-linear iterations to find the most accurate solution to the system of equations. To satisfy this condition according to the recommendation from FINE/Marine, minimum number of 12 non-linear iterations for seakeeping simulations and a convergence criterion of 4 orders of magnitude have been used in all the simulations.

Furthermore, before implementing the present study, we have conducted the grid convergency tests on the free surface for proper generation of regular waves to check the dependency of numerical results on the number of mesh and time step, and we have confirmed appropriate selection of the parameters; with which we confirmed that virtually no decaying phenomenon exists in an important computational domain around a ship.

Grid convergence test

Before the investigation of the added resistance response using the CFD numerical setup, mesh independency tests were performed to capture the accurate wavelength and free surface elevation only for the short wavelength cases ($\lambda/L_{pp} = 0.5$) because in the short waves if the mesh is not fine enough then added resistance might be underestimated. Ley et al. (2014)[28] and Seo et al. (2014)[45] showed in their research that the added resistance of a ship is quite sensitive to the grid spacing near the bow region. So, the coarse and fine mesh cell size were derived by reducing and increasing cell numbers per wavelength and cell height on free surface respectively using a factor of $\sqrt{2}$ based on the base mesh case (Case no. 8 for short wave conditions in Table 3.4). The simulation time step was calculated proportionally to the mesh size as shown in Table 3.3 where T_e represents the corresponding encountering period.

TABLE 3.3: Grid convergence test cases ($\lambda/L_{pp} = 0.5$, Fn $= 0.2$ $H_{ws} = 8$m)

Mesh	Number of cells (10^6) Millions	$\lambda_m/\Delta x$	$H_{wm}/\Delta z$	$T_e/\Delta t$
Coarse (G1)	8.39	56	11	70
Base (G2)	24.2	80	16	100
Fine (G3)	42.2	113	22	141

Nominal Wake Field

The wake field that would be measured at the propeller plane without the presence or influence of the propeller modifying the flow at the stern of the ship. Difference between free stream velocity V and local speed V_x normalized by the free stream velocity called Wave Fraction 'w'. if local velocity is free stream velocity that means wake fraction is zero that is uniform flow.

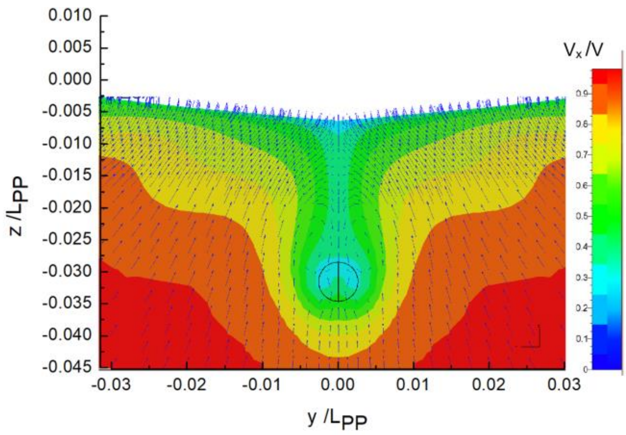

FIGURE 3.7 Computed velocity distribution on the propeller plane (x/L =0.98) in calm water

$$w = \frac{V - V_x}{V}$$

The velocity normalized by inflow velocity and the flow into the propeller surface were verified by the nominal wake field in calm water . The wake fields are compared with the experimental results of EFD and CFD results of Wu et al. (2020) shown in Fig. 3.8.

The Fig. 3.7 shows the velocity vector and streamline of the flow, and velocity contour obtained through present CFD computation. The agreement between present CFD and the EFD and CFD by Wu et al. (2020) is good. A hook-shaped vortex is clearly generated on the propeller plane. The Present CFD results and very similar to CFD results of Fig. 3.8, however, the shape of the wake in the CFD results compared to the EFD results of Fig. 3.8, was slightly smaller. The difference is attributed to the effect of scale; nevertheless, it is considered to be sufficient to show the tendency of the wake.

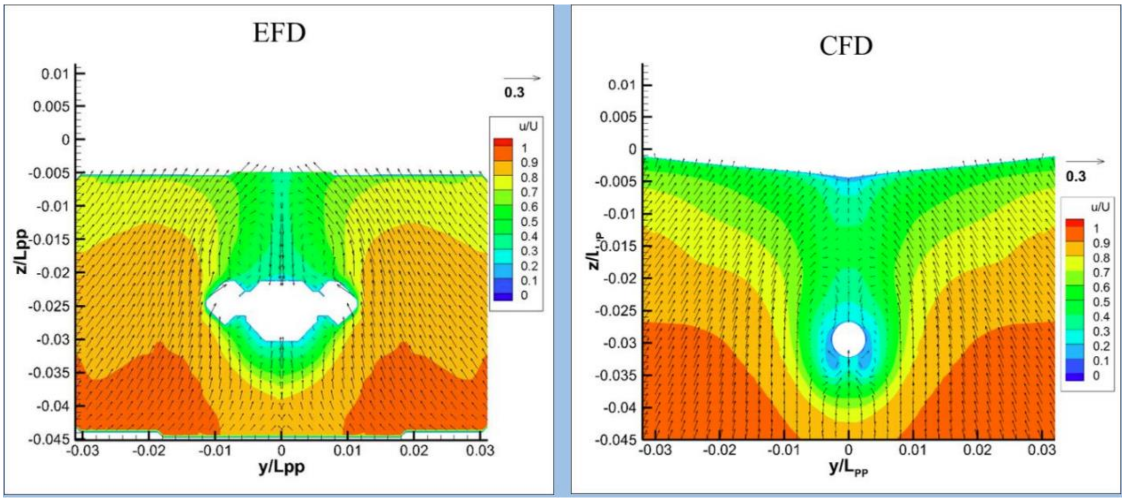

FIGURE 3.8 Comparison of the nominal wave field in calm water. Left: EFD and Right: CFD by Wu et al. (2020)

Wave calibration test

Also, wave calibration tests need to be done prior to the calculation of added resistance as mesh should be good enough for modeling waves properly. It was performed for different wave heights in short-wave conditions. Wave contour of the free surface and results of wave elevation in the calculation domain is shown in Figs. 3.9. The difference of the simulated model wave height and input wave for the case of short waves in the CFD calculation setup is 0.99% which means the time step used and the mesh cell size are suitable for the CFD simulation model.

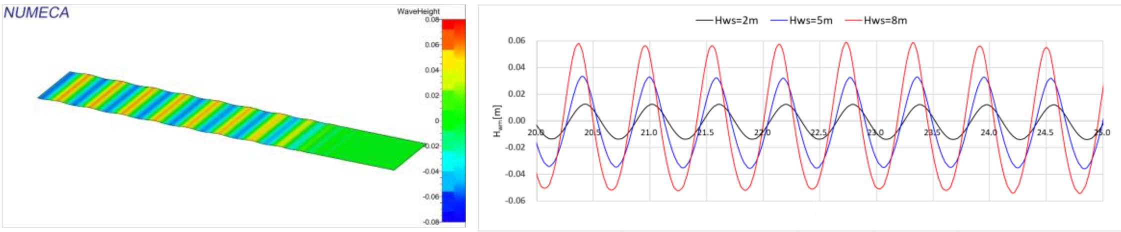

FIGURE 3.9: Snapshot of spatial wave profile for wave calibration test ($\lambda/L_{pp} = 0.5$, $H_{ws} = 8m$) and Simulated wave elevation for model wave height ($\lambda/L_{pp} = 0.5$)

3.3.1 KCS hull type numerical simulation conditions

CFD numerical simulation results of added resistance for the KCS hull model in regular head waves were compared with theoretical available data by a potential-based calculation method based on linear assumptions. CFD simulations are carried out for the cases given in Table 3.4. The calculation conditions are shown in Table 3.4, where Fn is set to three conditions, λ/L_{pp} is set to three conditions, the maximum wave height (actual ship scale wave height = H_{ws}) is set to four conditions, and the wave direction is set to all as head sea waves (α = 180deg.). However, for $\lambda/L_{pp} = 0.5$, wave collapse occurred at H_{ws} = 10m, with wave steepness of about 1/12 and 1/8, respectively, and the calculation got diverged. Therefore, it was excluded from the calculation conditions. The relationship between the added resistance for the 4 different wave steepness (H_{ws}/λ) values are investigated for short ($\lambda/L_{pp} = 0.5$), moderate ($\lambda/L_{pp} = 1.0$) and long ($\lambda/L_{pp} = 1.5$) wave conditions at the ship speed related to Fn $= 0.14, 0.20, 0.26$. The additional calculation at $\lambda/L_{pp} = 0.6$ was performed to confirm the accuracy of the calculation at $\lambda/L_{pp} = 0.5$ and was only performed for Fn = 0.20 condition at $H_{ws} =$ 2m , 5m.

TABLE 3.4: CFD simulation cases for added resistance calculation for different wave heights

CFD case no.	λ/L_{pp}	H_{WS} (m)	Fn
1-9	0.5	2, 5, 8	0.14,0.20,0.26
10-21	1	2, 5, 8, 10	
22-33	1.5	2, 5, 8, 10	

The added resistance in waves was calculated by CFD numerical simulations which directly integrates the pressure acting on the hull surface and estimates the added wave resistance i.e., an increase in resistance in waves by taking the difference in resistance when traveling in waves and in calm water according to Eq. 3.1.

$$R_{aw} = R_{Total} - R_{Calm} \tag{3.1}$$

Calm water Resistance results (R_{Calm})

The grid topology used for numerical simulations for estimating calm water resistance at different Froude numbers was the same as used in simulation in estimating the resistance in regular waves and obtained the converged forced signals for R_{Calm} as shown in Fig. 3.10. The resistance was taken by averaging the force for last 10 secs in the converged range.

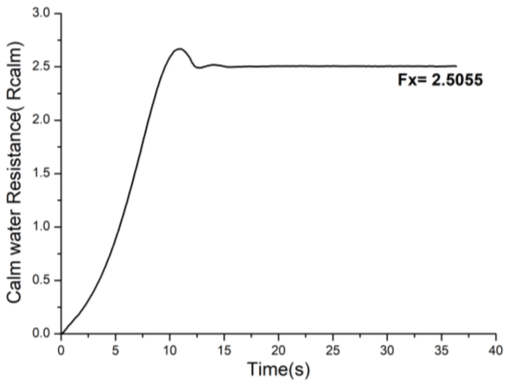

FIGURE 3.10: Convergence history of resistance in calm water (Fn = 0.2)

For the added resistance analysis, regular waves of different wave heights were input and total resistance in waves (R_{Total}) was calculated from CFD simulations for short and long wave cases (from case 1 to case 33). Convergence of numerical simulations showed the accuracy of waves after 10 periods of oscillations as after those numerical results showing repeatability as shown in Fig. 3.11 for the short wavelength case. So, taking the average of a minimum of 8 oscillations of converged solution for all the cases is shown as two vertical blue-color dotted lines. Finally, we calculated the added resistance coefficient for all the cases and compare the added resistance coefficient in waves with potential-based theoretical results shown in Figs. 3.13~3.14. Free surface animation contour is shown in Fig. 3.12 for short wave case no. 8.

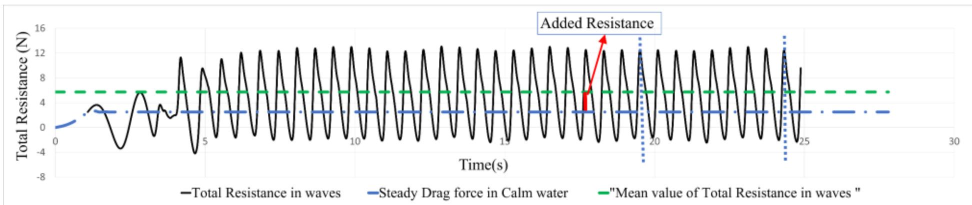

FIGURE 3.11: Time history of total resistance in regular waves for symmetric KCS hull at Fn = 0.2 , $H_{ws} = 8m$ for $\lambda/L_{pp} = 0.5$

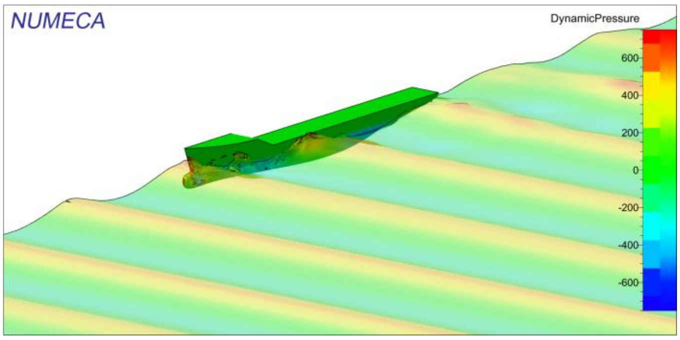

FIGURE 3.12: Free surface contour around hull in regular waves (head sea, Fn = 0.2, H_{ws}= 8m)

In Fig. 3.13, Non-linear effects can be seen at $\lambda/L_{pp} \geqq 1.0$, the resistance increase coefficient decreases as the wave height increases. A similar trend was seen with different Froude numbers as shown in Fig. 3.14. It shows that the values of the added resistance coefficient in short waves are much smaller than those in long waves as shown in Figs. 3.13~3.14, which indicates that the added resistance in short waves with smaller wave heights is difficult to predict experimentally and numerically.

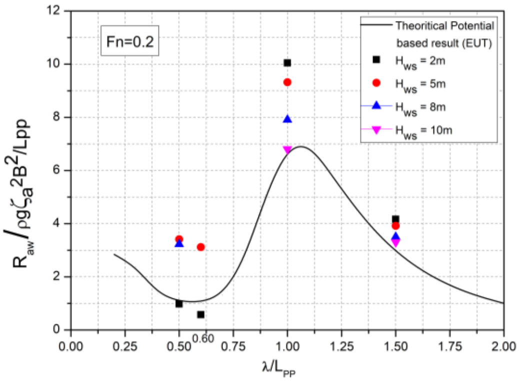

FIGURE 3.13: The results of the CFD calculation of the non-dimensional added resistance coefficient in regular waves at Fn = 0.20.

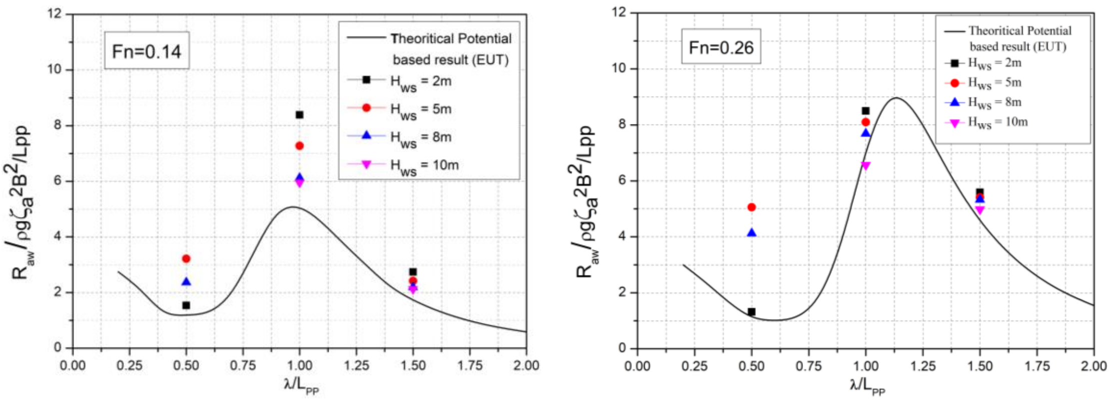

FIGURE 3.14: Non-dimensional added resistance coefficient in regular waves by CFD at Fn = 0.14 and 0.26.

3.3.2 RIOS hull type numerical conditions

CFD simulations were carried out to estimate the added resistance in regular head sea waves for only RIOS containership for the cases given in Table 3.5. The time steps used for these calculations were based on the encounter frequency between ship and waves as given in Table 3.6. However, for $\lambda/L_{pp} = 0.5$, wave collapse occurred at H_{ws} = 10m, with wave steepness of about 1/12 and 1/8, respectively, and the calculation got diverged. Therefore, it was excluded from the calculation conditions and additional calculation was performed to at H_{ws} = 4m to confirm the accuracy of the calculation in short wavelength case.

TABLE 3.5: CFD calculation cases

CFD case no.	λ/L_{pp}	H_{WS} (m)	Fn
1-4	0.5	2, 4, 5, 8	
5-8	1	2, 5, 8, 10	0.25
9-12	1.5	2, 5, 8, 10	

TABLE 3.6: Time step calculation

λ	Time period(s)	Wave freq.	Adv. freq.	Encounter freq.	Encounter period(s)	Timestep (s)
1.25	0.8952	1.1170	0.990	2.1070	0.4746	0.004746
2.5	1.2660	0.7899	0.495	1.2848	0.7783	0.003891
3.75	1.5506	0.6449	0.330	0.9749	1.0257	0.003419

Calm water resistance

CFD simulations in calm water performed using the same grid topology as used in simulation in regular waves and obtained the converged drag resistance R_{Calm} as shown in Fig. 3.15. The resistance was calculated by averaging the drag force for about 10 secs in the converged range.

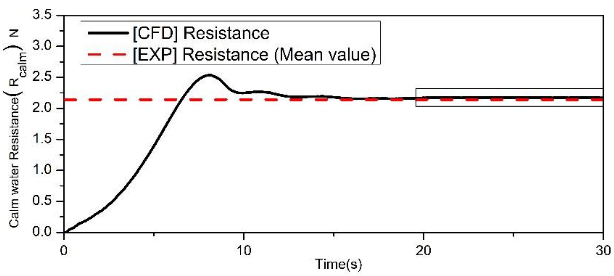

FIGURE 3.15: Comparison of resistance in calm water obtained using CFD (port side) with experimental results (Fn = 0.25).

Total resistance in waves was evaluated by the last 10 periods converged in numerical simulations as shown in Fig. 3.16. So, taking the average of a minimum of 10 oscillations of converged solution for all the cases i.e., two vertical blue-color dashed lines visible in Fig. 3.16. Finally, we calculated the added resistance coefficient for all the cases and compare the added resistance coefficient in waves with potential-based theoretical results shown in Fig. 3.18. Free surface contour with ship is shown in Fig. 3.17 for the short-wave case no. 4 which shows appropriate propagation of regular waves and diffracted waves get absorbed properly at the damping zone.

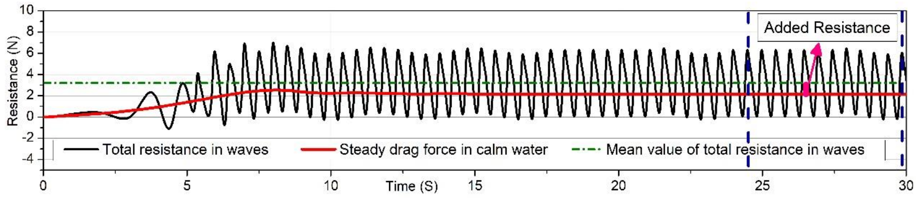

FIGURE 3.16: Time history of total resistance in regular waves for symmetric RIOS hull at Fn $= 0.25, \lambda/L_{pp} = 0.5, H_{ws} = 8$m on full ship scale.

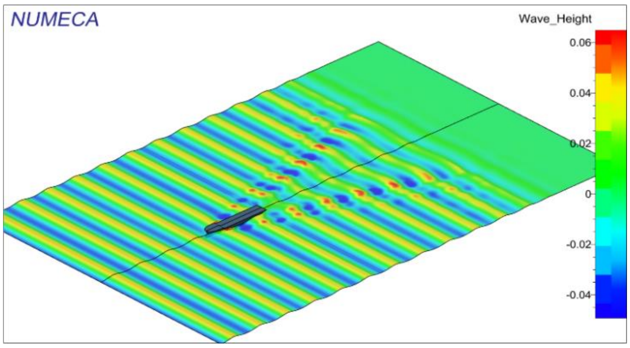

FIGURE 3.17: Free surface contour around ship hull in regular waves (head sea, $\lambda/L_{pp} = 0.5$, Fn $= 0.25$, $H_{ws} = 8$m on full ship scale)

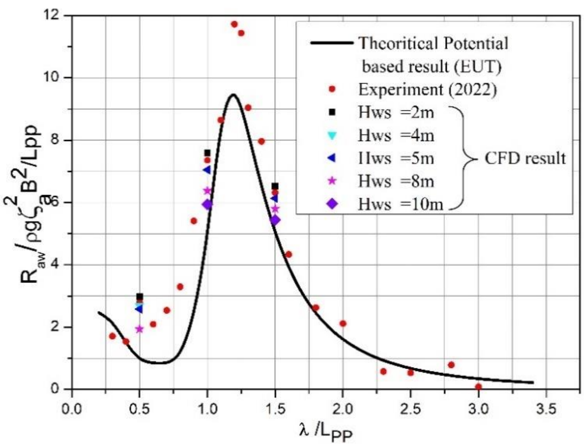

FIGURE 3.18: Comparison of CFD and experimental results in regular waves at Fn $= 0.25$ with theoretical results obtained by potential based method.

In Fig. 3.18, non-linear effects can be seen at λ/L_{pp} = 0.5, λ/L_{pp} =1.0 and λ/L_{pp} =1.5. This indicates that the tendency of the added wave resistance coefficient with respect to the normalized wavelength changes not only quantitatively but also qualitatively depending on the wave height. The added resistance coefficient decreases when wave steepness increases. The major reason is considered that the influence of the hull form above the waterline on the added resistance in waves varies depending on the wave height. Since the bow wave is easily broken as the steepness of the incident wave increases, the variation in wetted area is not proportional to the wave amplitude. From this, we can see that added resistance in waves is not necessarily proportional to the square of the wave height.

3.4 Numerical modeling in regular oblique waves.

Kunpeng, C et al. (2021)[21] compared the added resistance in oblique regular waves using CFD results with potential theory results and towing tank test results, but the differences of results observed in the comparison as added resistance CFD values are larger than potential values at short wavelength, the experimental values, and RANS CFD values have same tendency. All the CFD calculations of the added resistance have been performed for the RIOS containership hull model. Calculations were carried out on a model scale with a scale ratio of 1/83.72. A rectangular computational domain consisting of RIOS container ship model rotated to match the angle of incidence is used in the CFD numerical analysis.

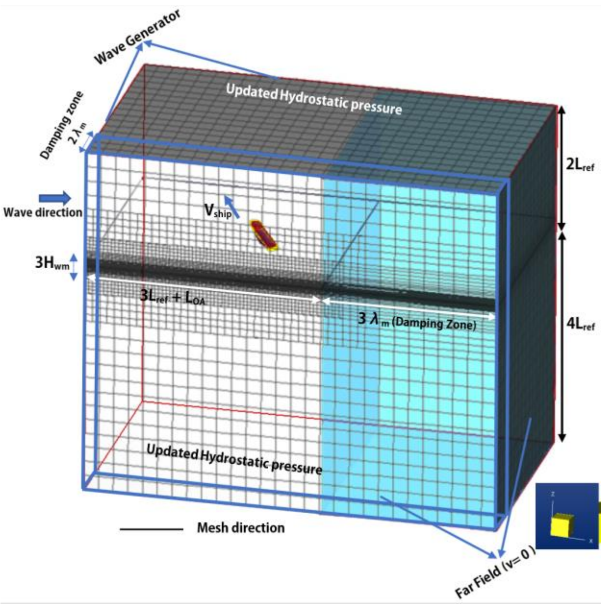

FIGURE 3.19: Meshed computational domain with box refinement and boundary conditions for regular oblique waves generation.

The origin of the computational domain is the hull centerline and the midship on the draft line. The coordinate system, dimensions and boundary conditions applied on computational domain used in this calculation are shown in Fig. 3.19. Here, L_{ref} is set to max (λ_m or L_{ppm}). An imposed motion was applied in the direction of motion of x and y direction with heave, pitch and roll motions solved and all other degrees of freedom remained constraint.

Suitable grid refinement region was set near the free surface as shown in Fig. 3.19. The z-axis direction is usually $1.5H_{wm}$ downward (model ship's wave height $=H_{wm}$) and $1.5H_{wm}$ upward based on the draft line, but when the actual ship's wave height is large (8m or more), there is a possibility that the waves will bounce over the deck and the free surface will exceed the meshed area, so upward direction was set to $2.5\,H_{wm}$ for $H_{ws} \geq$ 8m (actual ship scale wave height $=H_{ws}$).In the grid refinement region near the hull, the grid was made fine so that the regular oblique waves would not be attenuated. Damping zone region grid was made coarser to numerically damp the incident oblique waves. The grid sizes in each region are set $dx = \lambda_{\mathrm{m}}/60$ and $dz = H_{\mathrm{wm}}/16$, generation of oblique regular waves requires 60 cells per model wavelength (λ_{m}) and 16 cells per model wave height (H_{wm}) to propagate the waves on the free surface appropriately. To accurately estimate the total drag resistance, a fine grid must be placed around the hull and transom; this means that the mesh resolution must be high enough at the ship's bow and stern to effectively capture radiated waves, and on the starboard and port sides near the water line to capture incident waves as shown in Fig. 3.19. The system generated the 3rd order Stokes's regular waves model.

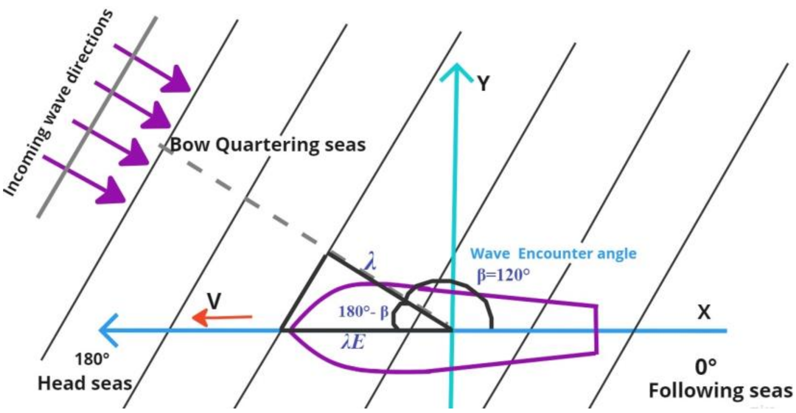

FIGURE 3.20: Schematic diagram of oblique wave encounter by the ship.

Ship's encountered wavelength in oblique waves differs from the applied one. The geometry in Fig. 3.20 is used to calculate the encounter wavelength, where β denotes the oblique wave angle and λ_E denotes the effective wavelength as a result of the oblique encounter. Thus, in head wave direction, if the observed wavelength is λ, in the case of oblique heading with angle β, the resulting wavelength is indicated in Eq. 3.2. The time steps used for these calculations were based on the encounter frequency between ship and waves as given in Table 3.7.

$$\lambda_E = \frac{\lambda}{cos(180^0 - \beta)} \tag{3.2}$$

TABLE 3.7:Time step calculation

λ	λ_E	Wave period	wave frequency	advance frequency	encounter frequency	encounter period	time step
1.25	2.5	1.266	0.789	0.2475	1.0374	0.964	0.0032
2.5	5	1.790	0.558	0.1237	0.6823	1.466	0.0048
3.75	7.5	2.192	0.456	0.0825	0.5385	1.857	0.0061

3.4.1 Discussion of ship motions and resistance results

Calculations are made for the ship motion transfer functions and added resistance of the RIOS containership moving forward in bow quartering waves ($\beta = 120°$). When a ship is traveling in oblique waves as opposed to head waves, the flow field is no longer symmetrical, and the waves are predominantly encountered by one side of the hull. At this time, the ship's rolling motion is now quite obvious, therefore 3 degrees of freedom i.e., heave, roll, and pitch are solved to determine the motions of the ship hull using CFD, and the estimation of added resistance in oblique sea conditions are performed. A potential flow (PF) based solver called EUT results Yoshida et al. (2017)[54] are used to compare the CFD based RAOs of the RIOS container ship motions for linear calculations in order to further support the findings as shown in the Fig 3.21.

Heave and pitch motion RAOs in oblique waves calculated using the present CFD method in linear conditions have shown well agreement with potential theory method results as shown in Fig. 3.21. This indicates that the present numerical method is accurate enough to predict the added resistance calculations at different wave steepness. For roll motion, discrepancies in magnitude are observed between the CFD and PF results for higher wavelength cases. In the case of the oblique bow waves, the encounter frequency decreases as the wavelength increases. Because of this, it is anticipated that the roll responses should gradually rise as the wavelength gets longer and shows maximum amplitude which is close to the ship's roll resonance point where the encounter frequency gets closer to the natural roll frequency as shown in Fig. 3.21.

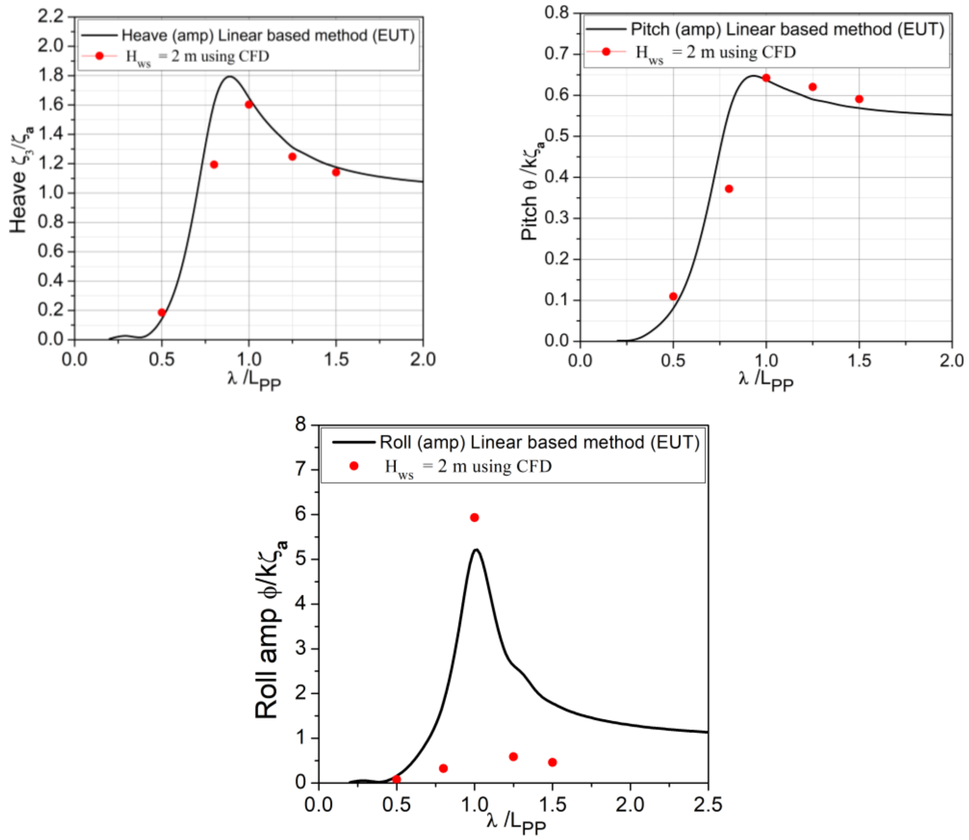

FIGURE 3.21: CFD results of heave ($\zeta 3$), pitch (θ) and roll (φ) RAOs are compared with PF method. where k is the wave number.

The added resistance (R_{aw}) for each CFD simulation cases shown in Table 3.5 is determined by deducting the resistance in calm water (R_{Calm}) from the time-averaged total resistance (R_{Total}) in waves according to Eq. 3.1 The additional calculation was performed at $\lambda/L_{pp} = 0.8, 1.25$ at $H_{ws} = 2m$ to confirm the accuracy of linear ship motion responses.

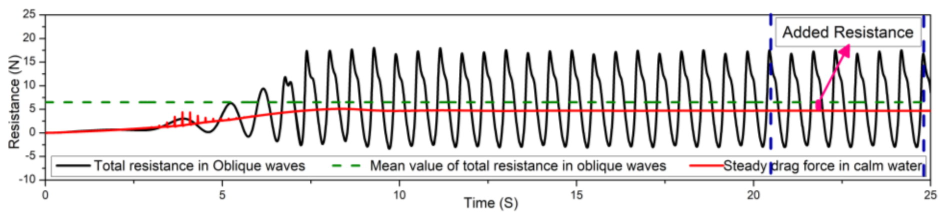

FIGURE 3.22: Calculation of added resistance in Oblique waves at Fn $= 0.25$, $H_{ws} = 5m$ for $\lambda/L_{pp} = 0.5$.

For the added resistance analysis of RIOS containership in oblique regular waves at different wave heights, total resistance in waves was calculated from CFD simulations for short and long wave cases (from case 1~12). Convergence of numerical simulations showed the accuracy of waves after

15s of periods of oscillations as after those numerical results showing repeatability as shown in Fig. 3.22 for the short wavelength case. Similarly, we calculated the added resistance coefficient for all the cases and compare the added resistance coefficient in waves with potential-based theoretical results shown in Figs. 3.24. Free surface animation contour is shown in Fig. 3.23 for short wave case no. 3.

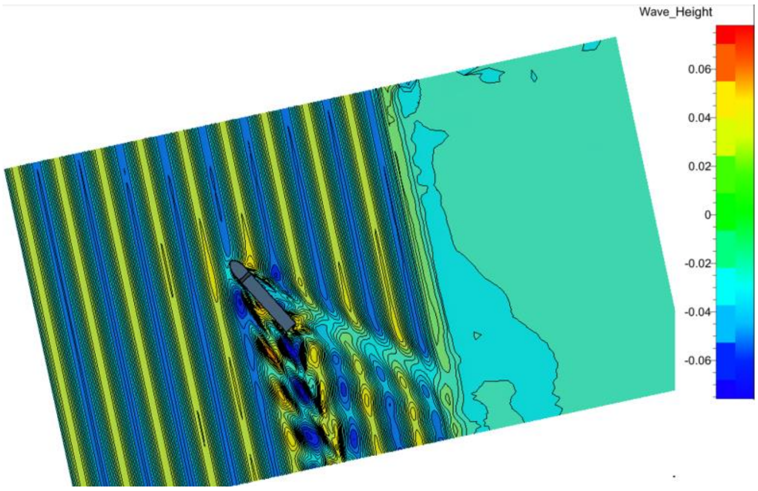

FIGURE 3.23: Free surface contour around ship hull ($\mathrm{Fn} = 0.25, \lambda/L_{pp} = 0.5\ H_{ws} = 5$)

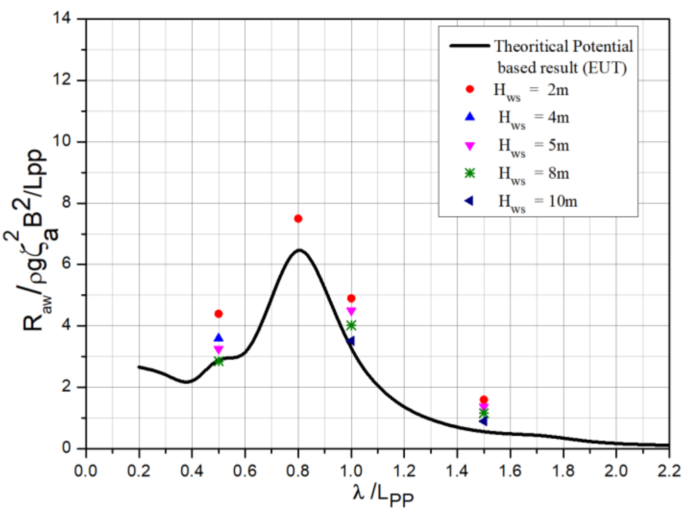

FIGURE 3.24: CFD calculation results of added resistance coefficient compared with potential theory-based method at $\mathrm{Fn} = 0.25$.

In Fig. 3.24, Non-linear effects can be seen at $\lambda/L_{pp} = 0.5$, $\lambda/L_{pp} \geqq 1.0$, the added resistance coefficient decreases as the wave height increases. This indicates that the tendency of the added wave resistance coefficient with respect to the normalized wavelength changes not only quantitatively but also qualitatively depending on the wave height.

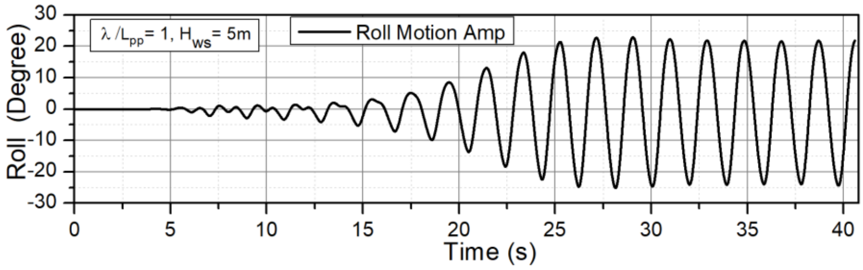

FIGURE 3.25: Time series of roll motion amplitude in $\lambda/L_{pp} = 1$, $H_{ws} = 5m$.

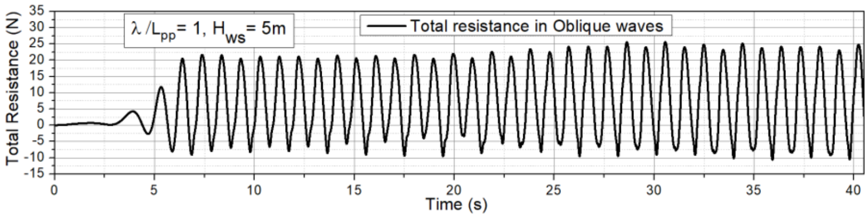

FIGURE 3.26: Time series of total drag resistance in $\lambda/L_{pp} = 1$, $H_{ws} = 5m$.

The results show that in case of wavelength being around ship length, for $\lambda/L_{pp} = 1$, ship's heave and pitch motion mainly account for the principal resistance. Even though there is higher roll motion in larger wave heights (H_{ws}= 5m and 8m) as shown in time series data of roll motion amplitude in case of $H_{ws} = 5m$ for $\lambda/L_{pp} = 1$ in Fig. 3.25 but much larger oscillation in roll motion has slightly increased total drag resistance and no significant variations observed during oscillations as shown in the Fig. 3.26. This is because, in case of resistance prediction, ship hull shape, and heave and pitch motions play most significant role. The higher roll motion is because of the encounter of incoming waves by one side of the hull.

3.5 Characteristics of nonlinearity for wave steepness

To qualitatively see the nonlinearity due to wave height, the ratio with the added resistance coefficient of other wave heights was obtained based on the added resistance in a linear condition of $H_{ws} =$ 2m as follows in Eq. 3.3. This satisfies the linear condition, therefore, $R_{aw}(\omega, 2)$ can be suitable for the denominator of Eq. 3.3.

$$C(s, V) = \frac{R_{aw}(\omega, H_{ws})}{R_{aw}(\omega, 2)}. \tag{3.3}$$

where, $C(s, V)$ or $C(s)$ is a coefficient representing the non-linearity with respect to the wave steepness, and s is the wave steepness defined by the following Eq. 3.4.

$$s = \frac{H}{\lambda}, \qquad \lambda = \frac{2\pi g}{\omega^2} \tag{3.4}$$

λ is the wavelength, and the second equation represents the dispersion relation of the deep-water wave. Since the minimum wavelength-to-ship-length ratio in CFD calculation is 0.5, its wave steepness is

$$s = \frac{H_{ws}}{\lambda} = \frac{2}{0.5L_{pp}} = \frac{2}{104.5} < \frac{1}{50}\ . \tag{3.5}$$

3.5.1 Estimation of correction coefficient in head waves for KCS

The correction coefficient $C(s,V)$ is empirically determined by CFD data which is only valid for KCS hull ship type is defined as the fundamental expression for deriving empirical formula, where a and b are arbitrary constants and α is a function of steepness.

$$C = \exp\{\alpha(\mathrm{Fn} - \ a\ )^b\} \tag{3.6}$$

Based on the data fitting of CFD added resistance coefficient values on different wave steepness and different Froude numbers, empirical expression is derived for correction coefficient

1) $s \le 0.13$, where $s = H_{ws}/\lambda$

$$C(s,V) = C(s,\mathrm{Fn}) = \begin{cases} 1-(1-C_0\ )\exp\{\alpha(\mathrm{Fn}-0.14)^4\} & ,\mathrm{Fn} \ge 0.14 \\ C_0 & ,\mathrm{Fn} < 0.14 \end{cases}$$

2) $s > 0.13$

$$C(s,V) = C(s,\mathrm{Fn}) = C_0 \tag{3.7}$$

Where Eq. 3.8~3.10 valid for both the above cases,

$$\alpha = 10^5(1.7385s^2 + 0.0273s - 0.033) \tag{3.8}$$

$$C_0 = \exp(-245.5390s^2) \tag{3.9}$$

$$\mathrm{Fn} = V/\sqrt{gL_{pp}} \tag{3.10}$$

As you can see in the Fig. 3.27, at $\mathrm{Fn} < 0.14$, Correction coefficient empirical formula gives value equals to $C = C_{0\ at\ \mathrm{Fn}=0.14} = \exp(-245.5390\ s^2)$ Similarly, $\mathrm{C} = \exp(-214.5054\ s^2)$ at $\mathrm{Fn} = 0.20$, and $\mathrm{C} = \exp(-77.3995\ s^2)$ at $\mathrm{Fn} = 0.26$.

$$C = 1 - (1 - C_0)\, exp\{\alpha(Fn - 0.14)^4\} \qquad Fn \geq 0.14$$

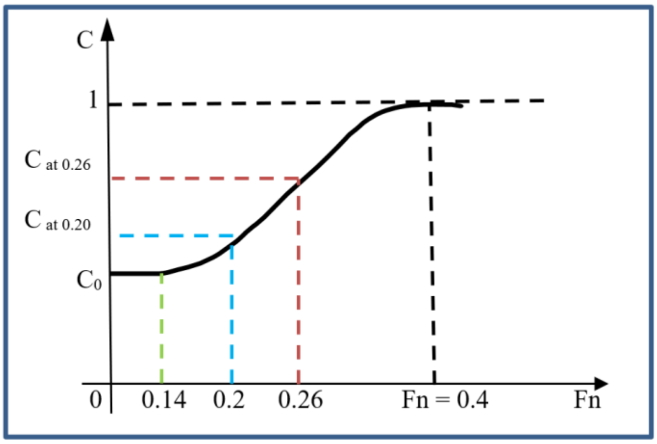

FIGURE 3.27: Illustration of correction coefficient with vs Froude number

In making the approximation curve shown in Fig. 3.28, the data in this short wavelength region was excluded. So, the approximation formula $C(s,V)$ was determined by excluding the non-linear effect of the short-wavelength range $\lambda/L_{pp} = 0.5$.

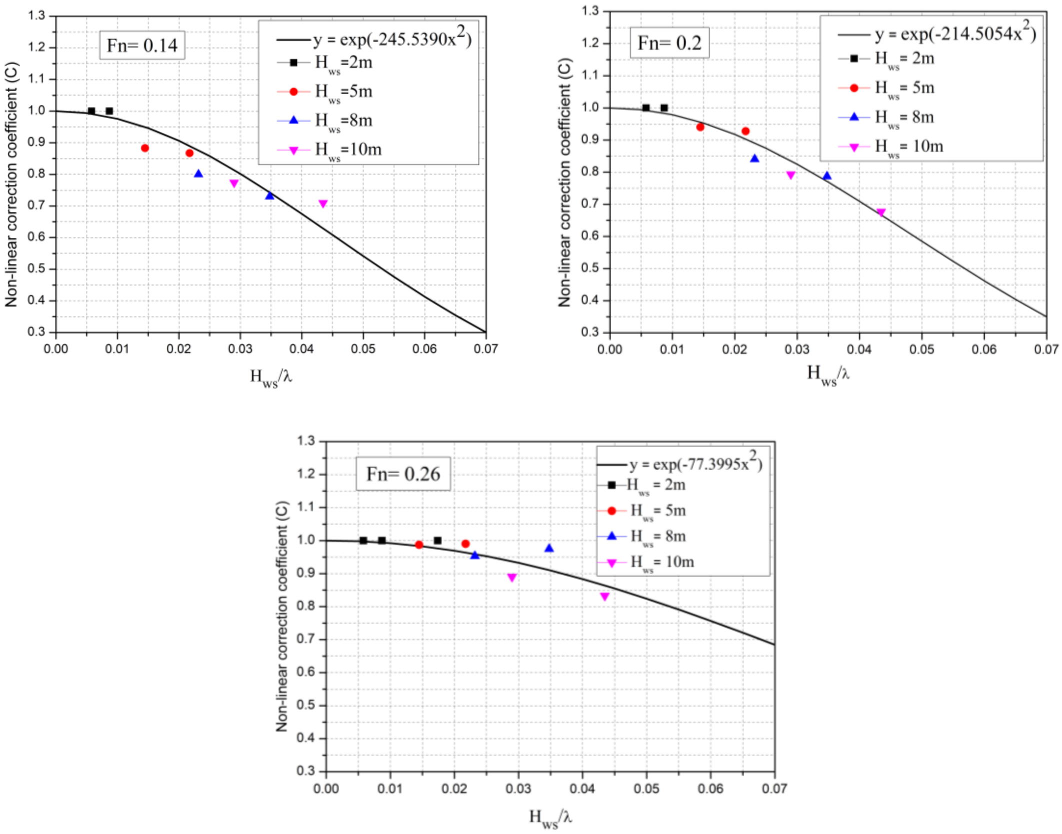

FIGURE 3.28: The approximation of non-linear effect correction coefficient $C(s,V)$ arranged with wave steepness H_{ws}/λ.

Relationship between non-linear effect correction coefficient and ship speed

From the relationship between the non-linearity correction factor and the wave height, the relationship between the correction coefficient $C(s, V)$ and the ship speed (V) was examined next. The relationship between the correction coefficient $C(s, V)$and the Froude number (Fn) derived from the approximate curve drawn in Fig. 3.28 is shown in Fig. 3.29. Based on the assumption that the ship in this study is not expected to operate at speeds higher than Fn $= 0.4$ and that the resistance correction coefficient approaches to 1 as the Froude number increases and the coefficient C can be expressed as a function of the wave steepness (H_{ws}/λ) and the ship speed (Fn) as shown in Eq. 3.7.

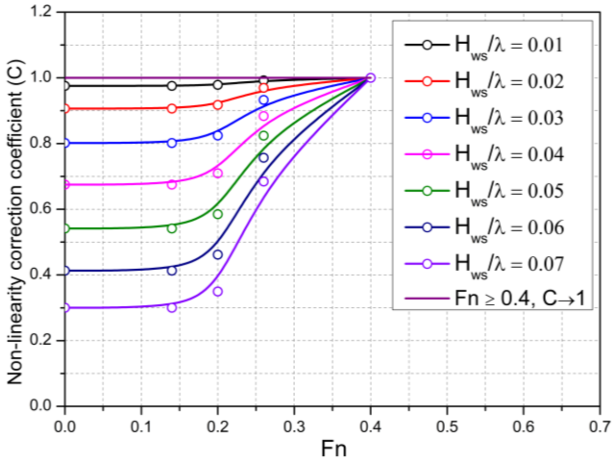

FIGURE 3.29: The correction coefficient for the H_{ws}/λ. input is organized by each Fn.

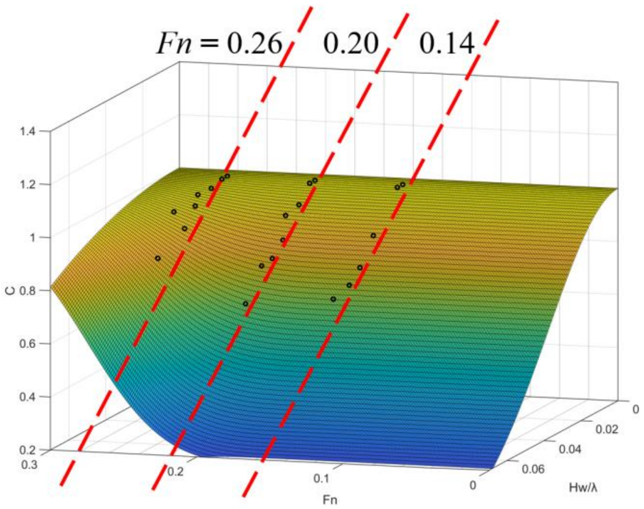

FIGURE 3.30: 3D plot of correction coefficient vs the CFD data

Fig. 3.30 shows the execution of the $C(s, V)$, in which cut sections in the 3D plot shows the approximation curves of non-linear effect correction coefficient at $\mathrm{Fn} = 0.14, 0.20, 0.26$ respectively as shown in Fig. 3.28. The formula is able to track the impact of the variation of different wave heights on added resistance in actual seas and can deal with different speeds and wave steepness.

3.5.2 Estimation of correction coefficient for RIOS hull type

3.5.2.1 In regular head waves

We conducted a survey of the effects of different wave height on added resistance of RIOS containership using CFD in regular waves. The results are shown in Fig. 3.31. Here, wave amplitude ζ_a is proportional to the wave height of incident wave. As the wave height increases, the added wave resistance coefficient K_{aw} decreases. Non-linearity due to wave height is quite evident in the in the short wavelength case λ/L_{pp} =0.5 while the wave height effect is relatively smaller for the long wavelength case λ/L_{pp} =1.5 as compared to short wavelength case. This non-linear tendency seems to be noticeable especially in the short wavelength range.

The correction coefficient $C(s)$ is empirically determined by CFD data which is only valid for RIOS hull ship type is defined as the fundamental expression for deriving empirical formula,

$$C(s) = \exp\{-As^2\} \tag{3.11}$$

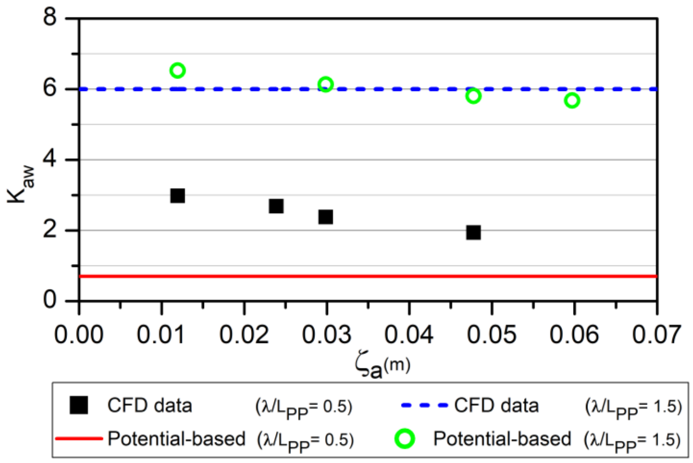

FIGURE 3.31 Effect of wave height on added resistance calculated in regular waves using CFD.

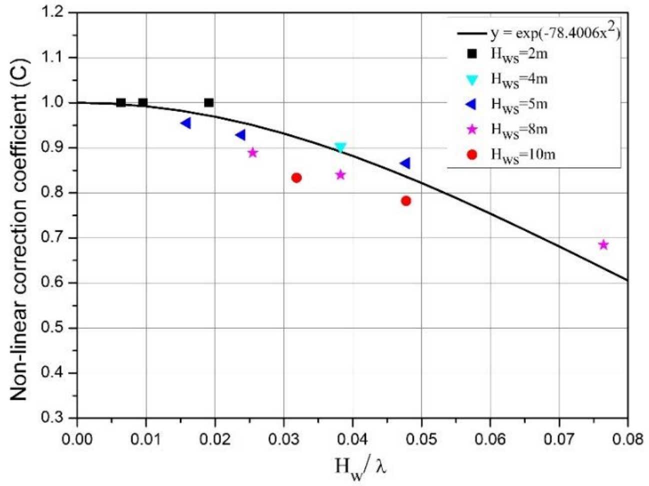

FIGURE 3.32 The approximation of non-linear effect correction coefficient C(s) arranged with wave steepness H_{ws}/λ.

Empirically fitting curve by the exponential function with the ratio of data obtained using Eq 3.3. which is valid for RIOS container ship is shown in Fig. 3.32.

$$C(s) = \exp(-78.4006s^2) \quad (3.12)$$

3.5.2.2 In regular oblique waves

As shown in Fig. 3.33, non-linearity of added resistance was investigated with varying wave steepness for short $\lambda/L_{pp} = 0.5$ and $\lambda/L_{pp} = 1.5$ long wave conditions. Added resistance shows quadratic behavior with increase in the wave height. Also, As the wave height increases, the added wave resistance coefficient decreases. Non-linearity due to wave height is quite evident in the in the short wavelength case λ/L_{pp} =0.5 while the wave height effect is relatively smaller for the long wavelength case λ/L_{pp} =1.5.

Similarly, empirically fitting curve by the exponential function with the ratio of data obtained using Eq 3.3. which is valid for RIOS container ship in oblique bow waves is shown in Fig. 3.34,

$$C(s) = \exp(-110.8836s^2) \quad (3.13)$$

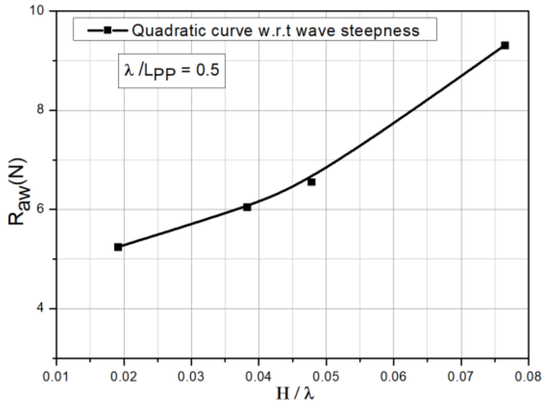

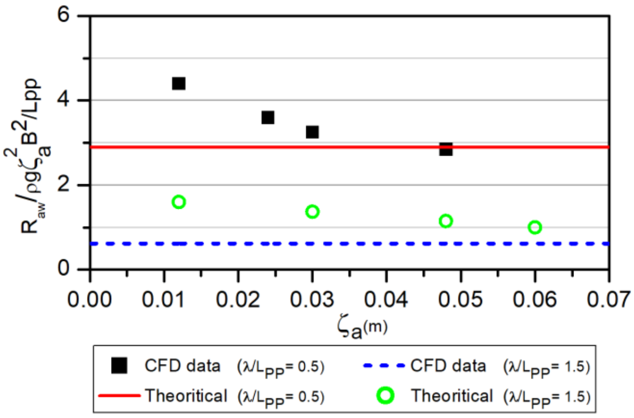

FIGURE 3.33 CFD calculation results of added resistance w.r.t to wave steepness

The nonlinearity of added resistance for wave steepness is characterized in $C(s)$ with increasing wave steepness. This result is applied for the proposed statistical method.

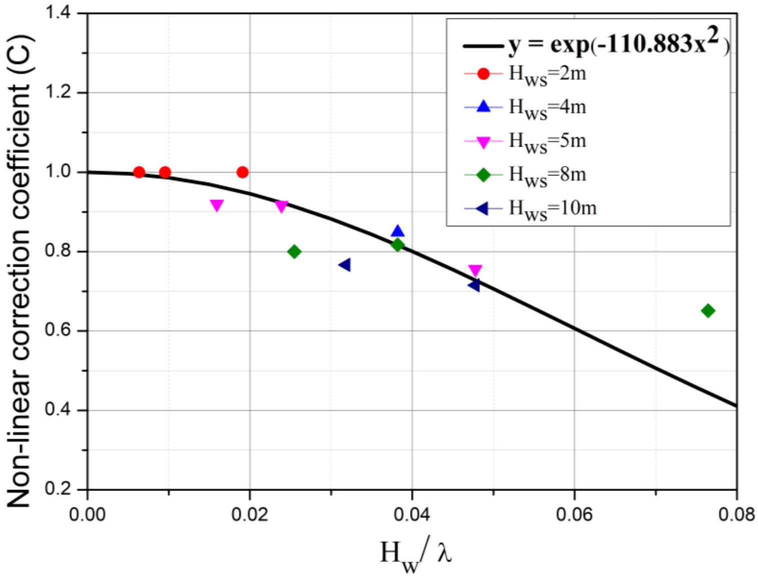

FIGURE 3.34 The approximation of non-linear effect correction coefficient C(s) arranged with wave steepness H_{ws}/λ.

3.6 Conclusion

Numerical simulations of CFD with KCS and RIOS containership in head and oblique sea regular waves under the different wave heights confirmed that added resistance in waves are not proportional to the square of the wave amplitude. The non-linearity with respect to wave height squared was empirically expressed as a "correction coefficient $C(s, V)$ or $C(s)$". Non-linearity due to wave steepness (wave height to wavelength ratio) estimated , was more pronounced in the short wavelength region, and such wave height effects (or wave steepness effects). The validity of a short-term prediction calculation of the added resistance by the spectrum method performed using the square of the incident wave amplitude has been questioned. Hence, these nonlinear effects of wave height and wave steepness are revealed by analyzing the added resistance in irregular waves. It's qualitative and quantitative characteristics are described in Section 5 onwards.

Chapter 4

Direct estimation of added resistance in irregular waves using RANSE based CFD method

4.1 Introduction

In this chapter, formulation of CFD numerical modeling in irregular waves is constructed equivalent to towing tank experiments using RIOS containership model. In order to predict accurately the statistical mean value of the added resistance of large ships in typical seaway conditions, the added resistance in (relatively) very short waves must be predicted accurately. Hence, we used CFD tools which use the very dense grids/small size panels needed to correctly capture the flow changes. Although the direct estimation of average added resistance in irregular seas using RANSE-based CFD requires a high computational cost, but it can deal with the nonlinearity inherently observed in irregular waves. Firstly, the methodology for the generation of irregular wave by the CFD is developed. Parametric study of grid and time step has been performed for the proper generation of irregular waves. Simulated CFD irregular waves are carried for FFT analysis, and the wave spectrum is compared with target wave spectrum. Added resistance results are estimated to validate the proposed non-linear Probability density function method.

4.2 Numerical modelling in irregular head waves

For any numerical analysis, performance of the numerical computation and the accuracy of data can be improved by many factors like, numerical method, boundary conditions, grid size, time interval, etc. In this analysis only grid size, time interval and the turbulence are taken care for improvement which can be modified by the researcher in the numerical computation analysis.

In the numerical simulation on test cases of irregular waves, the overset grid technique was taken to handle the large-amplitude motion of ship in waves and used for complex configuration of computational set up. A computational domains size was determined by a reference length,λ_p which is the wavelength corresponding to the peak wave period T_p. Boundary conditions and a cross-section of the computation mesh are shown in Fig. 4.1. Size of the computational domain proportionally increased with increase in the mean wave period to accurately capture the long wave lengths.

The hull region moves with the ship model and communicates with the background region. The dimensions of the hull region are 1.2 L_{ppm} in x-direction, 0.5L_{ppm} in y-direction, and 0.3L_{ppm} in z-direction, which ensures to cover the range of ship's motion in waves as shown in the Fig. 4.1. 3 degrees of freedom of ship motions were solved and background domain just follows the forward motion of the ship. The weighted average method is used as the interpolation method and mesh is adapted to rigid body motions unlike regular waves. CFD computations were performed equivalent to towing tank experiments set up in which 3 degrees of freedom was solved (heave, pitch, and surge motion) using virtual spring attached with the hull with the help of user defined function in the dynamic library which made the computational setup complex.

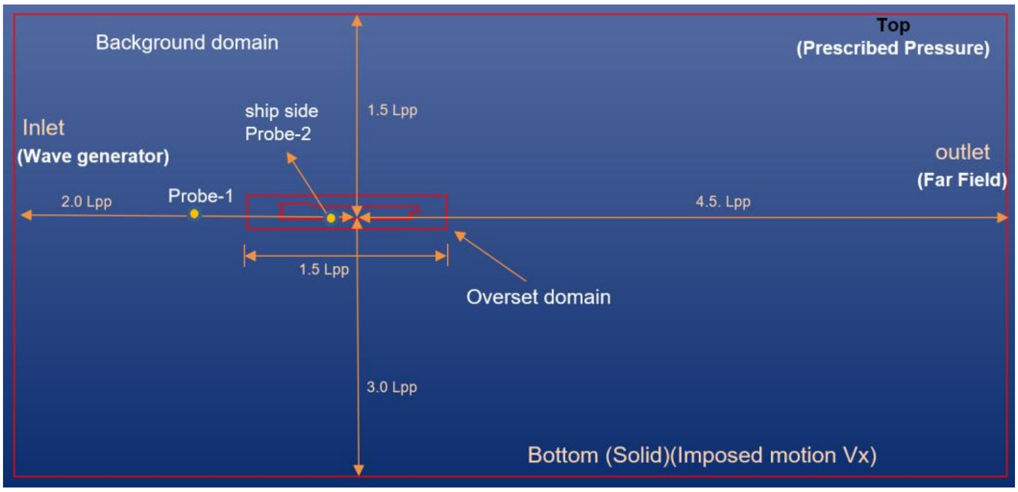

FIGURE 4.1: Computational domain with overset grid technique and boundary conditions for irregular waves generation.

4.2.1 Grid convergence study for irregular waves generation

The process of mesh generation was performed by the built-in meshing tool HEXPRESSTM (v10.1.2). A series of calibrations were performed to satisfy the input wave spectrum with the energy distribution of target wave spectrum by the parametric study of grid refinement and time step. For irregular waves, there is a range of wave lengths where a part of the energy has shorter wavelength than the peak value. For the long-crested irregular waves case, a minimum of 40 cells per peak wavelength corresponding to peak period must be used according to the guidelines for ship CFD seakeeping simulations from ITTC (2011)[12] for reasonable results. The length of time step was about 250 time-step per peak period as it was sufficient to generate accurate waves and to avoid too much amount of damping because larger time step results in wave attenuation. In the numerical wave tank results, 60 cells per peak wavelength and 10 cells per maximum model wave height (1.2 times $H_{1/3m}$) were generated in the z-direction which gave the reasonable results. So, we chose this as a base mesh size for generation of irregular waves.

Three different mesh refinement distributions were tested based on base mesh size at the free surface with a factor of 2 during wave calibration tests as shown in the Table 4.1. The final mesh numbers for each of the mesh convergence cases are listed in Table 4.2.

TABLE 4.1: Grid convergence test cases ($H_{1/3} = 0.024m$,T_{01} = 1.093s)

Type	Total no. of cells (millions)	No of cells per λ_{pm} (x-dir.)	No of cells per $H_{1/3m}$ (z-dir.)	Time step per T_{pm}
Coarse	1.1	30	5	
Base	2.8	60	10	250
Fine	5.9	120	20	

TABLE 4.2: Convergence Analysis on Numerical Mesh and Time Step.

Grid Scheme	Overset (Million)	Background(Million)	Total
Coarse	0.98	1.5	2.48
Base	2.1	3.5	5.60
Fine	3.8	6.3	10.1

Comparison of wave energy density between the model tank tests and CFD simulations results for the test case $H_{1/3} = 0.024$m, $T_{01} = 1.093$s, dt = $T_{pm}/250$ is shown in the Fig. 4.2. $S(\omega)$ is the spectral density obtained by the fast Fourier transform of time series data of wave elevation obtained by CFD and model tank tests. The accuracy of generated waves was evaluated by the measured waves at wave probes located at forward and side position of the ship domain in CFD and model tank tests. In Table 4.3, ratio of zeroth moment between CFD data divided by that of the model tank tests. The zeroth order spectral moment is obtained by Eq. 4.1 for $n = 0$.

$$m_n = \int_0^\infty \omega^n S(\omega) d\omega \tag{4.1}$$

The simulated wave spectrum based on the base grid size provides the favorable agreement with the model tank tests as shown in Fig. 4.2 and Table 4.3 . It is observed that coarse mesh is not able to capture the higher frequency wave components and consequently has lesser energy than base and fine mesh because minimum grid size in the refinement zone is not enough to capture the smaller wavelengths. In case of fine mesh type, irregular wave generation is nearly same with base mesh with some energy loss because grid size is too small in consideration with the time step used in the calculations. Hence, base mesh is suitable with the selected time step.

TABLE 4.3: Study of mesh sensitivity by comparing CFD and tank tests

Type	CFD/EXP ratio (Zeroth moment) %	
	Probe- 1	Probe- 2
Coarse	94	95
Base	98	99
Fine	96	97

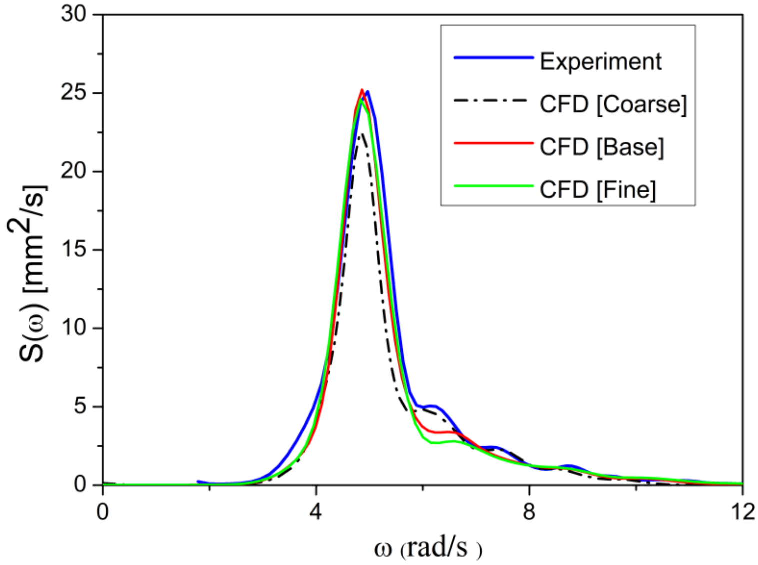

FIGURE 4.2: Comparison of wave spectrum with different grid sizes at probe 1 ($Fn = 0.25$, $H_{1/3} =$ 2m , T_{01} = 10s on full ship scale for $\Delta t = T_p/250$).

The simulation was conducted again for that grid and for different time steps $\Delta t = T_{pm}/200$ and $\Delta t = T_{pm}/300$, in order to assess the influence of the timestep selection in correlation with the spectrum's main parameters and comparison with theoretical wave characteristics was done. Once the wave spectrum analysis with different time steps was obtained, the statistical wave parameters can be derived using the Eq. 4.1. For the timestep sensitivity study as shown in Table 4.4, where it can be clearly seen that the timestep of $T_{pm}/250$ accurately capture the irregular wave and statistical wave characteristics are almost identical with the theoretical wave parameters as compared with smaller and larger time steps. So, the timestep of $T_{pm}/250$ was considered adequate to thoroughly capture the wave transformations. Hence, the results indicate that the proper combination of mesh size and time step has been achieved for the irregular waves generation simulation to calculate added resistance using CFD method.

TABLE 4.4: Study of time step sensitivity

Wave characteristics	$H_{1/3m}$ (m) ($4\sqrt{m_0}$)	T_{01m} (s) ($2\pi m_0/m_1$)
$T_{pm}/200$	0.021	1.12
$T_{pm}/250$	0.026	1.09
$T_{pm}/300$	0.028	1.074
Model tank test at probe 1	0.027	1.036
Theoretical (JONSWAP Spectrum)	0.024	1.093

4.2.2 Overset and adaptive grid technique

A medium mesh system (base mesh) is used for computational domains and in the overset grid system containing overlapping grid domain that surrounds the RIOS containership hull model in the background domain.

TABLE 4.5: Overset domain dimensions

Boundary	Distance	Boundary conditions
Inlet of overset region	$0.75L_{ppm}$	Overset grid
Outlet of overset region	$0.75L_{ppm}$	
Top of overset region	$0.15L_{ppm}$	
Bottom of overset region	$0.15L_{ppm}$	
Side of overset region	$0.15L_{ppm}$	

Mesh is generated in both the domains such that the cells at the boundary of the overlapping domain are as close as possible to the one of the background domains in that area in order to have proper interpolation of information between these domains as shown in the CFD guidelines for overset mesh by Mancini et al., (2017)[32]. Furthermore, at least 3 cells that are required to couple the overset and background regions refers to cell count in the direction normal to the boundary. In general , numerical calculations with an overset grid sometimes cause numerical oscillations and the calculation accuracy may decrease. In order to suppress numerical vibration, it is desirable to have a mesh in which the node points of the background domain and overset domain (overlap area) mesh coincide. Fig. 4.3 shows how the requirement is well met throughout the boundary, having a 1-to-1 ratio between the green colored dotted cell sizes of the overset domain and red solid colored cell sizes of the background domain across the interface.

The free surface box refinements are created in both the domains and the hull surface refinements is added in the overset one. Another box refinement is added in the background domain around the overset domain to comply with the requirement of same cell size in the area around the boundaries of the overset domain.

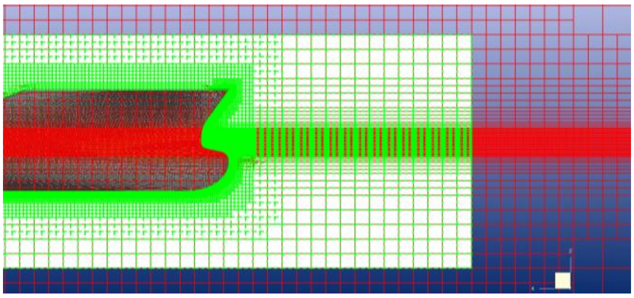

FIGURE 4.3: 1-to-1 ratio between the cell sizes of the two domains across the interface.

Adaptive grid refinement (AGR) technique is used which has the unique compatibility with overset meshing that ensures mesh continuity and reduction of numerical error within the two overlapping meshes. An Adaptive grid refinement algorithm is implemented in the FineMarine flow solver which automatically refines the mesh during the computation. The adaptive refinement is an iterative process in which the mesh is dynamically adapted to the requirements of the solution, during the computation. The decision on where to refine the mesh is based on the physics of the flow. Mesh adaptation is a powerful tool since it can assure the accuracy of overset computations, by smoothing out the transition in cell sizes over the interface between domains. Overset continuity only criterion is used in the simulations. This criterion improves the compatibility between adaptive grid refinement and overset grid and finds the best optimal mesh refinements to ensure a better transfer of data interpolation. The criterion checks the cell size at the overlapping boundaries of each domain and refines the mesh of the other domain, such that its cell sizes are not more than two times larger. If the criterion is used on its own, it only ensures a smooth transition between cell sizes; it cannot be relied upon to refine a very coarse background mesh enough to capture a flow. Therefore, the original meshes in both domains must be reasonably fine already. At least 4 cells are needed for the initial mesh of the background in the region of each overlapping boundary. In practice the background grid usually has to be much finer than that.

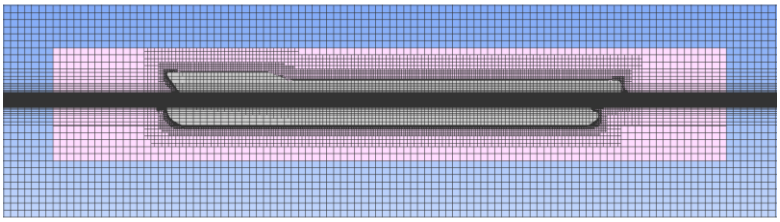

FIGURE 4.4: Overset mesh and mesh background domain

4.3 Numerical simulation set up

When the results were satisfactory with base mesh system, a ship model was included and performed the added resistance calculations. 60 cells per peak wavelength λ_p is necessary to capture the wave components with larger mean wave period in x and y directions but for shorter mean wave period cases, 40 cells per peak wavelength was chosen to keep the simulation size low as the peak wavelength is comparably smaller, otherwise which would have given unreasonable many cells. Required meshed computational domain as shown in Fig. 4.5. The CFD calculation conditions are given in Table 4.6. Case 9 ($H_{1/3m} = 0.060m$, $\mathrm{T_{01m}} = 0.546$s) has been excluded in the calculations as wave steepness is exceeding its limiting condition and resulting in wave breaking.

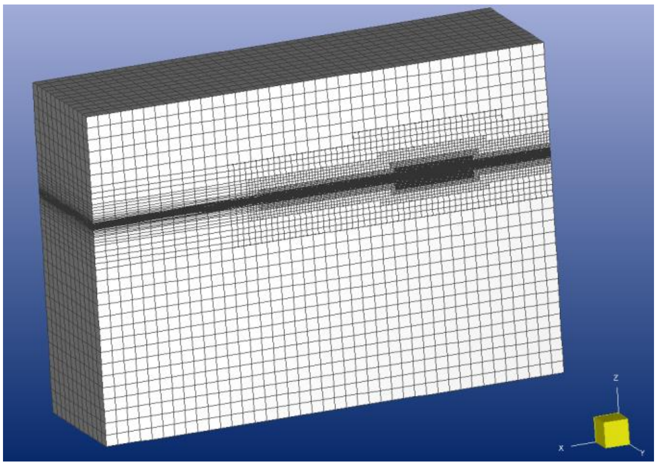

FIGURE 4.5: Mesh Computational domains with free surface box refinements in both the domains for irregular wave generation with adaptive grid refinement technique.

TABLE 4.6: CFD simulation cases in irregular waves at $Fn = 0.25$

CFD cases	$H_{1/3m}$ (m)	T_{01m} (s)
Case 1-8	0.024	0.546, 0.656, 0.765, 0.874, 1.093 ,1.202, 1.530, 1.639
Case 9-16	0.060	

We have analyzed the added resistance in long crested irregular waves using CFD according to the same experimental conditions in the towing tank of the OU facility. The entire calculation area moves forward at a constant speed V_x, and the calculation area and the hull are connected by a spring of spring constant of $K = 70$ N/m and initial tension T_0 of 4.32 N as shown in Fig. 4.6. The bottom of the background domain (Z_{min}) is defined as the solid boundary and is imposed with a half sinusoidal ramp motion law in negative x direction that brings the vessel from zero velocity to the desired speed equivalent to $\mathrm{Fn} = 0.25$. This was performed by dynamic library of the computational setup files where spring constant K and initial tension T_0 in the user customization program (UDP) was defined. As the ship goes in the negative direction of the x-axis, the external force F exerted by the spring on the hull is shown by Eq. 4.2.

$$F = -\{K(x_{bottom} - x_{ship}) + T_0\} \tag{4.2}$$

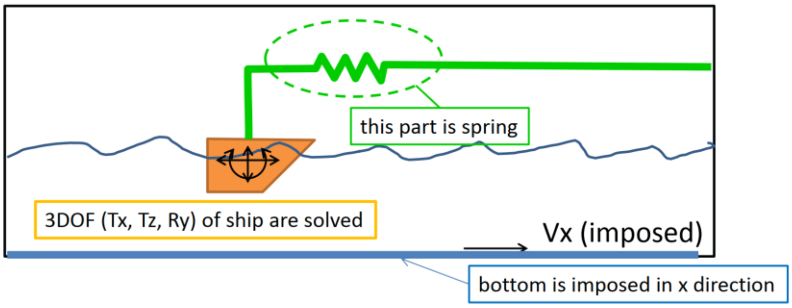

FIGURE 4.6: Schematic diagram of calculation set up in CFD using numerical virtual spring.

4.4 Numerical simulation results

Irregular waves were generated using the JONSWAP wave spectrum by defining the significant wave height $H_{1/3m}$ and peak wave period T_p and peakedness factor $\gamma = 3.3$ in head sea condition. To obtain the converged time range for accurate estimation of added wave resistance, CFD numerical simulations in irregular waves were performed for 100 number of wave periods to encounter for a total time duration, including the release and ramp time to stabilize the initial model motion responses. ITTC (2017)[13] recommends that a minimum of 50 waves should be encountered for model scale tests in irregular waves, while further highlighting encountering 100 waves is preferred to achieve the target wave energy spectrum for the resultant values of the significant wave height and mean wave period. So, larger the wave period, the more is the simulation time to encounter 100 wave periods.

Simulation in calm water condition was performed to check the feasibility of the overset grid strategy with external force controlled by spring defined by user defined program in numerical calculations. To select the valid time range in calm water resistance time series data ,transient range is about 45s at the surge response was observed as shown in the Fig. 4.7 after the applied release and ramp time of 15sec. After 50s ,model surge response got stabilized. So, the starting point of converged time range for the calculation of added resistance in irregular waves is chosen from 50 s at different sea state conditions as shown in Table 4.6.

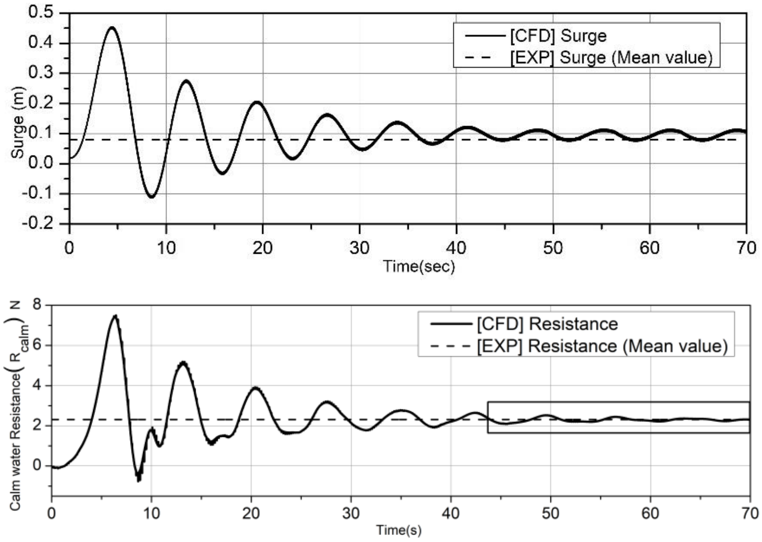

FIGURE 4.7: Comparison of convergence histories of surge motion and drag resistance in calm water conditions ($Fn = 0.25$) between CFD and tank tests , rectangular box: valid time range after transient motion.

Now, total resistance in irregular waves was calculated using CFD for all the cases as shown in Table 4.6 and compared with model tests results. we have shown the calculations for the case 5 and 13 that is for significant wave height $H_{1/3}$ of 2m and 5m for mean wave period T_{01} of 10s in full ship scale conditions. Time series data of total resistance force for ($H_{1/3m} = 0.024m\,, 0.060m$, $\mathrm{T}_{01\mathrm{m}} =$ 1.093s) as shown in Fig. 4.8 in model scale. Average total resistance was calculated by taking the mean after the 50 secs when the model responses got stabilized. The total simulation time window is different for different time periods.

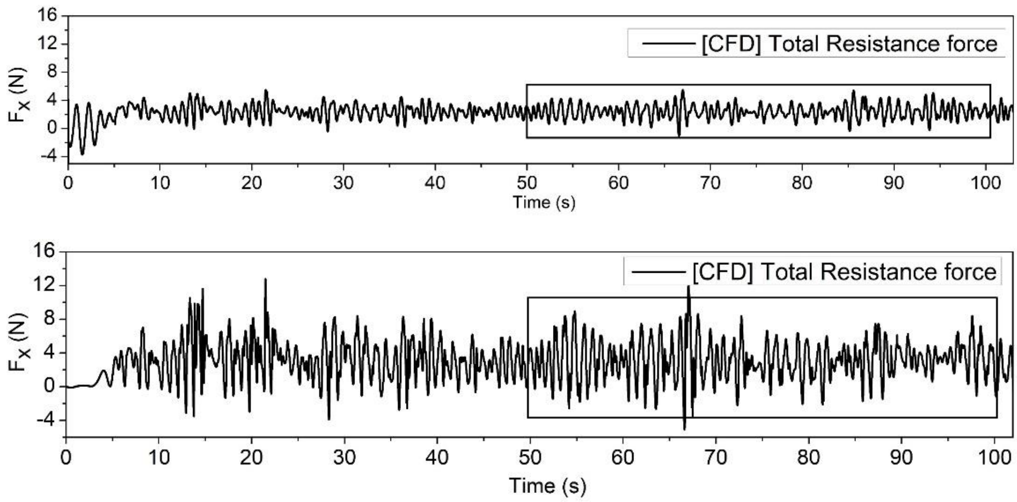

FIGURE 4.8: Time histories of total resistance in irregular waves (head sea, $Fn = 0.25$, $H_{1/3m} =$ 0.024m , $T_{01m} = 1.093$s (top) and $H_{1/3m} = 0.060$m , $T_{01m} = 1.093$s (bottom) , rectangular box: valid time range after transient motion.

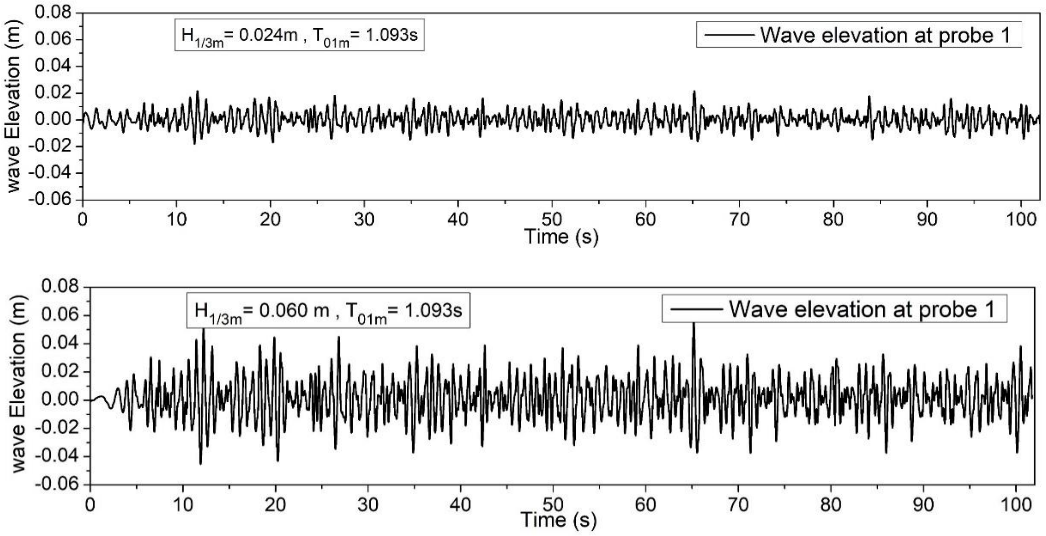

FIGURE 4.9: Time history of measured encountered long-crested irregular waves $H_{1/3m} = 0.024\text{m}$, $T_{01m} = 1.093\text{s}$ (top) and $H_{1/3m} = 0.060\text{m}$, $T_{01m} = 1.093\text{s}$ (bottom).

Wave elevations of irregular wave generation at two sea states are shown in the Fig. 4.9 and compared the wave energy spectrum obtained by Fast Fourier transformation of time series data of CFD irregular wave generation with theoretical JONSWAP spectrum and tank tests energy spectrum shown in Fig 4.10. Free surface contour snapshots in Fig. 4.11 showed that irregular waves appropriately propagate over the entire domain and diffracted waves from the ship moved smoothly toward the wake region and get properly absorbed at the damping zone. Comparing the tank tests and CFD numerical simulation in irregular head sea wave conditions. It was a fair comparison between both, and target wave energy spectrum was achieved with an approximate equivalent to theoretical wave energy spectrum as shown in Fig. 4.10.

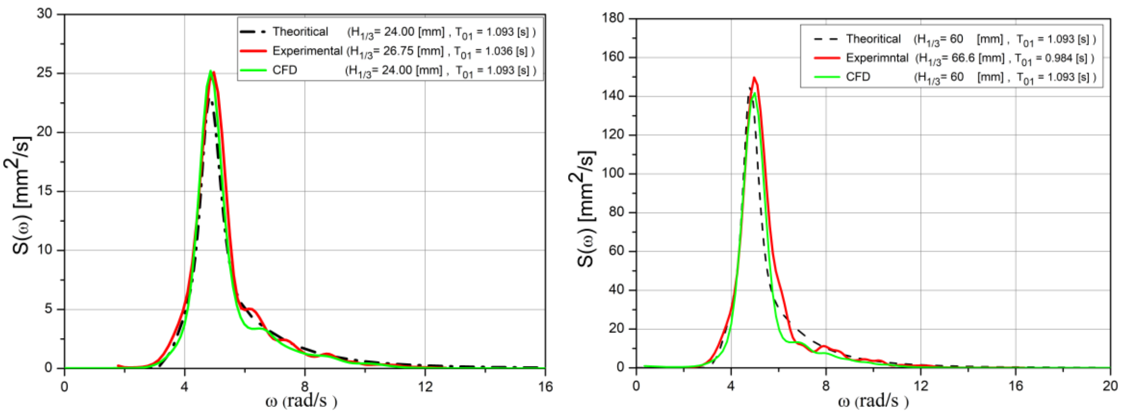

FIGURE 4.10: Comparison of wave energy spectrum based on JONSWAP wave spectrum at $H_{1/3m} = 0.024\text{m}$, $T_{01m} = 1.093\text{s}$ (left) and $H_{1/3m} = 0.060\text{m}$, $T_{01m} = 1.093\text{s}$ (right).

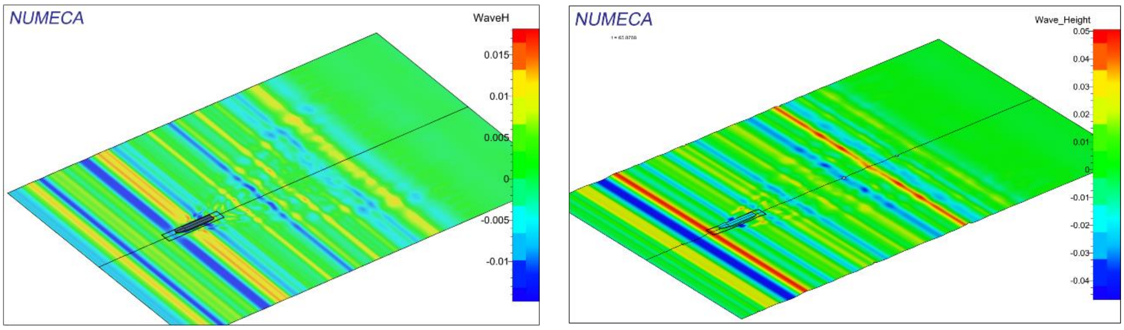

FIGURE 4.11: Free surface contour around ship hull in irregular waves $H_{1/3m} = 0.024$m , $T_{01m} =$ 1.093s (left) and $H_{1/3m} = 0.060$m , $T_{01m} = 1.093$s (right).

4.5 Numerical modelling in irregular oblique bow waves

Although data for irregular oblique wave conditions is scarce , we have shown the reliable results of added resistance both in regular and irregular waves. Direct estimation of added resistance in irregular oblique waves by using RANSE method was performed to validate the proposed non-linear PDF method in oblique sea conditions. The ship model is free to heave, pitch and roll. The weighted mesh deformation technique is used. As for the oblique wave conditions, the best-practice determined from head wave simulations is applied. The computational domain and boundary conditions in the irregular wave resistance cases were the same as those in the regular wave CFD simulations except the wave conditions in which irregular oblique waves were generated using the JONSWAP wave spectrum by defining the significant wave height $H_{1/3m}$ and peak wave period T_p and peakedness factor γ = 3.3 in oblique sea conditions.

TABLE 4.7: CFD simulation cases at $Fn = 0.25$

CFD cases	$H_{1/3m}$ (m)	T_{01m} (s)
Case 1-4	0.024	0.546, 0.656, 1.093, 1.530

The process of mesh generation was performed by the built-in meshing tool HEXPRESS™ (v10.1.2). A series of calibrations were performed to satisfy the input wave spectrum with the energy distribution of target wave spectrum by the parametric study of grid refinement and time step. The length of time step was about 250 time-step per peak period as it was sufficient to generate accurate waves and to avoid too much amount of damping because larger time step results in wave attenuation. In the numerical wave tank results, 60 cells per peak wavelength and 16 cells per maximum model wave height (1.2 times $H_{1/3m}$) were generated in the z-direction which gave the reasonable results. So, we chose this as a base mesh size for generation of oblique irregular waves.

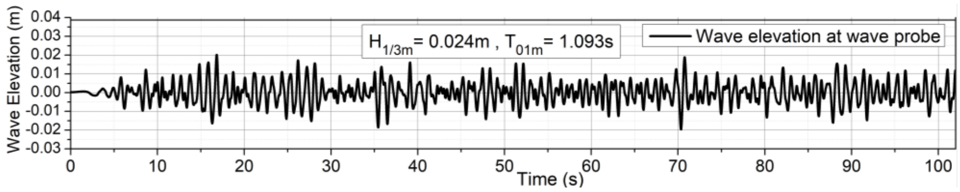

FIGURE 4.12: Time history of measured encountered long-crested irregular waves($H_{1/3}$ = 2m, $T_{01} = 10s$, $Fn = 0.25$ on full ship scale).

Comparison of wave energy density between the theoretical spectrum and numerical spectrum for the test case $H_{1/3} = 0.024$m, $T_{01} = 1.093$s, dt = $T_{pm}/250$ is shown in the Fig. 4.13. $S(\omega)$ is the spectral density obtained by the fast Fourier transform of time series data of wave elevation shown in Fig. 4.12 obtained using numerical wave tank. It shows the fair comparison between both, numerical wave energy spectrum with an approximate equivalent to theoretical wave spectrum.

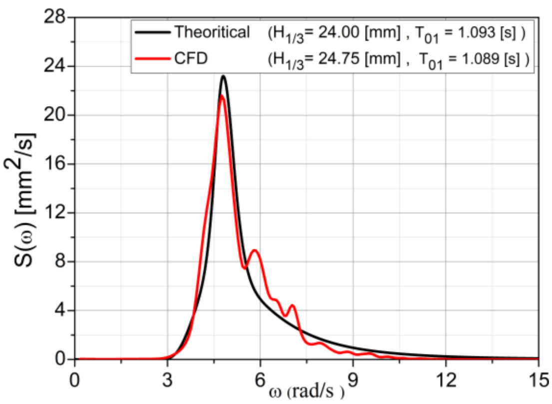

FIGURE 4.13: Comparison of target JONSWAP wave spectrum with measured wave spectrum at $H_{1/3} = 2m$, $T_{01} =$ 10s on full ship scale.

4.6 Numerical results in irregular oblique waves

Now, total resistance in oblique irregular waves was calculated using CFD for all the cases as shown in Table 4.7. we have shown the calculations for the case 3 that is for significant wave height $H_{1/3}$ of 2m for mean wave period T_{01} of 10s in full ship scale conditions.

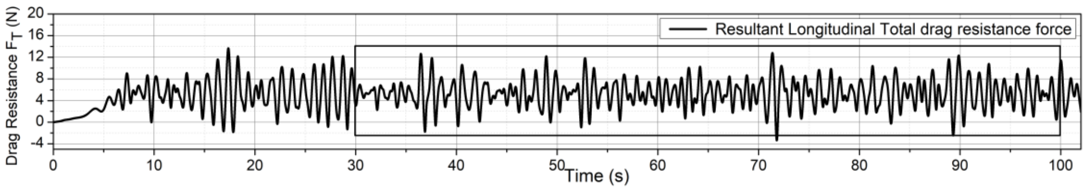

FIGURE 4.14: Time histories of total resistance in irregular waves of Oblique sea conditions, $Fn =$ 0.25, $H_{1/3m} = 0.024$m, $T_{01m} =$ 1.093s rectangular box: valid time range after transient motion.

Time series data of total resistance force as shown in Fig. 4.14 in model scale. Average total resistance was calculated by taking the mean after the 30 secs when the model responses got stabilized.

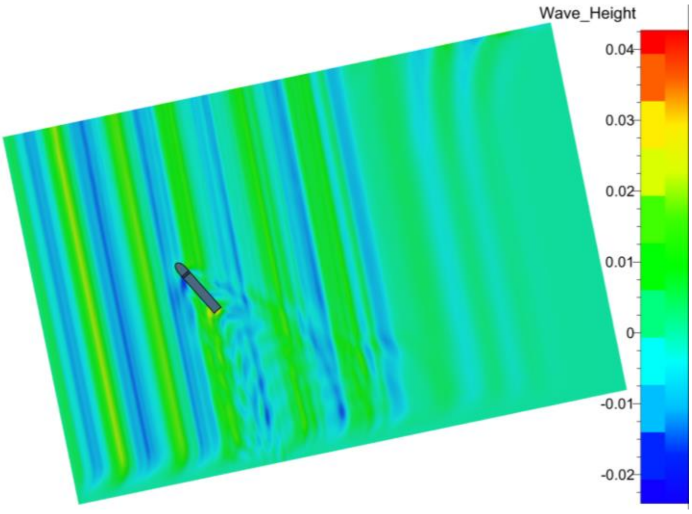

FIGURE 4.14: Free surface contour around ship hull in oblique irregular waves ($Fn = 0.25$, $\mathrm{T_{01m}} = 1.093\mathrm{s}$, $H_{1/3m} = 0.024m$).

4.7 Conclusion

CFD numerical modeling in irregular waves was constructed equivalent to towing tank experiments using RIOS containership model. Although the direct estimation of average added resistance in irregular seas using RANSE-based CFD needed a high computational cost as it used 5 HPC (High Performance Computers) of 32 core each and it took 5-7 days for a calculation to complete for each case. But the RANSE method has an advantage of including non-linearity due to wave height observed in irregular waves and supposed to consider their interactions that is the severe coupled ship motions in harsher sea conditions. Firstly, the methodology for the generation of irregular wave by the CFD was developed. Parametric study of grid and time step was performed for the proper generation of irregular waves. Simulated CFD irregular waves were carried for FFT analysis, and the wave spectrum was compared with target wave spectrum. Obtained added resistance results will be used to validate the proposed non-linear Probability density function method.

Chapter 5

Statistical model

5.1 Introduction

This chapter explained the stochastic approach and probabilistic prediction of ocean waves. We proposed a probability density function method based on the mathematical model in the estimation of added resistance in irregular waves to incorporate the non-linear effect of wave height. The conventional method based on spectral analysis is not applicable for the nonlinearities that occur due to wave height is also presented. First, the introduction of the stochastic approach and significance in random waves has been discussed. In this chapter, mathematical formulation of joint probability density function for wave height and wave period based on Longuet-Higgins model is analytically derived and expressed the probability density functions applicable to wave height, wave period in a given random sea which represent the statistical characteristics of random waves. Then, the comparison with a time series simulated model with JONSWAP spectrum is shown and modified joint probability density function of wave height and wave period with the improvement in the Longuet-Higgins model is proposed.

5.2 Theoretical background

In ocean engineering, it is very important to provide an exact description on ocean surface waves. As evaluation of the properties of random wavers is almost impossible on a wave-by-wave basis in the time domain. However, if we consider the randomly changing waves as a stochastic process, then it is possible to evaluate the statistical properties of waves through the frequency and the probability domains. In the stochastic process approach, waves in deep water are characterized as a Gaussian random process for which the probability distribution of displacement from the mean value (wave profile) obeys the normal probability law. For stochastic prediction of various properties (height, period, etc.) of random/irregular waves, the development of a probability density function applicable for each of these properties is prerequisite. We define the auto-correlation function which yields the variance of random waves in the time domain and provides information necessary for transferring from the time domain to the frequency domain. And from this we can evaluate the wave spectral density function. This provides the mathematical background on which the probabilistic prediction of wave characteristics is based.

5.3 Definitions of wave-height and wave period for wave envelope approach

If we consider the irregular wave envelope as shown in Fig.5.1, the time difference between the zero up crossing point of the wave displacement that appears immediately before the wave crest and the zero up crossing point that appears next to the wave trough is defined as zero up crossing wave period T. The zero up crossing mean wave period T_{02} is defined as the average of wave period T. Significant wave height $H_{1/3}$ is defined as the average of wave height H in the one third distribution region from the one with the highest frequency of occurrence. These are obtained from the narrow bandwidth of ocean waves using the wave spectrum as follows. In addition,T_{01} is sometimes referred to as the "energy mean wave period",T_{02} is not a visually distinctive average wave period, such as

$$H_{1/3} = 4\sqrt{m_0}, \qquad T_{01} = 2\pi\frac{m_0}{m_1}, \qquad T_{02} = 2\pi\sqrt{\frac{m_0}{m_2}}$$

$$m_0 = \int_0^{\infty} S\big(\omega\big|H_{1/3}, T_{01}\big)\, d\omega \tag{5.1}$$

$$m_1 = \int_0^{\infty} \omega S(\omega|H_{1/3}, T_{01})\, d\omega \tag{5.2}$$

$$m_2 = \int_0^{\infty} \omega^2 S(\omega|H_{1/3}, T_{01})\, d\omega \tag{5.3}$$

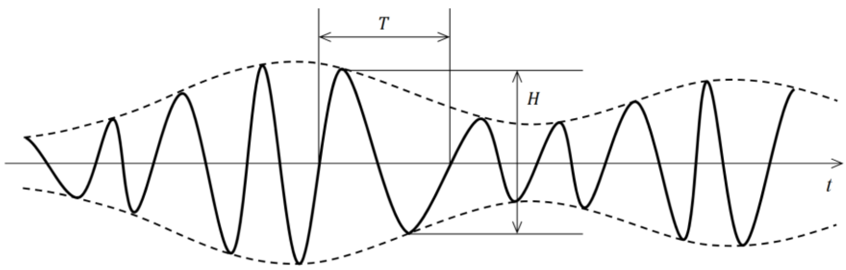

FIGURE 5.1: Definition of envelope of irregular waves, wave height and wave period per wave of wave model expressed by carrier wave proposed by Longuet-Higgins.

Regular waves are represented by wave heights and frequencies that do not vary with time as shown in Fig. 5.2. The solid line represents the wave displacement, and the dashed line is the wave envelope connecting the wave crest (or trough). This regular wave can be expressed by the formula as Eq. 5.4.

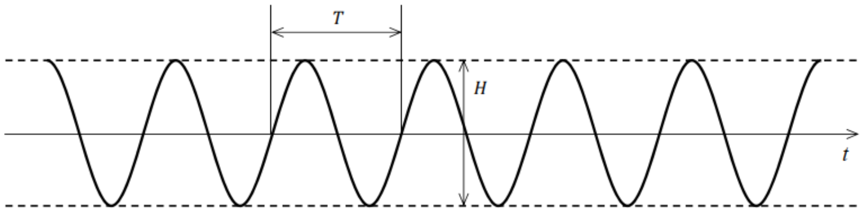

FIGURE 5.2: Definition of envelope of regular waves, of wave height and wave period per wave

$$x(t) = a\cos(\omega t) \tag{5.4}$$

Where,

$$H = 2a, \quad T = \frac{2\pi}{\omega}$$

On the other hand, irregular waves with amplitudes and phases that vary with time expressed as

$$x(t) = \rho(t)\cos(\phi(t) + \omega_m t) \tag{5.5}$$

In case of narrowband waves, the frequency components of the wave lie around the mean wave frequency ω_m. As shown in Fig. 5.1 , $\rho(t)$ represents the envelope height and $\phi(t)$ the phase shift from the mean frequency wave. If we define the wave height and wave period of this wave using the same concept as the regular wave, it will be defined as,

$$H(t) = 2\rho(t), \quad T(t) = \frac{2\pi}{\dot{\phi}(t) + \omega_m} \tag{5.6}$$

The simultaneous expression of probability density function of H and T was theoretically shown by Longuet-Higgins (1975, 1983)[30][31] by defining the envelope of a wave assuming the linearity and narrow bandness of the wave. Ochi (1998)[37] explains this theory in an easy-to-understand manner.

$$f(\zeta,\eta) = \frac{1}{8\sqrt{2\pi}\nu}\left(1+\frac{\nu^2}{4}\right)\left(\frac{\zeta}{\eta}\right)^2 \exp\left(-\frac{\zeta^2}{8}\right)\exp\left(\frac{\zeta^2}{8\nu^2}\left(\frac{1}{\eta}-1\right)^2\right) \tag{5.7}$$

where ζ and η are defined as the dimensionless wave height and wave period respectively, as follows:

$$\zeta = 4\frac{H}{H_{1/3}}, \qquad \eta = \frac{T}{T_{01}} \tag{5.8}$$

ν is the Spectral width parameter and is defined by the following equation.

$$\nu = \left(\frac{m_0 m_2}{{m_1}^2} - 1\right)^{\frac{1}{2}} \tag{5.9}$$

Equation (5.6) is obtained by modeling the time variation of the irregular wave as shown in equation (5.5). The definitions of instantaneous wave heights and periods, in Eq. (5.7) appear to be different from the definitions of wave height and wave period at the beginning of this section, but they are the same, obtained under narrow band conditions.

5.4 Statistics of wave height and wave period in the random seas

5.4.1 Irregular wave time series model and associated statistics.

Assuming that the irregular waves follow a stationary Gaussian process, a time series model of the waves is

$$x(t) = \sum_{n=1}^{\infty} a_n \cos(\omega_n t + \varepsilon_n) = \sum_{n=1}^{\infty} a_n \cos(n\omega_0 t + \varepsilon_n) \tag{5.10}$$

$\omega_0 = \frac{2\pi}{T_D}$, T_D : measurement section ε_n: uniform random phase from 0 to 2π independent of n

Due to the randomness of ε_n, $x(t)$ is a stochastic process. The autocorrelation function of $x(t)$ is given by Eqs. (A30) and (A31) in Appendix section.

$$f = g = x$$

$$b_n = a_n$$

$$\psi_n = \theta_n = 0$$

$$p = m = 0$$

Equation (A34) is the case where

$$C_{xx}(\tau) = \sum_{n=1}^{\infty} \frac{1}{2} a_n a_n \cos n\omega_0 \tau \tag{5.11}$$

The power spectrum of the wave is from equation (A45)

$$S_{xx}(\omega) = \frac{1}{2\pi} \int_{-\infty}^{\infty} C_{xx}(\tau) e^{-i\omega\tau} d\tau = \sum_{n=1}^{\infty} \frac{1}{4} {a_n}^2 \{\delta(\omega - n\omega_0) + \delta(\omega + n\omega_0)\} \tag{5.12}$$

$S_{xx}(\omega)$ is the Double side spectrum. Note that the is a Double side spectrum, $E_{xx}(\omega)$ from equations (A46) to (A48), the zero- to second-order moments for the single side spectrum of

$$m_0 = \int_0^\infty E_{xx}(\omega)d\omega = \int_0^\infty 2S_{xx}(\omega)d\omega = \sum\nolimits_{n=1}^\infty \frac{1}{2}{a_n}^2 \tag{5.13}$$

$$m_1 = \int_0^\infty \omega E_{xx}(\omega)d\omega = \int_0^\infty \omega 2S_{xx}(\omega)d\omega = \sum\nolimits_{n=1}^\infty \frac{1}{2}n\omega_0 {a_n}^2 \tag{5.14}$$

$$m_2 = \int_0^\infty \omega^2 E_{xx}(\omega)d\omega = \int_0^\infty \omega^2 2S_{xx}(\omega)d\omega = \sum\nolimits_{n=1}^\infty \frac{1}{2}(n\omega_0)^2 {a_n}^2 \tag{5.15}$$

m_0 in Equation (5.15) can also be calculated as follows

$$m_0 = C_{xx}(0)$$

The average wave frequency (ω_m) and zero up crossing mean wave frequency (ω_{02}) are defined by the following equations.

$$\omega_{01} = \frac{m_1}{m_0} \tag{5.16}$$

Spectral width parameter is defined as

$$\nu = \left(\frac{m_0 m_2}{{m_1}^2} - 1\right)^{\frac{1}{2}} \tag{5.17}$$

Using these relationships, the probability density function of wave height and wave period is theoretically obtained from the wave spectrum. The wave probability density function is constructed from the wave time series model, while the coefficients of the time series model can be calculated from the wave spectrum by equations (4) to (6). As a result, given the wave spectrum, the expression of probability density function of wave is obtained.

5.4.2 Assumption of stationary Gaussian distribution of wave components centered at mean wave frequency and their covariance

To the stationary Gaussian process in the previous section, we have added the assumption of a narrow-band phenomenon whose frequency components are concentrated around a certain wave frequency ω_c. To demonstrate this, we transform the time series model as follows.

$$x(t) = \sum_{n=1}^{\infty} a_n \cos(\omega_n t + \varepsilon_n)$$
$$= \sum_{n=1}^{\infty} a_n \cos\{(\omega_n - \omega_c)t + \omega_c t + \varepsilon_n\}$$

$$= \sum_{n=1}^{\infty} a_n[\cos\{(\omega_n - \omega_c)t + \varepsilon_n\} \cos \omega_c t - \sin\{(\omega_n - \omega_c)t + \varepsilon_n\} \sin \omega_c t]$$

$$= x_c(t) \cos \omega_c t - x_s(t) \sin \omega_c t \tag{5.18}$$

Here, x_c, x_s are respectively the following expressions.

$$x_c(t) = \sum_{n=1}^{\infty} a_n \cos\{(\omega_n - \omega_c)t + \varepsilon_n\} = \sum_{n=1}^{\infty} a_n \cos\{(n-c)\omega_0 t + \varepsilon_n\} \tag{5.19}$$

$$x_s(t) = \sum_{n=1}^{\infty} a_n \sin\{(\omega_n - \omega_c)t + \varepsilon_n\} = \sum_{n=1}^{\infty} a_n \sin\{(n-c)\omega_0 t + \varepsilon_n\} \tag{5.20}$$

This time derivative is as follows.

$$\dot{x}_c(t) = \sum_{n=1}^{\infty} -a_n(n-c)\omega_0 \sin\{(n-c)\omega_0 t + \varepsilon_n\} \tag{5.21}$$

$$\dot{x}_s(t) = \sum_{n=1}^{\infty} a_n(n-c)\omega_0 \cos\{(n-c)\omega_0 t + \varepsilon_n\} \tag{5.22}$$

From the assumption of a stationary Gaussian process, the joint probability density function of $x_c, x_s, \dot{x}_c, \dot{x}_s$.

$$f(x_c, x_s, \dot{x}_c, \dot{x}_s) = \frac{1}{4\pi^2\sqrt{|\boldsymbol{\Sigma}|}} \exp\left(-\frac{1}{2}\boldsymbol{x}^T\boldsymbol{\Sigma}^{-1}\boldsymbol{x}\right) \tag{5.23}$$

is. where $\boldsymbol{x}$ is the **variable vector** and **$\boldsymbol{\Sigma}$ is the covariance matrix of the variables**, defined as follows:

$$\boldsymbol{x} = [x_c, x_s, \dot{x}_c, \dot{x}_s]^T$$

$$\boldsymbol{\Sigma} = \begin{bmatrix} c_{xcxc} & c_{xcxs} & c_{xc\dot{x}c} & c_{xc\dot{x}s} \\ c_{xsxc} & c_{xsxs} & c_{xs\dot{x}c} & c_{xs\dot{x}s} \\ c_{\dot{x}cxc} & c_{\dot{x}cxs} & c_{\dot{x}c\dot{x}c} & c_{\dot{x}c\dot{x}s} \\ c_{\dot{x}sxc} & c_{\dot{x}sxs} & c_{\dot{x}s\dot{x}c} & c_{\dot{x}s\dot{x}s} \end{bmatrix}$$

In order to express the time-series model of formula of Eq. 5.18 as a combination of amplitude and phase, it is transformed as follows.

$$x(t) = x_c(t) \cos \omega_c t - x_s(t) \sin \omega_c t$$

$$= \mathrm{Re}[\{x_c(t) + ix_s(t)\}\{\cos\omega_c t + i\sin\omega_c t\}]$$

$\rho(t)$ and $\phi(t)$ as real-valued functions

$$\rho(t) = \sqrt{x_c{}^2(t) + x_s{}^2(t)}$$

$$\phi(t) = \tan^{-1}\frac{x_s(t)}{x_c(t)}$$

If we define

$$\rho(t)e^{i\phi(t)} = x_c(t) + ix_s(t) \tag{5.24}$$

Therefore, we obtain the following equation.

$$x(t) = \mathrm{Re}\left[\rho(t)e^{i\phi(t)}e^{i\omega_c t}\right] = \mathrm{Re}\left[\rho(t)e^{i(\phi(t)+\omega_c t)}\right] = \rho(t)\cos(\phi(t) + \omega_c t) \tag{5.25}$$

From this equation, the instantaneous wave amplitude is expressed by $\rho(t)$ and the wave frequency is the time-differentiated argument of the cosine function is represented as

$$\Omega = \dot{\phi}(t) + \omega_c$$

by using these, we define the dimensionless instantaneous wave height and wave period as follows.

$$\zeta = \frac{H}{H_{1/3}} = \frac{H}{4\sqrt{m_0}} = \frac{2\rho(t)}{4\sqrt{m_0}} = \frac{\rho(t)}{2\sqrt{m_0}} \tag{5.26}$$

$$\eta = \frac{T}{T_{01}} = \frac{\omega_{01}}{\Omega} = \frac{\omega_{01}}{\dot{\phi}(t) + \omega_c} \tag{5.27}$$

The range of each variable is from the definition of $\rho, \dot{\phi}$.

$$0 \le \zeta < \infty$$

$$-\infty < \eta < \infty$$

However, since η represents the wave period, it should originally be defined only for positive values. This will be corrected later. By variable transformation of $f(x_c, x_s, \dot{x}_c, \dot{x}_s)$, we obtained $f(\rho, \phi, \dot{\rho}, \dot{\phi})$, by variables contraction, we obtained $f(\rho, \dot{\phi})$, and by further variables transformation, the Joint probability density function of the wave height and the wave period $f(\zeta, \eta)$ is derived.

The autocorrelation and cross-correlation functions of $(x_c, x_s, \dot{x}_c, \dot{x}_s)$ are derived by equations (B1) and (B2) in **Appendix B.**

- Autocovariance of the x_c, x_s is given by c_{xcxc}, c_{xsxs}.

$$c_{xsxs} = c_{xcxc} = \int_0^\infty E_{xx}(\omega)d\omega = m_0 \tag{5.28}$$

- Autocovariance of the $\dot{x}_c, \dot{x}_s$ is given by $c_{\dot{x}c\dot{x}c}, c_{\dot{x}s\dot{x}s}$

$$c_{\dot{x}c\dot{x}c} = \int_0^\infty (\omega - \omega_c)^2 E_{xx}(\omega)d\omega \tag{5.29}$$

The moment order can be divided as follows.

$$c_{\dot{x}c\dot{x}c} = \int_0^\infty \omega^2 E_{xx}(\omega)d\omega - 2\omega_c \int_0^\infty \omega E_{xx}(\omega)d\omega + {\omega_c}^2 \int_0^\infty E_{xx}(\omega)d\omega$$

$$c_{\dot{x}s\dot{x}s} = c_{\dot{x}c\dot{x}c} = m_2 - 2\omega_c m_1 + {\omega_c}^2 m_0 \tag{5.30}$$

- Cross-covariance of the two x_c and $\dot{x}_c$ is given by $c_{xc\dot{x}c}$

$$c_{\dot{x}cxc} = C_{\dot{x}cxc}(0) = 0 \tag{5.31}$$

- Cross covariance of the two x_c and x_s is given by c_{xcxs}.

$$c_{xsxc} = C_{xsxc}(0) = 0 \tag{5.32}$$

- Cross covariance of the two x_c and $\dot{x}_s$ is given by $c_{xc\dot{x}s}$

$$c_{\dot{x}sxc} = C_{\dot{x}sxc}(0) = m_0(\omega_{01} - \omega_c) \tag{5.33}$$

- Cross covariance of the two $\dot{x}_c$ and x_s is given by $c_{\dot{x}cxs}$.

$$c_{xs\dot{x}c} = C_{xs\dot{x}c}(0) = -(\omega_{01} - \omega_c)m_0 \tag{5.34}$$

- Cross covariance of the two $\dot{x}_c$ and $\dot{x}_s$ is given by $c_{\dot{x}c\dot{x}s}$

$$c_{\dot{x}s\dot{x}c} = C_{\dot{x}s\dot{x}c}(0) = 0 \tag{5.35}$$

- Cross covariance of the two x_s and $\dot{x}_s$ is given by $c_{xs\dot{x}s}$

$$c_{\dot{x}sxs} = C_{\dot{x}sxs}(0) = 0 \tag{5.36}$$

5.5 Joint probability density function of wave height and wave period

From the above, the covariance matrix is

$$\mathbf{\Sigma} = \begin{bmatrix} c_0 & 0 & 0 & d \\ 0 & c_0 & -d & 0 \\ 0 & -d & c_2 & 0 \\ d & 0 & 0 & c_2 \end{bmatrix} \tag{5.37}$$

It becomes.

$$c_0 = \int_0^\infty E_{xx}(\omega)d\omega = m_0 \tag{5.38}$$

$$c_2 = \int_0^\infty (\omega - \omega_c)^2 E_{xx}(\omega)d\omega = m_2 - 2\omega_c m_1 + {\omega_c}^2 m_0 \tag{5.39}$$

$$d = m_1 - m_0\omega_c = m_0(\omega_{01} - \omega_c) \tag{5.40}$$

The determinant and inverse of the covariance matrix are as follows,

$$
\begin{aligned}
|\boldsymbol{\Sigma}| &= c_0 \begin{vmatrix} c_0 & -d & 0 \\ -d & c_2 & 0 \\ 0 & 0 & c_2 \end{vmatrix} - d \begin{vmatrix} 0 & c_0 & -d \\ 0 & -d & c_2 \\ d & 0 & 0 \end{vmatrix} \\
&= c_0(c_0c_2c_2 - ddc_2) - d(c_0c_2d - ddd) \\
&= (c_0c_2 - d^2)^2
\end{aligned}
\tag{5.41}
$$

$$
\boldsymbol{\Sigma}^{-1} = |\boldsymbol{\Sigma}|^{-1} \begin{bmatrix}
\begin{vmatrix} c_0 & -d & 0 \\ -d & c_2 & 0 \\ 0 & 0 & c_2 \end{vmatrix} & -\begin{vmatrix} 0 & -d & 0 \\ 0 & c_2 & 0 \\ d & 0 & c_2 \end{vmatrix} & \begin{vmatrix} 0 & c_0 & 0 \\ 0 & -d & 0 \\ d & 0 & c_2 \end{vmatrix} & -\begin{vmatrix} 0 & c_0 & -d \\ 0 & -d & c_2 \\ d & 0 & 0 \end{vmatrix} \\
-\begin{vmatrix} 0 & 0 & d \\ -d & c_2 & 0 \\ 0 & 0 & c_2 \end{vmatrix} & \begin{vmatrix} c_0 & 0 & d \\ 0 & c_2 & 0 \\ d & 0 & c_2 \end{vmatrix} & -\begin{vmatrix} c_0 & 0 & d \\ 0 & -d & 0 \\ d & 0 & c_2 \end{vmatrix} & \begin{vmatrix} c_0 & 0 & 0 \\ 0 & -d & c_2 \\ d & 0 & 0 \end{vmatrix} \\
\begin{vmatrix} 0 & 0 & d \\ c_0 & -d & 0 \\ 0 & 0 & c_2 \end{vmatrix} & -\begin{vmatrix} c_0 & 0 & d \\ 0 & -d & 0 \\ d & 0 & c_2 \end{vmatrix} & \begin{vmatrix} c_0 & 0 & d \\ 0 & c_0 & 0 \\ d & 0 & c_2 \end{vmatrix} & -\begin{vmatrix} c_0 & 0 & 0 \\ 0 & c_0 & -d \\ d & 0 & 0 \end{vmatrix} \\
-\begin{vmatrix} 0 & 0 & d \\ c_0 & -d & 0 \\ -d & c_2 & 0 \end{vmatrix} & \begin{vmatrix} c_0 & 0 & d \\ 0 & -d & 0 \\ 0 & c_2 & 0 \end{vmatrix} & -\begin{vmatrix} c_0 & 0 & d \\ 0 & c_0 & 0 \\ 0 & -d & 0 \end{vmatrix} & \begin{vmatrix} c_0 & 0 & 0 \\ 0 & c_0 & -d \\ 0 & -d & c_2 \end{vmatrix}
\end{bmatrix}^T
$$

$$
= \frac{1}{(c_0c_2 - d^2)^2} \begin{bmatrix}
c_0c_2^2 - c_2d^2 & 0 & 0 & -c_0c_2d + d^3 \\
0 & c_0c_2^2 - c_2d^2 & c_0c_2d - d^3 & 0 \\
0 & c_0c_2d - d^3 & c_0^2c_2 - c_0d^2 & 0 \\
-c_0c_2d + d^3 & 0 & 0 & c_0^2c_2 - c_0d^2
\end{bmatrix}^T
$$

$$
= \frac{1}{c_0c_2 - d^2} \begin{bmatrix}
c_2 & 0 & 0 & -d \\
0 & c_2 & d & 0 \\
0 & d & c_0 & 0 \\
-d & 0 & 0 & c_0
\end{bmatrix}
\tag{5.42}
$$

$E_{xx}(\omega)$ represents the single side spectrum of the wave. Substituting this into equation (5.23), the Joint occurrence probability density function of $x_c, x_s, \dot{x}_c, \dot{x}_s$ is expressed by the following equation.

$$
\begin{aligned}
f(x_c, x_s, \dot{x}_c, \dot{x}_s) &= \frac{1}{\sqrt{2\pi}^4 \sqrt{|\boldsymbol{\Sigma}|}} \exp\left(-\frac{1}{2}\boldsymbol{x}^T\boldsymbol{\Sigma}^{-1}\boldsymbol{x}\right) \\
&= \frac{1}{4\pi^2(c_0c_2 - d^2)} \exp\left(-\frac{1}{2(c_0c_2 - d^2)}\boldsymbol{x}^T \begin{bmatrix}
c_2 & 0 & 0 & -d \\
0 & c_2 & d & 0 \\
0 & d & c_0 & 0 \\
-d & 0 & 0 & c_0
\end{bmatrix} \boldsymbol{x}\right) \\
&= \frac{1}{4\pi^2(c_0c_2 - d^2)} \exp\left(-\frac{1}{2(c_0c_2 - d^2)}\boldsymbol{x}^T \begin{Bmatrix}
c_2x_c - d\dot{x}_s \\
c_2x_s + d\dot{x}_c \\
dx_s + c_0\dot{x}_c \\
-dx_c + c_0\dot{x}_s
\end{Bmatrix}\right)
\end{aligned}
$$

$$= \frac{1}{4\pi^2(c_0c_2 - d^2)} \exp\left(-\frac{x_c(c_2x_c - d\dot{x}_s) + x_s(c_2x_s + d\dot{x}_c) + \dot{x}_c(dx_s + c_0\dot{x}_c) + \dot{x}_s(-dx_c + c_0\dot{x}_s)}{2(c_0c_2 - d^2)}\right)$$

$$= \frac{1}{4\pi^2(c_0c_2 - d^2)} \exp\left(-\frac{c_2(x_c^2 + x_s^2) + 2d(-x_c\dot{x}_s + x_s\dot{x}_c) + c_0(\dot{x}_c^2 + \dot{x}_s^2)}{2(c_0c_2 - d^2)}\right)$$

The variable transformation of the probability density function $(x_c, x_s, \dot{x}_c, \dot{x}_s) \to (\rho, \phi, \dot{\rho}, \dot{\phi})$ is given by the Jacobian

$$f(\rho, \phi, \dot{\rho}, \dot{\phi}) = f(x_c, x_s, \dot{x}_c, \dot{x}_s) \frac{\partial(x_c, x_s, \dot{x}_c, \dot{x}_s)}{\partial(\rho, \phi, \dot{\rho}, \dot{\phi})} \tag{5.43}$$

Specifically, the calculation of the Jacobian is

$$\frac{\partial(x_c, x_s, \dot{x}_c, \dot{x}_s)}{\partial(\rho, \phi, \dot{\rho}, \dot{\phi})} = \det\begin{bmatrix} \frac{\partial x_c}{\partial\rho} & \frac{\partial x_c}{\partial\phi} & \frac{\partial x_c}{\partial\dot{\rho}} & \frac{\partial x_c}{\partial\dot{\phi}} \\ \frac{\partial x_s}{\partial\rho} & \frac{\partial x_s}{\partial\phi} & \frac{\partial x_s}{\partial\dot{\rho}} & \frac{\partial x_s}{\partial\dot{\phi}} \\ \frac{\partial \dot{x}_c}{\partial\rho} & \frac{\partial \dot{x}_c}{\partial\phi} & \frac{\partial \dot{x}_c}{\partial\dot{\rho}} & \frac{\partial \dot{x}_c}{\partial\dot{\phi}} \\ \frac{\partial \dot{x}_s}{\partial\rho} & \frac{\partial \dot{x}_s}{\partial\phi} & \frac{\partial \dot{x}_s}{\partial\dot{\rho}} & \frac{\partial \dot{x}_s}{\partial\dot{\phi}} \end{bmatrix}$$

x_c, x_s are from Eq. 5.24.

$$x_c(t) = \rho(t)\cos\phi(t) \tag{5.44}$$

$$x_s(t) = \rho(t)\sin\phi(t) \tag{5.45}$$

and its time derivative is as follows,

$$\dot{x}_c(t) = \dot{\rho}(t)\cos\phi(t) - \rho(t)\dot{\phi}(t)\sin\phi(t) \tag{5.46}$$

$$\dot{x}_s(t) = \dot{\rho}(t)\sin\phi(t) + \rho(t)\dot{\phi}(t)\cos\phi(t) \tag{5.47}$$

So, if we calculate the Jacobian from these

$$\begin{aligned} \frac{\partial(x_c, x_s, \dot{x}_c, \dot{x}_s)}{\partial(\rho, \phi, \dot{\rho}, \dot{\phi})} &= \det\begin{bmatrix} \cos\phi & -\rho\sin\phi & 0 & 0 \\ \sin\phi & \rho\cos\phi & 0 & 0 \\ -\dot{\phi}\sin\phi & -\dot{\rho}\sin\phi - \rho\dot{\phi}\cos\phi & \cos\phi & -\rho\sin\phi \\ \dot{\phi}\cos\phi & \dot{\rho}\cos\phi - \rho\dot{\phi}\sin\phi & \sin\phi & \rho\cos\phi \end{bmatrix} \\ &= \rho^2 \end{aligned} \tag{5.48}$$

$$f(\rho, \phi, \dot{\rho}, \dot{\phi}) = f(x_c, x_s, \dot{x}_c, \dot{x}_s) \frac{\partial(x_c, x_s, \dot{x}_c, \dot{x}_s)}{\partial(\rho, \phi, \dot{\rho}, \dot{\phi})} = f(x_c, x_s, \dot{x}_c, \dot{x}_s)\rho^2$$

$$f(\rho, \phi, \dot{\rho}, \dot{\phi}) = \frac{\rho^2}{4\pi^2(c_0c_2 - d^2)} \exp\left(-\frac{c_2\rho^2 + 2d(-x_c\dot{x}_s + x_s\dot{x}_c) + c_0(\dot{\rho}^2 + \rho^2\dot{\phi}^2)}{2(c_0c_2 - d^2)}\right)$$

but if we compute the second term of the argument of the exponential function

$$-x_c\dot{x}_s + x_s\dot{x}_c = -\rho\cos\phi\left(\dot{\rho}\sin\phi + \rho\dot{\phi}\cos\phi\right) + \rho\sin\phi\,(\dot{\rho}\cos\phi - \rho\dot{\phi}\sin\phi)$$
$$= -\rho^2\dot{\phi}$$

Therefore,

$$f\left(\rho,\phi,\dot{\rho},\dot{\phi}\right) = \frac{\rho^2}{4\pi^2(c_0c_2-d^2)}\exp\left(-\frac{c_2\rho^2 - 2d\rho^2\dot{\phi} + c_0\left(\dot{\rho}^2+\rho^2\dot{\phi}^2\right)}{2(c_0c_2-d^2)}\right) \tag{5.49}$$

where, $0 \le \rho < \infty, -\infty < \dot{\rho} < \infty, 0 \le \phi \le 2\pi, -\infty < \dot{\phi} < \infty$

$\dot{\rho}$ and ϕ are integrated over the entire region,

$$f\left(\rho,\dot{\phi}\right) = \int_{-\infty}^{\infty}\int_0^{2\pi} f\left(\rho,\phi,\dot{\rho},\dot{\phi}\right)d\phi\,d\dot{\rho}$$

$$= \int_{-\infty}^{\infty}\int_0^{2\pi}\frac{\rho^2}{4\pi^2(c_0c_2-d^2)}\exp\left(-\frac{c_2\rho^2 - 2d\rho^2\dot{\phi} + c_0\left(\dot{\rho}^2+\rho^2\dot{\phi}^2\right)}{2(c_0c_2-d^2)}\right)d\phi\,d\dot{\rho}$$

$$= \frac{\rho^2}{2\pi(c_0c_2-d^2)}\exp\left(-\frac{c_2\rho^2 - 2d\rho^2\dot{\phi} + c_0\rho^2\dot{\phi}^2}{2(c_0c_2-d^2)}\right)\int_{-\infty}^{\infty}\exp\left(-\frac{c_0\dot{\rho}^2}{2(c_0c_2-d^2)}\right)d\dot{\rho}$$

$$= \frac{\rho^2}{2\pi(c_0c_2-d^2)}\exp\left(-\frac{c_2\rho^2 - 2d\rho^2\dot{\phi} + c_0\rho^2\dot{\phi}^2}{2(c_0c_2-d^2)}\right)\sqrt{\pi\frac{2(c_0c_2-d^2)}{c_0}}$$

$$= \frac{\rho^2}{\sqrt{2\pi c_0(c_0c_2-d^2)}}\exp\left(-\frac{c_2\rho^2 - 2d\rho^2\dot{\phi} + c_0\rho^2\dot{\phi}^2}{2(c_0c_2-d^2)}\right)$$

$$= \frac{\rho^2}{\sqrt{2\pi c_0(c_0c_2-d^2)}}\exp\left(-\frac{\rho^2}{2(c_0c_2-d^2)}\left(c_2 - 2d\dot{\phi} + c_0\dot{\phi}^2\right)\right)$$

$$= \frac{\rho^2}{\sqrt{2\pi c_0(c_0c_2-d^2)}}\exp\left(-\frac{c_2\rho^2}{2(c_0c_2-d^2)}\right)\exp\left(-\frac{\rho^2}{2(c_0c_2-d^2)}\left(-2d\dot{\phi} + c_0\dot{\phi}^2\right)\right)$$

$$= \frac{\rho^2}{\sqrt{2\pi c_0(c_0c_2-d^2)}}\exp\left(-\frac{c_2\rho^2}{2(c_0c_2-d^2)}\right)\exp\left(-\frac{c_0\rho^2}{2(c_0c_2-d^2)}\left(-\frac{2d}{c_0}\dot{\phi} + \dot{\phi}^2\right)\right) \tag{5.50}$$

This is obtained, however,

$$\int_{-\infty}^{\infty}\exp\left(-\frac{x^2}{a}\right)dx = \sqrt{\pi a}$$

using this relationship, where $(c_0c_2-d^2)/c_0^2$ is organized as

$$\frac{c_0c_2-d^2}{c_0^2} = \frac{m_0(m_2 - 2\omega_c m_1 + {\omega_c}^2 m_0) - m_0^2(\omega_{01}-\omega_c)^2}{m_0^2}$$

$$= \frac{1}{m_0^2}\{m_0(m_2 - 2\omega_c m_1 + \omega_c{}^2 m_0) - m_0^2(\omega_{01} - \omega_c)^2\}$$
$$= \frac{1}{m_0^2}\{m_0(m_2 - 2\omega_c m_1 + \omega_c{}^2 m_0) - m_0^2(\omega_{01}^2 - 2\omega_{01}\omega_c + \omega_c^2)\}$$
$$= \frac{1}{m_0}\{m_2 - 2\omega_c m_1 + \omega_c{}^2 m_0 - m_0\omega_{01}^2 + 2m_0\omega_{01}\omega_c - m_0\omega_c^2\}$$
$$= \frac{1}{m_0}\{m_2 - 2\omega_c m_1 - m_0\omega_{01}^2 + 2m_0\omega_{01}\omega_c\}$$
$$= \frac{1}{m_0}\{m_2 - 2\omega_c m_1 - m_0\omega_{01}^2 + 2m_1\omega_c\}$$
$$= \frac{1}{m_0}\{m_2 - m_0\omega_{01}^2\}$$
$$= \omega_{01}^2\left(\frac{m_2}{m_0\omega_{01}^2} - 1\right)$$
$$= \omega_{01}^2\left(\frac{m_2 m_0}{m_1^2} - 1\right)$$
$$= \omega_{01}{}^2\nu^2 \tag{5.51}$$

however, it is applied

$$\nu = \left(\frac{m_2 m_0}{m_1^2} - 1\right)^{\frac{1}{2}} \tag{5.52}$$

From this we get,

$$f(\rho, \dot{\phi}) = \frac{\rho^2}{\sqrt{2\pi c_0^3 \omega_{01}{}^2\nu^2}} \exp\left(-\frac{c_2\rho^2}{2c_0^2\omega_{01}{}^2\nu^2}\right) \exp\left(-\frac{\rho^2}{2c_0\omega_{01}{}^2\nu^2}\left(-\frac{2d}{c_0}\dot{\phi} + \dot{\phi}^2\right)\right)$$

Moreover,

$$\frac{d}{c_0} = \frac{m_0(\omega_{01} - \omega_c)}{m_0} = \omega_{01} - \omega_c = \omega_{01}\left(1 - \frac{\omega_c}{\omega_{01}}\right) = \omega_{01}\kappa \tag{5.53}$$

$$\kappa = 1 - \frac{\omega_c}{\omega_{01}} \tag{5.54}$$

Then, the following formula is obtained.

$$f(\rho, \dot{\phi}) = \frac{\rho^2}{\sqrt{2\pi c_0^3 \omega_{01}{}^2\nu^2}} \exp\left(-\frac{c_2\rho^2}{2c_0^2 c_0^3\omega_{01}{}^2\nu^2}\right) \exp\left(-\frac{\rho^2}{2c_0 c_0^3\omega_{01}{}^2\nu^2}\left(-2\omega_{01}\kappa\dot{\phi} + \dot{\phi}^2\right)\right)$$

$$= \frac{\rho^2}{\sqrt{2\pi c_0^3 c_0^3 {\omega_{01}}^2 \nu^2}} \exp\left(-\frac{c_2 \rho^2}{2c_0^2 c_0^3 {\omega_{01}}^2 \nu^2}\right) \exp\left(-\frac{\rho^2}{2c_0 c_0^3 {\omega_{01}}^2 \nu^2}\left(\left(\dot{\phi} - \omega_{01}\kappa\right)^2 - c_0^3 {\omega_{01}}^2 \kappa^2\right)\right)$$

$$= \frac{\rho^2}{\sqrt{2\pi c_0^3 c_0^3 {\omega_{01}}^2 \nu^2}} \exp\left(-\frac{\rho^2}{2c_0 c_0^3 {\omega_{01}}^2 \nu^2}\left(\frac{c_2}{c_0} - c_0^3 {\omega_{01}}^2 \kappa^2\right)\right) \exp\left(-\frac{\rho^2}{2c_0 c_0^3 {\omega_{01}}^2 \nu^2}\left(\dot{\phi} - \omega_{01}\kappa\right)^2\right)$$

Furthermore, if we organize c_2/c_0

$$\frac{c_2}{c_0} = \frac{m_2 - 2\omega_c m_1 + {\omega_c}^2 m_0}{m_0} = {\omega_{01}}^2\left(\frac{m_2 m_0}{m_1^2} - 1 + \kappa^2\right) = {\omega_{01}}^2(\nu^2 + \kappa^2) \tag{5.55}$$

So, applying this

$$f(\rho, \dot{\phi}) = \frac{\rho^2}{\sqrt{2\pi c_0^3 c_0^3 {\omega_{01}}^2 \nu^2}} \exp\left(-\frac{\rho^2}{2c_0 c_0^3 {\omega_{01}}^2 \nu^2}({\omega_{01}}^2(\nu^2 + \kappa^2) - {\omega_{01}}^2 \kappa^2)\right) \exp\left(-\frac{\rho^2}{2c_0 {\omega_{01}}^2 \nu^2}\left(\dot{\phi} - \omega_{01}\kappa\right)^2\right)$$

$$= \frac{\rho^2}{\sqrt{2\pi c_0^3 {\omega_{01}}^2 \nu^2}} \exp\left(-\frac{\rho^2}{2c_0}\right) \exp\left(-\frac{\rho^2}{2c_0 {\omega_{01}}^2 \nu^2}\left(\dot{\phi} - \omega_{01}\kappa\right)^2\right) \tag{5.56}$$

From this equation, by transforming the variables in equations (5.26) and (5.27) $(\rho, \dot{\phi}) \to (\zeta, \eta)$,it becomes $f(\zeta, \eta)$

$$f(\zeta, \eta) = f(\rho, \dot{\phi}) \frac{\partial(\rho, \dot{\phi})}{\partial(\zeta, \eta)}$$

The results obtained from equations (5.26) and (5.27) are as follows,

$$\rho(t) = \frac{4\sqrt{m_0}}{2}\zeta(t) \ = 2\sqrt{c_0}\zeta(t) \tag{5.57}$$

$$\dot{\phi}(t) = \left(\frac{1}{\eta(t)} - \frac{\omega_c}{\omega_{01}}\right)\omega_{01} \tag{5.58}$$

and the Jacobian is

$$\frac{\partial(\rho, \dot{\phi})}{\partial(\zeta, \eta)} = \det\begin{bmatrix} \frac{\partial \rho}{\partial \zeta} & \frac{\partial \rho}{\partial \eta} \\ \frac{\partial \dot{\phi}}{\partial \zeta} & \frac{\partial \dot{\phi}}{\partial \eta} \end{bmatrix} = \det\begin{bmatrix} 2\sqrt{c_0} & 0 \\ 0 & -\frac{\omega_{01}}{\eta^2} \end{bmatrix} = \frac{2\sqrt{c_0}}{\eta^2}\omega_{01} \tag{5.59}$$

Applying these to the equation (5.56) and rearranging, it gives the following equation.

$$f(\zeta,\eta) = f(\rho,\dot{\phi})\frac{\partial(\rho,\dot{\phi})}{\partial(\zeta,\eta)}$$

$$= \frac{\left(2\sqrt{c_0}\zeta\right)^2}{\sqrt{2\pi c_0^3 {\omega_{01}}^2 \nu^2}} \exp\left(-\frac{\left(2\sqrt{c_0}\zeta\right)^2}{2c_0}\right) \exp\left(-\frac{\left(2\sqrt{c_0}\zeta\right)^2}{2c_0 {\omega_{01}}^2 \nu^2}\left(\left(\frac{1}{\eta}-\frac{\omega_c}{\omega_{01}}\right)\omega_{01} - \omega_{01}\kappa\right)^2\right)\frac{2\sqrt{c_0}}{\eta^2}\omega_{01}$$

$$= \frac{8}{\sqrt{2\pi}\,\nu}\left(\frac{\zeta}{\eta}\right)^2 \exp(-2\zeta^2)\exp\left(-\frac{2\zeta^2}{\nu^2}\left(\left(\frac{1}{\eta}-\frac{\omega_c}{\omega_{01}}\right)-\kappa\right)^2\right)$$

$$\boldsymbol{f(\zeta,\eta) = \frac{8}{\sqrt{2\pi}\,\nu}\left(\frac{\zeta}{\eta}\right)^2 \exp\left(-2\zeta^2\right)\exp\left(-2\frac{\zeta^2}{\nu^2}\left(\frac{1}{\eta}-1\right)^2\right)} \tag{5.60}$$

Longuet -Higgins assumed the period of the carrier wave to be the mean wave period, but from this result it can be seen that the results are the same even if any period is used. That is, the setting of the carrier wave is a means for deriving the solution, and the probability density function does not depend on the setting of the carrier wave.

5.5.1 Probability density function of wave height

Integrating equation (5.60) over the entire region with respect to η,

$$f(\rho) = \int_{-\infty}^{\infty} f(\rho,\dot{\phi})d\dot{\phi}$$

$$= \int_{-\infty}^{\infty} \frac{\rho^2}{\sqrt{2\pi c_0^3 {\omega_{01}}^2 \nu^2}} \exp\left(-\frac{\rho^2}{2c_0}\right)\exp\left(-\frac{\rho^2}{2c_0 {\omega_{01}}^2 \nu^2}\left(\dot{\phi}-\omega_{01}\kappa\right)^2\right)d\dot{\phi}$$

$$= \frac{\rho^2}{\sqrt{2\pi c_0^3 {\omega_{01}}^2 \nu^2}} \exp\left(-\frac{\rho^2}{2c_0}\right)\int_{-\infty}^{\infty} \exp\left(-\frac{\rho^2}{2c_0 {\omega_{01}}^2 \nu^2}\left(\dot{\phi}-\omega_{01}\kappa\right)^2\right)d\dot{\phi}$$

$$= \frac{\rho^2}{\sqrt{2\pi c_0^3 {\omega_{01}}^2 \nu^2}} \exp\left(-\frac{\rho^2}{2c_0}\right)\frac{\sqrt{2\pi c_0 {\omega_{01}}^2 \nu^2}}{\rho}$$

$$= \frac{\rho}{c_0}\exp\left(-\frac{\rho^2}{2c_0}\right) \tag{5.61}$$

Obtained as follows, note that the calculation of the integral requires following integral equation.

$$\int_{-\infty}^{\infty} a\exp(-(t-\mu)^2)\,dt = \sqrt{\frac{2\pi}{a}}$$

The relationship used in equation (5.61) is the Rayleigh probability density function. Furthermore, the variable transformation of equation (5.57) yields the following equation.

$$f(\zeta) = f(\rho)\left|\frac{\partial\rho}{\partial\zeta}\right|$$

$$= \frac{2\sqrt{c_0}\zeta}{c_0}\exp\left(-\frac{\left(2\sqrt{c_0}\zeta\right)^2}{2c_0}\right)2\sqrt{c_0}$$

$$= 4\zeta\exp(-2\zeta^2) \qquad (5.62)$$

5.5.2 Probability density function of wave period

Integrating equation (5.60) over the entire region with respect to ρ,

$$f(\dot{\phi}) = \int_0^\infty f(\rho,\dot{\phi})d\rho$$

$$= \int_0^\infty \frac{\rho^2}{\sqrt{2\pi c_0^3 {\omega_{01}}^2\nu^2}}\exp\left(-\frac{\rho^2}{2c_0}\right)\exp\left(-\frac{\rho^2}{2c_0{\omega_{01}}^2\nu^2}\left(\dot{\phi}-\omega_{01}\kappa\right)^2\right)d\rho$$

$$= \frac{1}{\sqrt{2\pi c_0^3 {\omega_{01}}^2\nu^2}}\int_0^\infty \rho^2\exp\left(-\frac{\rho^2}{2c_0}\left(1+\frac{1}{{\omega_{01}}^2\nu^2}\left(\dot{\phi}-\omega_{01}\kappa\right)^2\right)\right)d\rho$$

Next variable transformation,

$$\xi = \frac{\rho^2}{2c_0}\left(1+\frac{1}{{\omega_{01}}^2\nu^2}\left(\dot{\phi}-\omega_m\kappa\right)^2\right) \quad \rightarrow \quad \rho = \sqrt{2c_0}\left(1+\frac{1}{{\omega_{01}}^2\nu^2}\left(\dot{\phi}-\omega_{01}\kappa\right)^2\right)^{-\frac{1}{2}}\xi^{\frac{1}{2}}$$

$$d\xi = \frac{\rho}{c_0}\left(1+\frac{1}{{\omega_{01}}^2\nu^2}\left(\dot{\phi}-\omega_{01}\kappa\right)^2\right)d\rho \quad \rightarrow \quad \rho d\rho = c_0\left(1+\frac{1}{{\omega_{01}}^2\nu^2}\left(\dot{\phi}-\omega_{01}\kappa\right)^2\right)^{-1}d\xi$$

After substituting transformed variables,

$$f(\dot{\phi}) = \frac{1}{\sqrt{2\pi c_0^3 {\omega_{01}}^2\nu^2}}\int_0^\infty \sqrt{2c_0}\left(1+\frac{1}{{\omega_{01}}^2\nu^2}\left(\dot{\phi}-\omega_{01}\kappa\right)^2\right)^{-\frac{1}{2}}\xi^{\frac{1}{2}}\exp(-\xi)\, c_0\Bigg(1$$

$$+\frac{1}{{\omega_{01}}^2\nu^2}\left(\dot{\phi}-\omega_{01}\kappa\right)^2\Bigg)^{-1}d\xi$$

$$= \frac{1}{\sqrt{\pi{\omega_{01}}^2\nu^2}}\left(1+\frac{1}{{\omega_{01}}^2\nu^2}\left(\dot{\phi}-\omega_{01}\kappa\right)^2\right)^{-\frac{3}{2}}\int_0^\infty \xi^{\frac{1}{2}}\exp(-\xi)\, d\xi$$

$$= \frac{1}{\sqrt{\pi{\omega_{01}}^2\nu^2}}\left(1+\frac{1}{{\omega_{01}}^2\nu^2}\left(\dot{\phi}-\omega_{01}\kappa\right)^2\right)^{-\frac{3}{2}}\frac{\sqrt{\pi}}{2}$$

$$= \frac{1}{2\omega_{01}\nu}\left(1 + \frac{1}{{\omega_{01}}^2\nu^2}\left(\dot{\phi} - \omega_{01}\kappa\right)^2\right)^{-\frac{3}{2}} \tag{5.63}$$

Note that the calculation of the integral requires

$$\int_0^\infty t^{\frac{1}{2}} \exp(-t)\, dt = \int_0^\infty t^{\frac{3}{2}-1} \exp(-t)\, dt = \Gamma\left(\frac{3}{2}\right) = \frac{\sqrt{\pi}}{2}$$

We used the following relationship to improve the perspective of the equation.

$$z = \frac{1}{\omega_{01}\nu}\left(\dot{\phi} - \omega_{01}\kappa\right)$$

Putting together the variables as

$$f(z) = f(\dot{\phi})\left|\frac{\partial\dot{\phi}}{\partial z}\right| = \frac{1}{2\omega_{01}\nu}(1 + z^2)^{-\frac{3}{2}}\frac{1}{\omega_{01}\nu} = \frac{1}{2{\omega_{01}}^2\nu^2}(1 + z^2)^{-\frac{3}{2}} \tag{5.64}$$

This is a Bell-shaped distribution.

If we apply the variable transformation of equation (5.58) to equation (5.63), we get

$$f(\eta) = \frac{1}{2\omega_{01}\nu}\left(1 + \frac{1}{{\omega_{01}}^2\nu^2}\left(\left(\frac{1}{\eta} - \frac{\omega_c}{\omega_{01}}\right)\omega_{01} - \omega_{01}\kappa\right)^2\right)^{-\frac{3}{2}}\frac{\omega_{01}}{\eta^2}$$

$$= \frac{1}{2\nu\eta^2}\left(1 + \frac{1}{\nu^2}\left(\left(\frac{1}{\eta} - \frac{\omega_c}{\omega_{01}}\right) - \kappa\right)^2\right)^{-\frac{3}{2}}$$

$$f(\eta) = \frac{1}{2\nu\eta^2}\left(1 + \frac{1}{\nu^2}\left(\frac{1}{\eta} - 1\right)^2\right)^{-\frac{3}{2}} \tag{5.65}$$

5.6 Modified Longuet-Higgins model

5.6.1 Modification of wave period range

The domain of the probability density function is

$$0 \le \zeta < \infty\,, -\infty < \eta < \infty$$

However, since η represents the period, it should be defined only to positive values. In fact, when $\eta < 0$, $f(\zeta, \eta) \sim 0$, so the range of η is forced to

$$0 \le \eta < \infty$$

Therefore, the derived density function also has value in the negative region, but its magnitude is not significant due to the narrowband nature of the wave assumption. Therefore, in order to delete this area and maintain the normality of the density function (the integral value of the entire area is 1), the coefficients is added as L.

The density function before adding the coefficients is:

$$f(\zeta,\eta)=\frac{1}{8\sqrt{2\pi}\,\nu}\left(\frac{\zeta}{\eta}\right)^{2}\exp\left(-\frac{\zeta^{2}}{8}\right)\exp\left(-\frac{\zeta^{2}}{8\nu^{2}}\left(\frac{1}{\eta}-1\right)^{2}\right)$$

Moreover, $H_{1/3}/4$, it is inconvenient from an engineering point of view to make the wave height dimensionless. Therefore, $H_{1/3}$ as a non-dimensionalization by

$$\zeta=\frac{H}{H_{1/3}}=\frac{\zeta_{\mathrm{original}}}{4}$$

is newly defined and rewritten as follows by variable conversion .

$$f(\zeta,\eta)=f(\zeta_{\mathrm{original}},\eta)\left|\frac{d\zeta_{\mathrm{original}}}{d\zeta}\right|=4\times f(\zeta_{\mathrm{original}},\eta)$$

$$=\frac{8}{\sqrt{2\pi}\,\nu}\left(\frac{\zeta}{\eta}\right)^{2}\exp(-2\zeta^{2})\exp\left(-2\frac{\zeta^{2}}{\nu^{2}}\left(\frac{1}{\eta}-1\right)^{2}\right)$$

and the normalization factor for it as "L"

$$f(\zeta,\eta)=\frac{8\boldsymbol{L}}{\sqrt{2\pi}\,\nu}\left(\frac{\zeta}{\eta}\right)^{2}\exp(-2\zeta^{2})\exp\left(-2\frac{\zeta^{2}}{\nu^{2}}\left(\frac{1}{\eta}-1\right)^{2}\right)\tag{5.66}$$

$$0\le\zeta<\infty,\qquad 0\le\eta<\infty$$

At this time, from the condition of the probability density function is represented as

$$\int_{0}^{\infty}\int_{0}^{\infty}f(\zeta,\eta)\,d\zeta d\eta=1$$

Must. If we substitute the density function and compute this integral

$$\int_{0}^{\infty}\int_{0}^{\infty}f(\zeta,\eta)\,d\zeta d\eta=\int_{0}^{\infty}\int_{0}^{\infty}\frac{8L}{\sqrt{2\pi}\,\nu}\left(\frac{\zeta}{\eta}\right)^{2}\exp(-2\zeta^{2})\exp\left(-2\frac{\zeta^{2}}{\nu^{2}}\left(\frac{1}{\eta}-1\right)^{2}\right)d\zeta d\eta$$

$$= \int_0^\infty \frac{8L}{\sqrt{2\pi}\,\nu}\frac{1}{\eta^2}\int_0^\infty \zeta^2 \exp\left(-2\zeta^2\left(1+\frac{1}{\nu^2}\left(\frac{1}{\eta}-1\right)^2\right)\right) d\zeta d\eta$$

Substitute as A,

$$A = 1+\frac{1}{\nu^2}\left(\frac{1}{\eta}-1\right)^2$$

$$= \int_0^\infty \frac{8L}{\sqrt{2\pi}\,\nu}\frac{1}{\eta^2}\int_0^\infty \zeta^2 \exp(-2\zeta^2 A)\, d\zeta d\eta$$

Variable substitution,

$$\xi = 2\zeta^2 A \quad \rightarrow \quad d\xi = 4\zeta A d\zeta,\ \ \zeta = \sqrt{\frac{\xi}{2A}}$$

$$= \int_0^\infty \frac{8L}{\sqrt{2\pi}\,\nu}\frac{1}{\eta^2}\int_0^\infty \sqrt{\frac{\xi}{2A}} \exp(-\xi)\frac{1}{4A}\ d\xi\, d\eta$$

$$= \int_0^\infty \frac{L}{\sqrt{\pi}\,\nu}\frac{1}{\eta^2}A^{-\frac{3}{2}}\int_0^\infty \sqrt{\xi} \exp(-\xi)\ d\xi\, d\eta$$

Note that the calculation of the integral requires variable Transformation ,

So, after multiple variable transformation, we get

$$\frac{L}{2}\left(1+\sqrt{\frac{1}{\nu^2+1}}\right) = 1$$

so that L is determined as follows,

$$L = 2\left(1+\sqrt{\frac{1}{\nu^2+1}}\right)^{-1}$$

Note that Longuet-Higgins (1983)[31] approximated L under a dimensionless quantity of $\zeta = 4H/H_{1/3}$ as follows (the dimensionless quantity in this thesis is $\zeta = H/H_{1/3}$).

$$L = 1+\frac{\nu^2}{4} \tag{5.67}$$

Equation (5.66) is illustrated in Fig. 5.3 and Fig. 5.4, respectively

$$f(\zeta,\eta) = \frac{8}{\sqrt{2\pi}}\frac{L}{\nu}\left(\frac{\zeta}{\eta}\right)^2 \exp(-2\zeta^2)\exp\left\{-\frac{2\zeta^2}{\nu^2}\left(\frac{1}{\eta}-1\right)^2\right\} \tag{5.68}$$

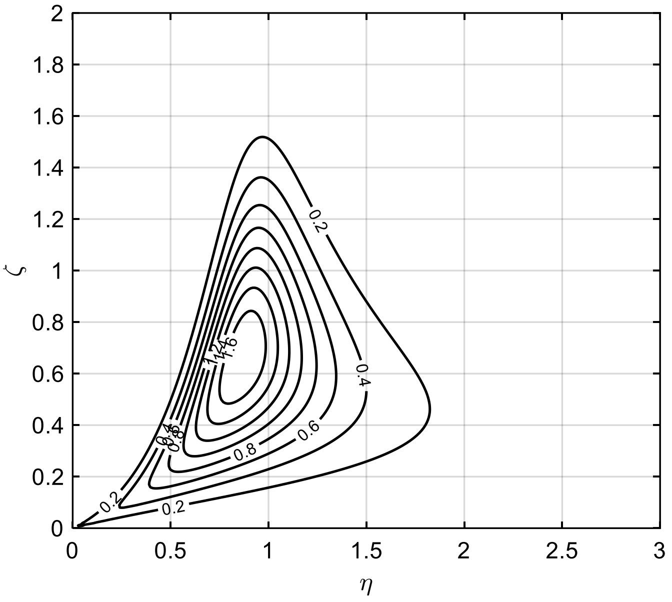

FIGURE 5.3: Joint probability density function of wave height and wave period of JONSWAP spectrum with the band width parameter $\nu = 0.39$.

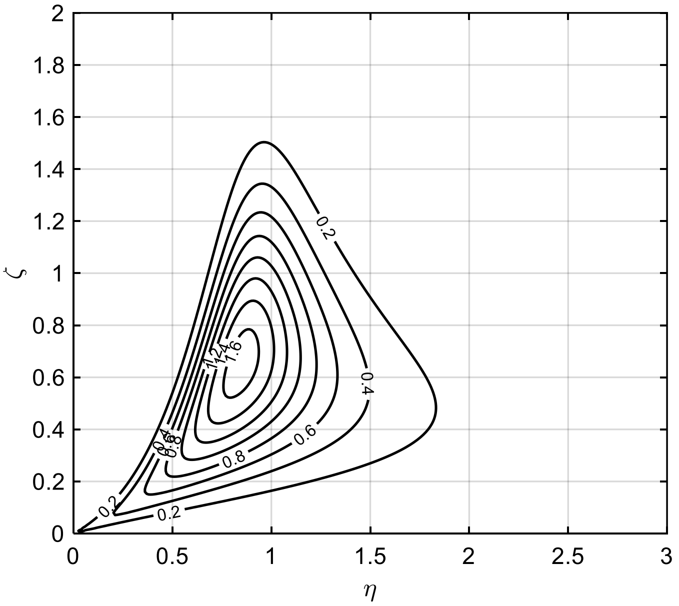

FIGURE 5.4: Joint probability density function of wave height and wave period of ITTC spectrum with the band width parameter $\nu = 0.42$

5.6.2 Improved Longuet -Higgins model by correction of the peak period

Until now, the Longuet-Higgins (1983) [31] joint distribution is still a widely accepted theoretical model in describing the distribution of wave height and associated period in a single wave system (Zhang *et al*., 2013b)[56]. Based on the linear assumption, Longuet-Higgins expressed the displacement of ocean waves in short-term sea conditions as a modulated model of carrier waves (regular waves) that fluctuate stochastically with the mean wave period of the irregular ocean waves. Furthermore, the modulation component is associated with the wave spectrum which follows a Gaussian distribution, showing the joint probability density function of the wave height and wave period of the short-term sea conditions.

There is a superposition method as a time-series simulation method for wave displacement with an arbitrary wave spectrum. A probability density function obtained from this time series by normalizing the zero-up-cross period and the frequency of simultaneous occurrence of wave heights in that period is called a simulation model. However, as shown in Fig. 5.5, comparison of this joint probability density function with the distribution of wave heights and wave periods obtained by numerical simulations of waves the (simulation model) under linear assumptions from the given wave spectrum shows a discrepancy in the peak of the distribution.

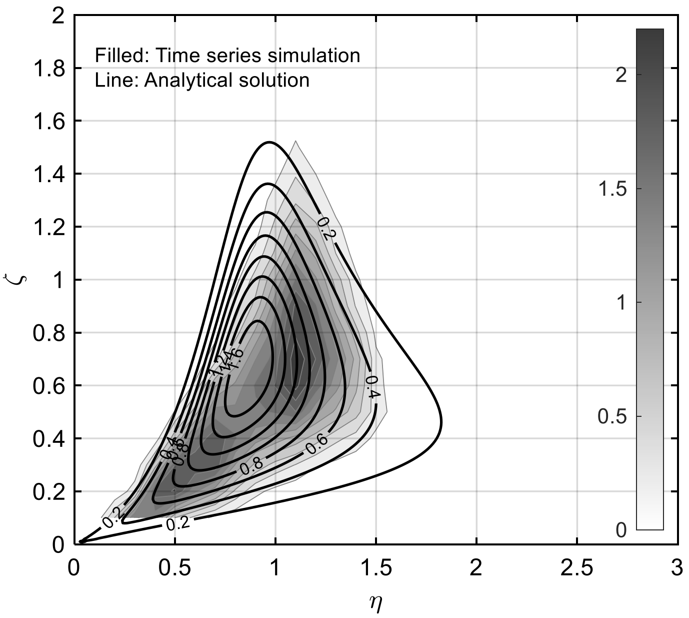

FIGURE 5.5: Comparison of joint probability density functions of wave height and wave period. Filled contour is that obtained from the time series simulation of JONSWAP spectrum. Line contour from the Original Longuet-Higgins model.

A comparison between the Longuet -Higgins model and the simulation model is shown in Fig. 5.5 . The JONSWAP spectrum was used as the wave spectrum. There is a discrepancy between the two models in terms of the peak period (mode period). The reason for this may be that the Longuet -Higgins model assumes a narrow band $\nu \ll 1$, but the JONSWAP spectrum $\nu \sim 0.4$, which does not fully satisfy the assumed conditions. Therefore, the instantaneous wave frequency of the carrier used in the derivation of the Longuet -Higgins model is

$$\Omega = \dot{\phi}(t) + \omega_c \tag{5.69}$$

is shifted from the zero up-crossing wave frequency, and the peak period (mode period) cannot be represented correctly. Based on this fact, the correction of the peak period is considered.

Regarding this, Zhang and Guedes Soares (2016)[55] also showed that if the period of the carrier wave is replaced from the mean wave period to the peak period of the wave spectrum, the discrepancy of the peak of the probability distribution can be improved. From an engineering point of view, the joint probability density function shown by Zhang et al. would be useful. So, One alternative method is to use the peak frequency as the carrier wave frequency directly for each wave system.

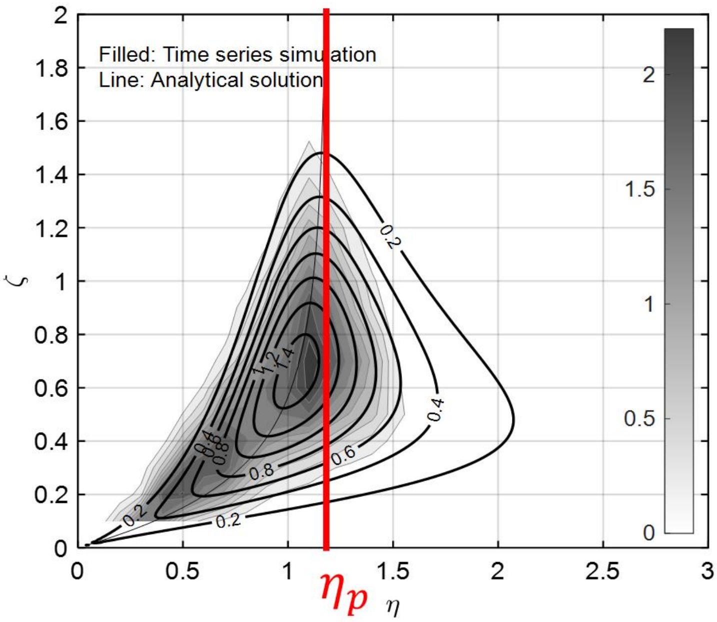

FIGURE 5.6: Comparison of joint probability density functions of wave height and wave period. Filled contour is that obtained from the time series simulation of JONSWAP spectrum. Line contour from the Modified Longuet-Higgins model by peak period.

It can be seen in Fig. 5.6 that the ridgeline (Appendix A) of the simulation model extends smoothly from $(\zeta,\eta)=(0,0)$ to the peak period position, and then extends upward (in the direction of the large ζ) at a steep angle from the peak period position. It would be reasonable to assume that the asymptotic value is the peak period of the wave spectrum. To achieve this, the instantaneous wave frequency of the carrier that is Eq. 5.69 is multiplied by an appropriate factor α, Correction is done as follows .

$$\Omega=\alpha\left(\dot{\phi}(t)+\omega_c\right) \tag{5.70}$$

This α is obtained from the condition that the ridgeline of the probability density function asymptotically approaches the peak period of the wave spectrum. By modifying equation (5.70), the dimensionless and related variables for frequency are redefined as follows.

$$\eta=\frac{T}{T_{01}}=\frac{\omega_{01}}{\Omega}=\frac{\omega_{01}}{\alpha\left(\dot{\phi}(t)+\omega_c\right)} \tag{5.71}$$

$$\dot{\phi}(t)=\left(\frac{1}{\alpha\eta(t)}-\frac{\omega_c}{\omega_{01}}\right)\omega_{01} \tag{5.72}$$

$$\frac{\partial\left(\rho,\dot{\phi}\right)}{\partial(\zeta,\eta)}=\det\begin{bmatrix}\frac{\partial\rho}{\partial\zeta} & \frac{\partial\rho}{\partial\eta}\\ \frac{\partial\dot{\phi}}{\partial\zeta} & \frac{\partial\dot{\phi}}{\partial\eta}\end{bmatrix}=\det\begin{bmatrix}2\sqrt{c_0} & 0\\ 0 & -\frac{\omega_{01}}{\alpha\eta^2}\end{bmatrix}=\frac{2\sqrt{c_0}}{\alpha\eta^2}\omega_{01} \tag{5.73}$$

Restating the probability density function (5.56) equation for $\left(\rho,\dot{\phi}\right)$

$$f\left(\rho,\dot{\phi}\right)=\frac{\rho^2}{\sqrt{2\pi c_0^3{\omega_{01}}^2\nu^2}}\exp\left(-\frac{\rho^2}{2c_0}\right)\exp\left(-\frac{\rho^2}{2c_0{\omega_{01}}^2\nu^2}\left(\dot{\phi}-\omega_{01}\kappa\right)^2\right)$$

Then, a new probability density function is obtained by a variable transformation on the redefined variables as follows,

$$f(\zeta,\eta)=f\left(\rho,\dot{\phi}\right)\frac{\partial\left(\rho,\dot{\phi}\right)}{\partial(\zeta,\eta)}$$

$$=\frac{\rho^2}{\sqrt{2\pi c_0^3{\omega_{01}}^2\nu^2}}\exp\left(-\frac{\rho^2}{2c_0}\right)\exp\left(-\frac{\rho^2}{2c_0{\omega_{01}}^2\nu^2}\left(\dot{\phi}-\omega_m\kappa\right)^2\right)\frac{2\sqrt{c_0}}{\alpha\eta^2}\omega_{01}$$

$$=\frac{\left(2\sqrt{c_0}\zeta\right)^2}{\sqrt{2\pi c_0^3{\omega_{01}}^2\nu^2}}\exp\left(-\frac{\left(2\sqrt{c_0}\zeta\right)^2}{2c_0}\right)\exp\left(-\frac{\left(2\sqrt{c_0}\zeta\right)^2}{2c_0{\omega_{01}}^2\nu^2}\left(\left(\frac{1}{\alpha\eta}-\frac{\omega_c}{\omega_{01}}\right)\omega_{01}\ -\omega_{01}\kappa\right)^2\right)\frac{2\sqrt{c_0}}{\alpha\eta^2}\omega_m$$

$$= \frac{8}{\alpha\sqrt{2\pi\nu^2}}\left(\frac{\zeta}{\eta}\right)^2 \exp(-2\zeta^2)\exp\left(-2\frac{\zeta^2}{\nu^2}\left(\left(\frac{1}{\alpha\eta}-1+\kappa\right)-\kappa\right)^2\right)$$

$$f(\zeta,\eta) = \frac{8}{\alpha\sqrt{2\pi}\,\nu}\left(\frac{\zeta}{\eta}\right)^2 \exp(-2\zeta^2)\exp\left(-2\frac{\zeta^2}{\nu^2}\left(\frac{1}{\alpha\eta}-1\right)^2\right)$$

the normalization factor for it as "L_c"

$$\boldsymbol{f(\zeta\,,\eta) = \frac{8L_c}{\alpha\sqrt{2\pi}\,\nu}\left(\frac{\zeta}{\eta}\right)^2 \exp(-2\zeta^2)\exp\left\{-\frac{2\zeta^2}{\nu^2}\left(1-\frac{1}{\alpha\eta}\right)^2\right\}} \qquad \mathbf{(5.74)}$$

where,

$$L_c = 2\left(1+\frac{1}{\sqrt{\nu^2+1}}\right)^{-1}, \qquad \alpha = \frac{1}{\eta_p} = \frac{\omega_p}{\omega_{01}}$$

ω_p is the peak frequency of the wave spectrum and ω_{01} the mean wave frequency defined as $\omega_{01} = m_1/m_0$.

The ridge of this density function is obtained by tracking the location of 0 slope with respect to η. The ridge line is defined as follows,

$$\frac{df(\zeta,\eta)}{d\eta} = 0 \qquad (5.75)$$

is a curve that satisfies the differentiated equation (5.74) with respect to η,

$$\frac{df(\zeta,\eta)}{d\eta} = f(\zeta,\eta)\left(-\frac{2}{\eta}-4\frac{\zeta^2}{\nu^2}\left(\frac{1}{\alpha\eta}-1\right)\left(\frac{-1}{\alpha\eta^2}\right)\right)$$

$$= f(\zeta,\eta)\frac{2}{\eta^3}\left(-\eta^2+2\frac{\zeta^2}{\alpha^2\nu^2}(1-\alpha\eta)\right) \qquad (5.76)$$

Therefore, by substituting it in equation (5.75),

$$-\eta^2+2\frac{\zeta^2}{\alpha^2\nu^2}(1-\alpha\eta) = 0$$

is obtained, This is transformed into the following equation .

$$-\frac{\alpha^2\nu^2}{2\zeta^2}\eta^2+(1-\alpha\eta) = 0$$

In the limit of , if we asymptotically approach the peak period of the wave spectrum , then

At the limit of $\zeta \to \infty$, if the peak period of the wave spectrum is asymptotic, then $\eta_p = \omega_{01}/\omega_p$

$$-\frac{\alpha^2\nu^2}{2\infty^2}\eta_p^2+\left(1-\alpha\eta_p\right) = 0$$

Hence, α is determined as follows,

$$\alpha = \frac{1}{\eta_p} = \frac{\omega_p}{\omega_{01}} \tag{5.77}$$

The equation for drawing the ridge line in this case is

$$\zeta = \frac{\nu\alpha\eta}{2\sqrt{1-\alpha\eta}} \tag{5.78}$$

or the following equation,

$$\eta = \frac{\zeta^2}{\alpha\nu^2}\left(-1 + \sqrt{1 + \frac{2\nu^2}{\zeta^2}}\right) \tag{5.79}$$

The probability density function of Equation (5.74) is shown in Fig. 5.7. The peak period is closer to that of the simulation model, indicating that the model has been improved. However, the spread of the distribution in the region of $\eta > \eta_p$ is larger than that of the simulation model. This improvement is presented in the next section.

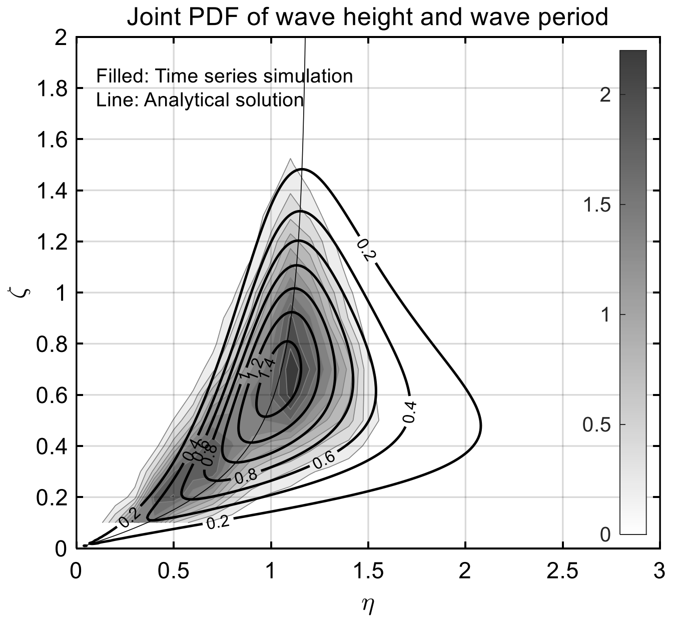

FIGURE 5.7: Comparison of joint probability density functions of wave height and wave period. Filled contour is that obtained from time series simulation of JONSWAP spectrum. Line contour is from the improved modified Longuet-Higgins model replaced with peak period.

5.6.3 Improved Longuet -Higgins model by correction of the peak period and distribution spread

Table 5.1 shows the ratio of the mean wave period (zero-up crossing wave period) calculated from the wave spectrum and the probability density function . The mean period due to the wave spectrum is given by using the spectral moment

$$\eta_{02} = \frac{T_{02}}{T_{01}} = \frac{\omega_{01}}{\omega_{02}} = \frac{m_1/m_0}{\sqrt{m_2/m_0}} = \frac{m_1}{\sqrt{m_0 m_2}}$$

and the mean wave period by the probability density function was obtained by the following equation.

$$\eta_m = \int_0^\infty \int_0^\infty \eta f(\zeta,\eta) d\zeta d\eta$$

TABLE 5.1: mean wave period by the pdf function calculation

Model	η_m	η_{02}	η_m/η_{02}
Original Longuet -Higgins	1.1608	0.9316	1.2460
Modified by Peak Period	1.4156	0.9316	1.5195

Table 5.1 shows these ratios η_m/η_{02}: η_m and η_{02} is a quantity that should match, but the result is greater than 1, indicating that η_m is shifted to the longer period compared to η_{02}. This discrepancy is due to the spread of the modified Longuet -Higgins model distribution in the region of $\eta > \eta_p$, which is larger than that of the simulation model. The spread of the distribution with respect to η depends on ν^2 what is included in the argument of the exponential function in equation (5.68) . The smaller the ν^2 , the smaller the spread of the distribution. Therefore, in the region where $\eta > \eta_p$, the spread of the distribution is suppressed by multiplying ν^2 by a coefficient β. That is, it is as follows.

$$\boldsymbol{f(\zeta,\eta)} = \frac{\boldsymbol{8L_p}}{\boldsymbol{\alpha\sqrt{2\pi}\,\nu}}\left(\frac{\boldsymbol{\zeta}}{\boldsymbol{\eta}}\right)^{\boldsymbol{2}} \mathbf{exp}\left(-\boldsymbol{2\zeta^2}\right) \mathbf{exp}\left(-\boldsymbol{2}\frac{\boldsymbol{\zeta^2}}{\boldsymbol{\beta\nu^2}}\left(\frac{\boldsymbol{1}}{\boldsymbol{\alpha\eta}} - \boldsymbol{1}\right)^{\boldsymbol{2}}\right) \tag{5.80}$$

$$\beta = \begin{cases} 1, & \eta \le \eta_p \\ \gamma, & \eta > \eta_p \end{cases}$$

where L_p is the normalization factor and

$$\int_0^\infty \int_0^\infty f(\zeta,\eta)d\zeta d\eta = 1 \tag{5.81}$$

is determined so as to satisfy the following equation. In addition, $\eta = \eta_p$

$$f(\zeta,\eta_p) = \frac{8L_p}{\alpha\sqrt{2\pi}\,\nu}\left(\frac{\zeta}{\eta}\right)^2 \exp(-2\zeta^2)$$

and is independent of β.Therefore, even if L_p is constant, it is continuous in the vicinity of $f(\zeta,\eta_p)$. However, it should be noted that it is not smooth. The following calculations are performed to obtain the normalization factor L_p.

$$\int_0^\infty \int_0^\infty f(\zeta,\eta)\, d\zeta d\eta = \int_0^\infty f(\eta) d\eta$$

$$= \int_0^\infty \frac{L_p}{2\alpha\nu\eta^2}\left(1+\frac{1}{\beta\nu^2}\left(\frac{1}{\alpha\eta}-1\right)^2\right)^{-\frac{3}{2}} d\eta$$

$$= \frac{L_p}{2\alpha\nu}\int_0^\infty \frac{1}{\eta^2}\left(1+\frac{1}{\beta\nu^2}\left(\frac{1}{\alpha\eta}-1\right)^2\right)^{-\frac{3}{2}} d\eta$$

Using variable transformation,

$$\xi = \left(1+\frac{1}{\beta\nu^2}\left(\frac{1}{\alpha\eta}-1\right)^2\right)^{-\frac{1}{2}}$$

$$= \quad \rightarrow \quad d\xi = -\frac{1}{2}\left(1+\frac{1}{\beta\nu^2}\left(\frac{1}{\alpha\eta}-1\right)^2\right)^{-\frac{3}{2}} \frac{2}{\beta\nu^2}\left(\frac{1}{\alpha\eta}-1\right)\frac{-1}{\alpha\eta^2} d\eta$$

$$= \quad \rightarrow \quad d\xi = \frac{1}{\alpha\eta^2}\left(1+\frac{1}{\beta\nu^2}\left(\frac{1}{\alpha\eta}-1\right)^2\right)^{-\frac{3}{2}} \frac{1}{\beta\nu^2}\left(\frac{1}{\alpha\eta}-1\right) d\eta$$

$$= \quad \rightarrow \quad \alpha\beta\nu^2\left(\frac{1}{\alpha\eta}-1\right)^{-1} d\xi = \frac{1}{\eta^2}\left(1+\frac{1}{\beta\nu^2}\left(\frac{1}{\alpha\eta}-1\right)^2\right)^{-\frac{3}{2}} d\eta$$

$$= \frac{L_p}{2\alpha\nu}\int_0^\infty \alpha\beta\nu^2\left(\frac{1}{\alpha\eta}-1\right)^{-1} d\xi$$

$$= \frac{\nu L_p}{2}\int_0^\infty \beta\left(\frac{1}{\alpha\eta}-1\right)^{-1} d\xi$$

Using variable transformation,

$$\xi = \left(1 + \frac{1}{\beta\nu^2}\left(\frac{1}{\alpha\eta} - 1\right)^2\right)^{-\frac{1}{2}}$$

$$= \quad \rightarrow \quad \frac{1}{\alpha\eta} - 1 = \begin{cases} \sqrt{\beta}\nu\sqrt{\xi^{-2} - 1}, & 0 \le \eta \le \frac{1}{\alpha} \rightarrow \; 0 \le \xi \le 1 \\ -\sqrt{\beta}\nu\sqrt{\xi^{-2} - 1}, & \frac{1}{\alpha} \le \eta \le \infty \; \rightarrow \; 1 \le \xi \le \left(1 + \frac{1}{\beta\nu^2}\right)^{-\frac{1}{2}} \end{cases}$$

$$= \frac{\nu L_p}{2}\left(\int_0^1 \frac{\beta}{\sqrt{\beta}\nu\sqrt{\xi^{-2} - 1}} d\xi + \int_1^{\left(1+\frac{1}{\beta\nu^2}\right)^{-\frac{1}{2}}} \frac{-\beta}{\sqrt{\beta}\nu\sqrt{\xi^{-2} - 1}} d\xi\right)$$

$$= \frac{\nu L_p}{2}\left(\int_0^1 \frac{1}{\nu\sqrt{\xi^{-2} - 1}} d\xi + \int_1^{\left(1+\frac{1}{\gamma\nu^2}\right)^{-\frac{1}{2}}} \frac{-\gamma}{\sqrt{\gamma}\nu\sqrt{\xi^{-2} - 1}} d\xi\right)$$

$$= \frac{L_p}{2}\left(\int_0^1 \frac{\xi}{\sqrt{1 - \xi^2}} d\xi + \sqrt{\gamma}\int_1^{\left(1+\frac{1}{\gamma\nu^2}\right)^{-\frac{1}{2}}} \frac{-\xi}{\sqrt{1 - \xi^2}} d\xi\right)$$

Using variable transformation,

$$t = 1 - \xi^2 \rightarrow \; dt = -2\xi d\xi$$

$$= \frac{L_p}{2}\left(\int_1^0 \frac{-1}{2\sqrt{t}} dt + \sqrt{\gamma}\int_0^{1-\left(1+\frac{1}{\gamma\nu^2}\right)^{-1}} \frac{1}{2\sqrt{t}} dt\right)$$

$$= \frac{L_p}{4}\left(-\left[2\sqrt{t}\right]_1^0 + \sqrt{\gamma}\left[2\sqrt{t}\right]_0^{1-\left(1+\frac{1}{\gamma\nu^2}\right)^{-1}}\right)$$

$$= \frac{L_p}{2}\left(1 + \sqrt{\gamma}\sqrt{1 - \left(1 + \frac{1}{\gamma\nu^2}\right)^{-1}}\right)$$

$$= \frac{L_p}{2}\left(1 + \sqrt{\frac{\gamma}{\gamma\nu^2 + 1}}\right)$$

So, from this result

$$\frac{L_p}{2}\left(1 + \sqrt{\frac{\gamma}{\gamma\nu^2 + 1}}\right) = 1$$

so that L_p is determined it is as follows.

$$\boldsymbol{L_p = 2\left(1 + \sqrt{\frac{\gamma}{\gamma\nu^2 + 1}}\right)^{-1}}$$

On the other hand, the mean wave period is obtained by numerical integration because an analytical solution cannot be found. γ is determined such that the mean wave period calculated from the probability density function corresponds to the mean wave period from the wave spectrum. Naturally, the Eq. 5.82 is satisfied.

$$\int_0^\infty \eta f(\zeta, \eta)\, d\eta = T_{01} \tag{5.82}$$

For the JONSWAP spectrum, $\gamma = 0.15$ is to be chosen from the numerical analysis.

Therefore, we additionally modify ν dominating the spread of distribution in $\eta > \eta_p$ as use of spectral width parameter depends critically on the tail behavior of the spectral density. Consequently, the joint probability density function of wave height and wave period is described as Eq. 5.80. This is shown in Fig. 5.8. Not only is the discrepancy of the distribution spreading being improved but also the peak position has also improved.

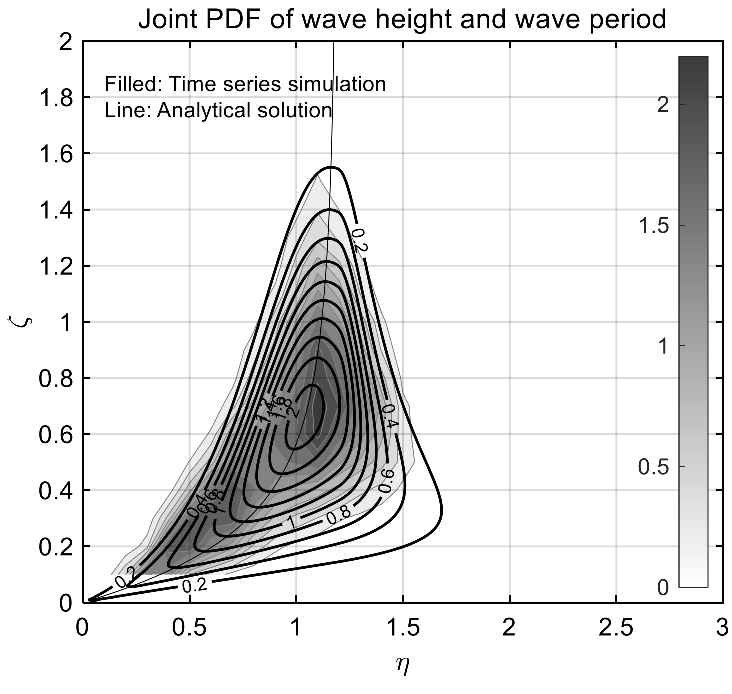

FIGURE 5.8: Comparison of joint probability density functions of wave height and wave period. Filled contour is that obtained from the time series simulation of JONSWAP spectrum. Line contour is from the modified Longuet-Higgins model replacing the carrier wave period to the spectrum peak period and reducing the spread of the tail.

5.7 Conclusion

In this chapter, mathematical formulation of joint probability density function for wave height and wave period based on Longuet-Higgins model was analytically derived and expressed the probability density functions applicable to wave height, wave period in a given random sea which represent the statistical characteristics of random waves. Then, the comparison with a time series simulated model with JONSWAP spectrum showed a discrepancy in the peak of the distribution and various improvements were introduced in the original Longuet-Higgins model. Modified versions of Longuet-Higgins joint distribution of wave heights and periods were proposed. Comparison was made with the simulation model for the given wave spectrum. Modification in the wave period range was performed. One of the improvements of asymptotic wave period (mean wave period) in the probability distribution to the wave spectrum peak period and other is the reduction in the width of the probability distribution spreading in the larger wave period range.

Chapter 6

Joint probability density function of wave height and ship response encountered by a ship moving forward in irregular seas

6.1 Introduction

This chapter describes the s the multivariate joint probability occurrence of a single wave encountered under stationary sea conditions and the ship's response to the wave. We determine the joint probability of the wave height encountered by the ship and the ship response expressed by a multivariate Rayleigh probability distribution. First, the relationship between the spectrum of waves and ship motion and their time series model is determined, and then the relationship between the time series model and the joint probability density function is determined. Furthermore, we determine the numerical solution by successive integration of the probability density function of wave carrier model and heave motion response. This proposed multivariate probability density function is further verified by the necessary numerical analysis The analysis is related to the superposition model for time-series generation of wave height and heave motion height. It is carried out according to the zero-up crossing definition to determine the occurrence frequency of the ship motion height in conjunction with the wave height. It is confirmed that the ship response motions are synchronized as the average wave period increased.

6.2 Theoretical background

Waves in the ocean can be assumed to be a linear and narrow-band phenomenon, and the probability distribution of wave heights is known to be the Rayleigh distribution. Since the motion response of a ship caused by such waves is also linear and narrow band, the probability distribution of the height difference of the motion response displacement (defined as "motion height") becomes the Rayleigh distribution. The characteristics of the probability distribution of motion height (Rayleigh distribution) are determined for each sea state, for example, the probability distribution of motion height can be obtained for each Beaufort scale, which is a criterion for the strength of the sea state, and the frequency of occurrence and probability of exceedance of motion height can be estimated. On the other hand, the motion response of a ship to a single wave is generally estimated by a deterministic mathematical models based on dynamical theory. This is because the ship's response in irregular waves is not caused by just one wave, but by the accumulation of previously experienced waves and responses. The ship response is determined by the memory effect of so-called dynamical phenomena. However, there are an infinite number of wave history patterns that a ship can encounter, and it is not possible to calculate the response history for all of them. Therefore, a probabilistic approach may be useful here as well. If the magnitude of the ship's response to a single wave can be presented probabilistically, the degree of freedom in the performance design of the ship can be expanded.

The probabilistic presentation of the magnitude of the hull response to a single wave is also useful in ship manoeuvring assistance. For example, it can reduce the burden on the ship operator by giving the judgement on whether or not a wave of a certain wave height approaching the ship can be safely survived (or without accumulating damage to the hull). In principle, the wave and hull motion can be predicted by a dynamic model, but this requires spatiotemporal waveform information around the hull. This is currently not possible. The stochastic approach, in other words, is to predict the magnitude of the hull response to a single wave by probabilistically assessing the uncertainties in the wave and response history. In this way, it is useful to know the motion response of a ship to a certain wave stochastically, but no such case has been seen so far. This method can be used in the estimation of hull response to a single wave, rather than estimation of hull response to sea conditions (significant wave height). It also helpful providing criteria for making manoeuvring decisions for a given wave. It will expand the flexibility in design and ship operation support by combining wave height and wave period. Hence, the probability of a ship moving forward in stationary irregular waves exceeding a certain value of motion or wave loading is useful in ship performance design. The threshold values of hull response to motion and wave loads are often evaluated against statistics of ocean phenomenon like significant wave height , mean wave period and Beaufort scale etc. However, these are not only the quantities that represent the characteristics of ocean phenomena such as wave spectrum, bandwidth, wave sequence (trains), correlation and simultaneity between wave height and wave period. If the threshold value and occurrence probability (or exceedance probability) of the hull response corresponding to these quantities are also evaluated, the degree and accuracy of performance design can be increased. Also, the smaller the time scale, the more it can be applied to navigation support. For example, the joint probability occurrence of waves (one wave or a series of wave) to be encountered and the hull response to them is useful for real-time ship manoeuvring decisions. In this paper, we discussed the joint probability of a single wave encountered under stationary sea conditions and the ship response at that wave.

Longuet-Higgins (1975, 1983)[30][31] assumed the linearity and narrowband nature of stationary irregular ocean waves, the joint probability occurrence of wave height and wave period for each wave was shown by him assuming that the wave components are normally distributed around the mean wave frequency as the carrier frequency. Recent studies done by Zhang and Guedes Soares[2016][55] have shown that it is better to use the peak frequency of the spectrum as the carrier frequency from an engineering point of view. The Longuet-Higgins's wave height-wave period probability distribution is a Rayleigh distribution when focusing only on the wave height. Since the hull motion in waves has a strong linearity with respect to wave height, the probability distribution of the hull motion is also a Rayleigh distribution. Therefore, when considering the simultaneity of wave height and hull response, the multivariate Rayleigh distribution is effective, Ochi et al.[57] showed the joint occurrence probability of waves and slamming. Umeda et al.[58] showed the probability of occurrence of broaching by combining the Longuet-Higgins's wave height -wave period distribution and a ship motion model.

6.3 Representation of encountering waves and ship motion by carrier wave modulation and statistics on autocorrelation

Time Series model of encountered waves and ship motions is shown in this section. Based on the linear assumption, Longuet-Higgins expressed the displacement of ocean waves in short-term sea conditions as a modulated model of carrier wave which is a regular wave with a period equal to mean wave period, and it's amplitude and phase are assumed to fluctuate stochastically and gradually around a certain value as derived in the Chapter 5. A clear explanation of this theory is mentioned in the textbook Ochi[37].

$$x(t) = \sum_{\mathrm{n}=1}^{\infty} a_{\mathrm{n}} \cos(\omega_{\mathrm{n}} t + \varepsilon_{\mathrm{n}}) = x_c(t) \cos\omega_m t - x_s(t) \sin\omega_m t \tag{6.1}$$

$$x_c(t) = \sum_{\mathrm{n}=1}^{\infty} a_{\mathrm{n}} \cos\{(\omega_{\mathrm{n}} - \omega_m)t + \varepsilon_{\mathrm{n}}\} \tag{6.2}$$

$$x_s(t) = \sum_{\mathrm{n}=1}^{\infty} a_{\mathrm{n}} \sin\{(\omega_{\mathrm{n}} - \omega_m)t + \varepsilon_{\mathrm{n}}\} \tag{6.3}$$

Where ω_m is the mean wave frequency and the two times of instantaneous amplitude obtained from $x_c(t)$ and $x_s(t)$ is the dashed line (envelope) of the Figure 5.1. The wave that the advancing ship encounters can be expressed by the following equation by replacing the wave frequency of this mathematical model with the encounter wave frequency.

$$y(t) = y_c(t)\cos\omega_{em}t - y_s(t)\sin\omega_{em}t \tag{6.4}$$

$$y_c(t) = \sum_{\mathrm{n}=1}^{\infty} a_{\mathrm{n}}\cos\{(\omega_{en} - \omega_{em})t + \varepsilon_{\mathrm{n}}\} \tag{6.5}$$

$$y_s(t) = \sum_{\mathrm{n}=1}^{\infty} a_{\mathrm{n}}\sin\{(\omega_{en} - \omega_{em})t + \varepsilon_{\mathrm{n}}\} \tag{6.6}$$

Where ω_e is the encounter wave frequency, ω_{en} is the discretized encounter wave frequency and ω_{em} is the mean wave frequency of the encounter wave. If the forward speed of the ship is V and the encounter angle between the ship and the wave is θ, the relationship between the wave frequency is as follows.

$$\omega_e = \omega - KV\cos\theta \tag{6.7}$$

K is the wave number at infinite depth, and the dispersion relation holds $\omega^2 = Kg$ and Note that θ = 0 [deg.] is the following wave and θ = 180 [deg.] is the head wave. On the other hand, the motion displacement of the advancing ship is given by the frequency response function of the motion to the wave i.e., $H(\omega) = H_a(\omega)e^{i\psi(\omega)}$. $H_{an}, \psi_{\mathrm{n}}$ is the response amplitude and phase lag expressed as real numbers, respectively where, $H_{an} = H_a(\omega_{\mathrm{n}}), \psi_{\mathrm{n}} = \psi(\omega_{\mathrm{n}})$.

$$z(t) = z_c(t)\cos\omega_{em}t - z_s(t)\sin\omega_{em}t \tag{6.8}$$

$$z_c(t) = \sum_{\mathrm{n}=1}^{\infty} H_{an}a_{\mathrm{n}}\cos\{(\omega_{en} - \omega_{em})t + \varepsilon_{\mathrm{n}} + \psi_n\} \tag{6.9}$$

$$z_s(t) = \sum_{\mathrm{n}=1}^{\infty} H_{an}a_{\mathrm{n}}\sin\{(\omega_{en} - \omega_{em})t + \varepsilon_{\mathrm{n}} + \psi_n\} \tag{6.10}$$

6.4 Probability of simultaneous occurrence of wave height and ship motion height.

First, the relationship between the spectrum of waves and hull motion and their time series model is determined, and then the relationship between the time series model and the co-occurrence probability density function is determined. By linking these results, the relationship between the spectrum of waves and hull motion and the probability density function of wave and ship motion is obtained. To find the relationship between wave height and ship motion height, the following vector variables are defined.

$$\boldsymbol{\xi} = [y_c, y_s, z_c, z_s]^T \tag{6.11}$$

If the variables y_c, y_s, z_c, z_s follow a multivariate normal distribution under the assumption of a narrowband phenomenon, the probability density function of $\boldsymbol{\xi}$ is expressed by the following equation.

$$f(\boldsymbol{\xi}) = \frac{1}{4\pi^2(|\boldsymbol{\Sigma}|)^{\frac{1}{2}}} \exp\left(-\frac{1}{2}\boldsymbol{\xi}^T\boldsymbol{\Sigma}^{-1}\boldsymbol{\xi}\right) \tag{6.12}$$

where is $\boldsymbol{\Sigma}$ the covariance matrix, which is as follows.

$$\boldsymbol{\Sigma} = \mathrm{Cov}[\boldsymbol{\xi}, \boldsymbol{\xi}] = \begin{bmatrix} c_0 & 0 & n_0^+ & -n_0^- \\ 0 & c_0 & n_0^- & n_0^+ \\ n_0^+ & n_0^- & d_0 & 0 \\ -n_0^- & n_0^+ & 0 & d_0 \end{bmatrix} \tag{6.13}$$

c_0, d_0 , n_0^+, n_0^- are spectral moments, and $S_{yy}(\omega_e)$ is the wave spectrum of the encounter wave, the $S_{zz}(\omega_e)$ is the ship motion spectrum, and if the $S_{yz}(\omega_e)$ is cross spectrum of the wave and the hull motion are defined as follows. The calculation formula is shown in the two-sided spectrum.

$$c_0 = m_{y0} = \int_{-\infty}^{\infty} S_{yy}(\omega_e)d\omega_e \tag{6.14}$$

$$d_0 = m_{z0} = \int_{-\infty}^{\infty} S_{zz}(\omega_e)d\omega_e \tag{6.15}$$

$$n_0^+ = \int_{-\infty}^{\infty} \mathrm{Re}\big[S_{yz}(\omega_e)\big]d\omega_e \tag{6.16}$$

$$n_0^- = \int_{-\infty}^{\infty} \mathrm{sgn}(\omega_e)\mathrm{Im}\big[S_{yz}(\omega_e)\big]d\omega_e \tag{6.17}$$

Here, the following variable transformation is performed.

$$y_c(t) = \rho_y(t)\cos\phi_y(t) \tag{6.18}$$

$$y_s(t) = \rho_y(t)\sin\phi_y(t) \tag{6.19}$$

$$z_c(t) = \rho_z(t)\cos\phi_z(t) \tag{6.20}$$

$$z_s(t) = \rho_z(t)\sin\phi_z(t) \tag{6.21}$$

Twice of ρ_y is the instantaneous wave height at that time i.e., $H_y = 2\rho_y(t)$ Using this, the instantaneous dimensionless wave height is defined by the following equation.

$$\zeta_y = \frac{H_y}{H_{1/3}} = \frac{H_y}{4(m_{y_0})^{\frac{1}{2}}} = \frac{\rho_y}{2(c_0)^{\frac{1}{2}}}, \quad 0 \le \zeta_y < \infty \tag{6.22}$$

$H_{1/3}$ is a significant wave height. Similarly, the instantaneous dimensionless hull motion height (the difference in height of the hull motion corresponding to the wave height) is defined as Eq. 6.22.

$$\zeta_z = \frac{H_z}{H_{1/3}} = \frac{H_z}{4\left(m_{y_0}\right)^{\frac{1}{2}}} = \frac{\rho_z}{2(c_0)^{\frac{1}{2}}}, \quad 0 \le \zeta_z < \infty \tag{6.23}$$

Using these relationships to transform y_c, y_s, z_c, z_s and into variables ζ_y, ζ_z, we obtained the following probability density function of simultaneous occurrence of wave height and ship motion height. Here, in order to improve the perspective, the expression of product of the occurrence probability density of the wave height and conditional occurrence probability density of the hull motion height conditioned on the wave height is given by Eq. 6.24.

$$f(\zeta_y, \zeta_z) = f(\zeta_y) f(\zeta_z|\zeta_y) \tag{6.24}$$

$f\left(\zeta_y\right)$, $f(\zeta_z|\zeta_y)$ is expressed as follows.

$$f(\zeta_y) = 4\zeta_y \exp\left(-2{\zeta_y}^2\right) \tag{6.25}$$

$$f\left(\zeta_z\middle|\zeta_y\right) = 4\rho\zeta_y I_0(z) \exp\left\{-2\rho\left(\left(\frac{d_0}{c_0} - \frac{1}{\rho}\right)\zeta_y^2 + \zeta_z^2\right)\right\} \tag{6.26}$$

$$z = 4\rho\zeta_y\zeta_z\left[\left(\frac{n_0^+}{c_0}\right)^2 + \left(\frac{n_0^-}{c_0}\right)^2\right]^{\frac{1}{2}} \tag{6.27}$$

$I_0(z)$ is the zeroth order Modified Bessel function of the first kind and ρ is defined as,

$$\rho = \frac{{c_0}^2}{c_0 d_0 - (n_0^+)^2 - (n_0^-)^2} \tag{6.28}$$

6.5 Numerical calculations

Figures 6.1 to 6.3 shows the calculation results of the occurrence probability density of the heave of a RIOS container vessel moving forward in a stationary long-crested irregular wave is shown in the contour diagram. The wave spectrum is the ITTC spectrum, and the waves are assumed to be head waves. The slope of the distribution is different from the mean wave period of 6 seconds, 10 seconds, and 18 seconds, and the slope of the ridge line converges to 1, and the spread of the distribution becomes narrow for longer periods. This is because the longer the mean wave period, the more the ship moves in sync with the waves. At the period of 18s in Figure 4, we can see that the ship is almost completely in tune with the waves. From this result, the validity of the calculation result can be seen.

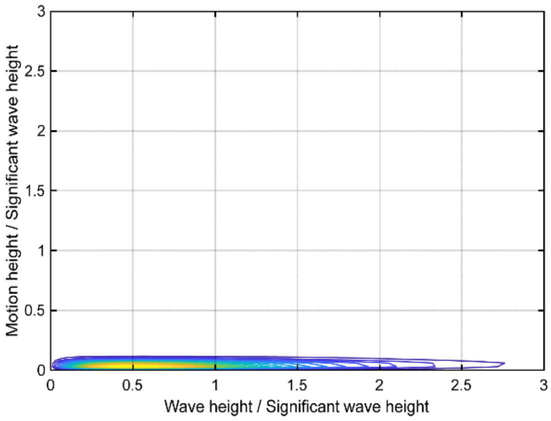

FIGURE 6.1. Joint probability density function of wave height and heave height of RIOS container ship advancing with $\mathrm{Fn} = 0.25$ in head wave of ITTC wave spectrum for $T_{01} = 6$s.

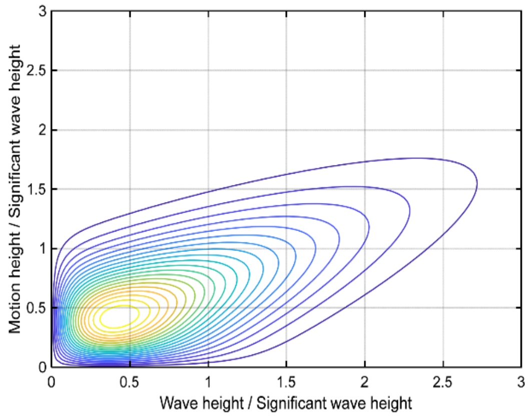

FIGURE 6.2. Joint probability density function of wave height and heave height of RIOS containership advancing with $\mathrm{Fn} = 0.25$ in head wave of ITTC wave spectrum for $T_{01} = 10$s.

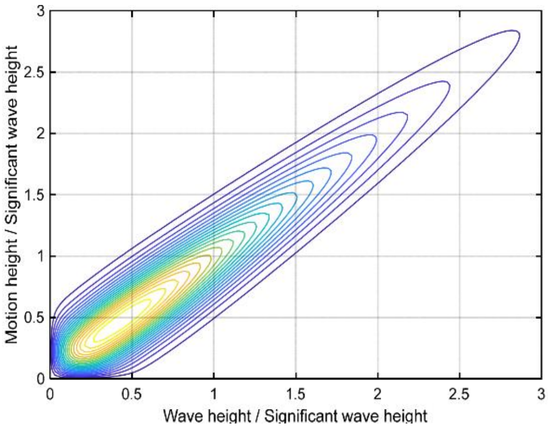

FIGURE 6.3. Joint probability density function of wave height and heave height of RIOS container ship advancing with $\mathrm{Fn} = 0.25$ in head wave of ITTC wave spectrum for $T_{01} = 18$s.

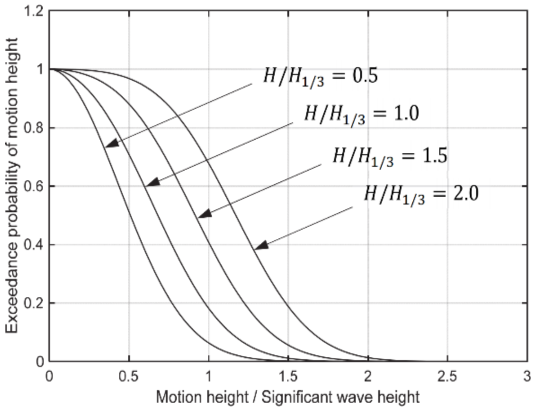

FIGURE 6.4. Exceedance probability of heave height of RIOS container ship advancing with $\mathrm{Fn} = 0.25$ in head wave of ITTC wave spectrum for $T_{01} = 10s$.

The proposed joint probability density function of wave height and ship motion height is further verified with the numerical analysis by comparing the time series of wave and heave motion based on zero-up crossing points. First, the heave motion response spectrum of RIOS containership was calculated based on the ITTC wave spectrum and heave response transfer function (RAO) which was obtained using linear potential based method. The generation of a time-series by superposition of wave components and ship motion height components was done, respectively. The necessary numerical analysis related to the superposition model for time-series generation of wave height and heave motion height was carried out according to the zero-up crossing definition to determine the frequency of the ship motion height occurring in conjunction with the wave height.

The data show the typical range of heave motion height of RIOS container ship advancing with Fn = 0.25 in head wave of ITTC wave spectrum for $T_{01} = 10$s for the various wave heights. To make the data comparable, results are presented as dimensionless quantities of wave height and ship motion height. The distributions of the ship motion height estimated by numerical analysis are almost equal to that of the results obtained using the joint probability density function of wave height and ship motion height. This confirms the validity of the probability density function of wave and ship motion.

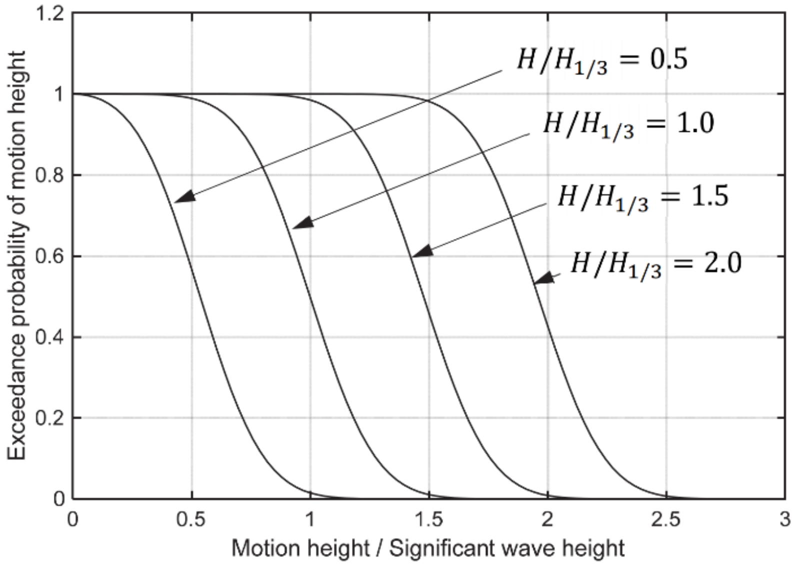

FIGURE 6.5. Exceedance probability of heave height of RIOS container ship advancing with Fn=0.25 in head wave of ITTC wave spectrum for $T_{01} = 18$s.

Figures 6.4 and 6.5 show the exceedance probability of heave oscillation when encountering a single wave. It is the exceedance probability obtained from the density function conditional on the wave height of the equation 6.24. The horizontal axis is the dimensionless quantity of the heave oscillation height (height difference), and the vertical axis is the exceedance probability. It is quantitatively shown that the exceedance probability increases as the wave height increases. For example, in Figure 6.4, when encountering a dimensionless wave height of 1.0, the probability that the non-dimensional heave oscillation height exceeds 1 is about 0.2. but when encountering a non-dimensional wave height of 1.5 , the probability is 0.4 and so on, the longer the average wave period, the steeper the rise of the probability, and synchronization with the wave can be confirmed from the Figure 6.5. It is important to note that this is not a short-term exceedance probability for a stationary sea state, but an exceedance probability when one wave is encountered.

6.6 Conclusion

The probability of simultaneous occurrence of wave height and wave period encountered by a ship moving forward at a constant speed in a stationary long crested irregular wave was determined according to the Longuet-Higgins method was extended to the probability of simultaneous occurrence of wave and hull motion. We theoretically calculated the joint probability density function of the wave height and ship motion height for a single wave encountered by a ship. The joint probability density function of the wave height and heave motion height encountered by the ship (expressed by a multivariate Rayleigh probability distribution) is calculated under the condition of forward speed, and it is illustrated graphically. The joint probability density function of the wave height and heave motion height was verified by the numerical analysis, and it is confirmed that the heave oscillations were synchronized as the average wave period increased, indicating the validity of this paper. The longer the mean wave period , the more the heave motions synchronized.

Chapter 7

Short-term prediction of added resistance by statistical model

7.1 Introduction

In this chapter, we have established a method for estimating the added resistance in irregular waves by combining the nonlinearity of added resistance due to wave height (or wave steepness) in regular waves with the encounter irregular wave statistics. The correction coefficients obtained in chapter 3 using CFD simulations with different ship models is incorporated into linear added wave resistance transfer function. Since the wave height and wave period are specified in the proposed PDF methods in chapter 5, it is possible to estimate short term predictions of added resistance including the wave height nonlinearity. Hence, these nonlinear effects of wave height and wave steepness are revealed by analyzing the added resistance in irregular waves. Its qualitative and quantitative characteristics are described in this section. Comparison of added resistance with the modified versions of Longuet-Higgins model is shown. Estimation of added resistance results with short term prediction methods with different ship models in head and oblique sea conditions are shown. Short term prediction of added resistance results by the improved Longuet-Higgin's model are verified by tank experiments and CFD results in long crested irregular waves. Summary of the results are concluded.

7.2 Theoretical background

The advantage of analyzing the ship response in waves in the time domain is that it can directly handle the transient response and non-linear response. This has an affinity for visualization of the interaction between wave and ship motion, and the result can be understood intuitively. However, when analyzing responses in stationary irregular waves, time-series data of sufficient length are required to eliminate the effects of uncertainty. On the other hand, the advantage of analysis in the frequency domain is the simplicity of using linear superposition. It can also be applied to nonlinear problems if the higher-order terms of frequency are considered. Darzell et al. (1974,1979)[2][3] conducted theoretical and experimental studies using the mathematical model up to the second order, and if the phenomenon satisfies Gaussian stationarity, the added resistance due to waves is estimated by Eq.7.1.

$$R_{AW}\left(H_{1/3}, T_{01}, V\right) = 2\int_0^{\infty} R_{WU}(\omega, V) S\left(\omega \middle| H_{1/3}, T_{01}\right) d\omega \tag{7.1}$$

where, $R_{WU}(\omega, V)$ is a linear response function that expresses the added resistance due to waves when traveling at a ship speed V in a head sea per unit wave amplitude of wave frequency ω. This formula is named the spectrum method (SPE). This added resistance is defined as the average of the secondary responses to wave displacement. $S\left(\omega \middle| H_{1/3}, T_{01}\right)$ represents the wave spectrum with significant wave height $H_{1/3}$ and mean wave period T_{01}. Kuroda et al. (2018)[22] showed the need for a fourth-order nonlinear fluid force because the nonlinearity with respect to the wave height of the wave added resistance is due to the bow shape above the waterline. As a result, a calculation result could explain an experimental result well. However, dealing with higher-order response functions and higher-order wave spectra departs from the convenience of linear superposition.

Hirayama et al. (1993)[9] showed experimentally that Hsu's assumptions (1970)[11] for the estimation of drifting force of floating bodies was applicable to the estimation of the added resistance of ships with forward speed in transient water waves and steady irregular waves. Hsu's assumption is that one wave of an irregular wave encountered is regarded as one cycle of a regular wave, and a drifting force with that as a half-cycle acts for each irregular wave. Based on this assumption, the time series of added resistance in waves was obtained, and the average was calculated. Hence, it agrees well with the calculation result by Eq. 7.1.

Basically, if we consider the irregular wave envelope as shown in Fig. 5.1 in Chapter 5, the time difference between the zero up crossing point of the wave displacement that appears immediately before the wave crest and the zero up crossing point that appears next to the wave trough is defined as zero up crossing wave period T, and the height between wave crest and next trough is defined as wave height H. According to Hsu's assumption it means that, in terms of probability statistics, if the probability density $p(H, T)$ of occurrence of each wave encountered by a ship and the response function $R_{WN}(H, T, V)$ of the added resistance for each wave are known, the added resistance in irregular waves can be estimated as

$$R_{AW}\left(H_{1/3}, T_{01}, V\right) = \int_0^{\infty}\int_0^{\infty} R_{WN}(H, T, V) p\left(H, T | H_{1/3}, T_{01}\right) dT dH \tag{7.2}$$

The function $R_{WN}(H,T,V)$ is a response function that considers the non-linearity with respect to the wave height. This formula is named the probability density function method (PDF) by Jawa, et al. (2022)[15].

It is possible to find $R_{WN}(H,T,V)$ using CFD or higher-order response function method, but it must be calculated for all required combinations of H,T,V. To avoid this, assume that the non-linear effect on the wave height can be separated from $R_{WN}(H,T,V)$ and each wave of irregular waves can be recognized as a cycle of the regular wave with wave amplitude $H/2$ and wave frequency $2\pi/T$,we express as Eq.7.3.

$$R_{WN}(H,T,V) = \left(\frac{H}{2}\right)^2 C(s)R_{WU}(2\pi/T,V) \tag{7.3}$$

where, $C(s)$ is a coefficient representing the non-linearity with respect to the wave steepness mentioned in Chapter 3 . The linear PDF method is defined for $C(s) = 1$. $R_{WU}(2\pi/T,V)$ is replaced with $R_{WU}(\omega,V)$ of a calculation result based on the linear potential theory. Then, $C(s)$ can be obtained numerically or experimentally from some of the representative points and the functional system of $C(s)$ can be fitted using them. At the representative point, $C(s)$ can be calculated by the following Eq. 7.4 transformed from Eq. 7.3.

$$C(s) = \frac{R_{WN}(H,T,V)}{H^2 R_{WU}(2\pi/T,V)} \tag{7.4}$$

This equation is essentially the same as Eq. 3.3 in chapter 3 . In this study, representative point of the $R_{WN}(H,T,V)$ and $R_{WU}(\omega,V)$ are numerically obtained by CFD, and $C(s)$ is determined. In this determination, the denominator of Eq. 7.4 should not be replaced with $R_{WU}(\omega,V)$ obtained from the linear potential-based calculation. This is because CFD can be qualitatively obtained with practical accuracy, but quantitatively it is not always so. Since $C(s)$ is a relative ratio of linearity and non-linearity, the base must be the same calculation method.

The function $R_{WU}(\omega,V)$ is calculated based on the Enhanced Unified Theory, which is the linear potential theory developed by Kashiwagi (1997, 2000)[33][34]. It estimates with reliable accuracy as results of research so far. Therefore, $R_{WN}(H,T,V)$ of Eq. 7.3 is formulated by $C(s)$ determined by CFD and $R_{WU}(\omega,V)$ determined by the linear potential-based calculation. This is a formulation that combines the qualitativeness of CFD and the quantitativeness of linear potential theory.

7.3 Comparison of short-term prediction calculation results

The probability density function method obtained by combining the joint occurrence probability density function of wave height and wave period in chapter 5 is used. Meaning, we obtain $p(H,T|H_{1/3},T_{01})$ with the variable transform of the probability density function of original and modified Longuet-Higgins models derived in Chapter 5 as shown in Eq. 7.5.

$$p(H,T|H_{1/3},T_{01}) = f(\zeta,\eta)\left|\frac{\partial(\zeta,\eta)}{\partial(H,T)}\right| \tag{7.5}$$

First, the joint occurrence probability density function of the wave height and wave period of a stationary irregular ocean waves based on the original Longuet-Higgins model defined by the following Eq. 7.6.

$$f(\zeta,\eta) = \frac{8}{\sqrt{2\pi}}\frac{L}{\nu}\left(\frac{\zeta}{\eta}\right)^2 \exp(-2\zeta^2)\exp\left\{-\frac{2\zeta^2}{\nu^2}\left(\frac{1}{\eta}-1\right)^2\right\} \tag{7.6}$$

Where,

$$L = 1+\frac{\nu^2}{4}$$

Next, modified joint probability density function of wave height and wave period by replacing the mean frequency with the peak frequency of the wave system according to Zhang and Guedes Soares (2016)[55] is described by the Eq. 7.7

$$f(\zeta\,,\eta) = \frac{8L_c}{\alpha\sqrt{2\pi}\,\nu}\left(\frac{\zeta}{\eta}\right)^2 \exp(-2\zeta^2)\exp\left\{-\frac{2\zeta^2}{\nu^2}\left(1-\frac{1}{\alpha\eta}\right)^2\right\} \tag{7.7}$$

where,

$$L_c = 2\left(1+\frac{1}{\sqrt{\nu^2+1}}\right)^{-1}, \qquad \alpha = \frac{1}{\eta_p} = \frac{\omega_p}{\omega_{01}}$$

Improved modified joint probability density function of wave height and wave period by replacing to the peak frequency of the wave system and reducing the tail spread of the probability distribution is described by the Eq. 7.8.

$$f(\zeta,\eta) = \frac{8L_p}{\alpha\sqrt{2\pi}\,\nu}\left(\frac{\zeta}{\eta}\right)^2 \exp(-2\zeta^2)\exp\left\{-\frac{2\zeta^2}{\beta\nu^2}\left(1-\frac{1}{\alpha\eta}\right)^2\right\} \tag{7.8}$$

Where,

$$L_p = 2\left(1 + \frac{\gamma}{\sqrt{\gamma\nu^2 + 1}}\right)^{-1}, \qquad \beta = \begin{cases} 1, & \eta \le \eta_p \\ \gamma, & \eta > \eta_p \end{cases}$$

The calculation of the added resistance in short-term sea conditions is roughly divided into a method by the Spectrum method and a method by the probability density function (PDF) of the wave. To verify the validity of the proposed PDF method considering the non-linearity due to wave height derived in this study, PDF method based on the linear assumption of calculating the average added resistance in waves is compared with the Spectrum method.

- The Spectrum method based on the linear assumption

$$R_{AW}\left(H_{1/3}, T_{01}, V\right) = 2\int_0^\infty \frac{R_{WU}(\omega, V)}{{\zeta_a}^2} S\left(\omega \middle| H_{1/3}, T_{01}\right) d\omega \tag{7.9}$$

- PDF method based on the linear assumption

$$R_{AW}\left(H_{1/3}, T_{01}, V\right) = \int_0^\infty \int_0^\infty {\zeta_a}^2 R_{WU}(\omega, V) p\left(H, T \middle| H_{1/3}, T_{01}\right) dT dH \tag{7.10}$$

- PDF method considering wave height non-linearity

$$R_{AW}\left(H_{1/3}, T_{01}, V\right) = \int_0^\infty \int_0^\infty R_{WN}(H, T, V) p\left(H, T \middle| H_{1/3}, T_{01}\right) dT dH \tag{7.11}$$

7.3.1 Short-term prediction of added resistance in head seas for KCS

The added resistance in irregular waves is calculated by the SPE method (Eq. 7.1), the linear PDF method (Eq. 7.2 with $C(s) = 1$) and the nonlinear PDF method (Eq. 7.2 with $C(s)$) of Eq. 3.7). The probability density function $p\left(H, T \middle| H_{1/3}, T_{01}\right)$ is obtained from Eqs. 7.6. The frequency response transfer function of added resistance is estimated by the potential-based calculation based on Enhanced Unified Theory (EUT) referred in Yoshida, J. et al. (2016)[54]. The JONSWAP spectrum approximated by the significant wave height $H_{1/3}$ and mean wave period T_{01} is used.

It can be seen in Fig. 7.1 that the non-linearity against the wave height is sufficiently reflected in the calculation by the nonlinear PDF method. That means non-linearity is evident in regions where the mean wave period is less than 5s (regions with large wave steepness), and the average added wave resistance is smaller than linear calculations. The tendency is the same even if the speed of the ship is different, and the method of calculating the proposal is reasonable. This demonstrates the validity of the probability density function method if the spectrum method is positive.

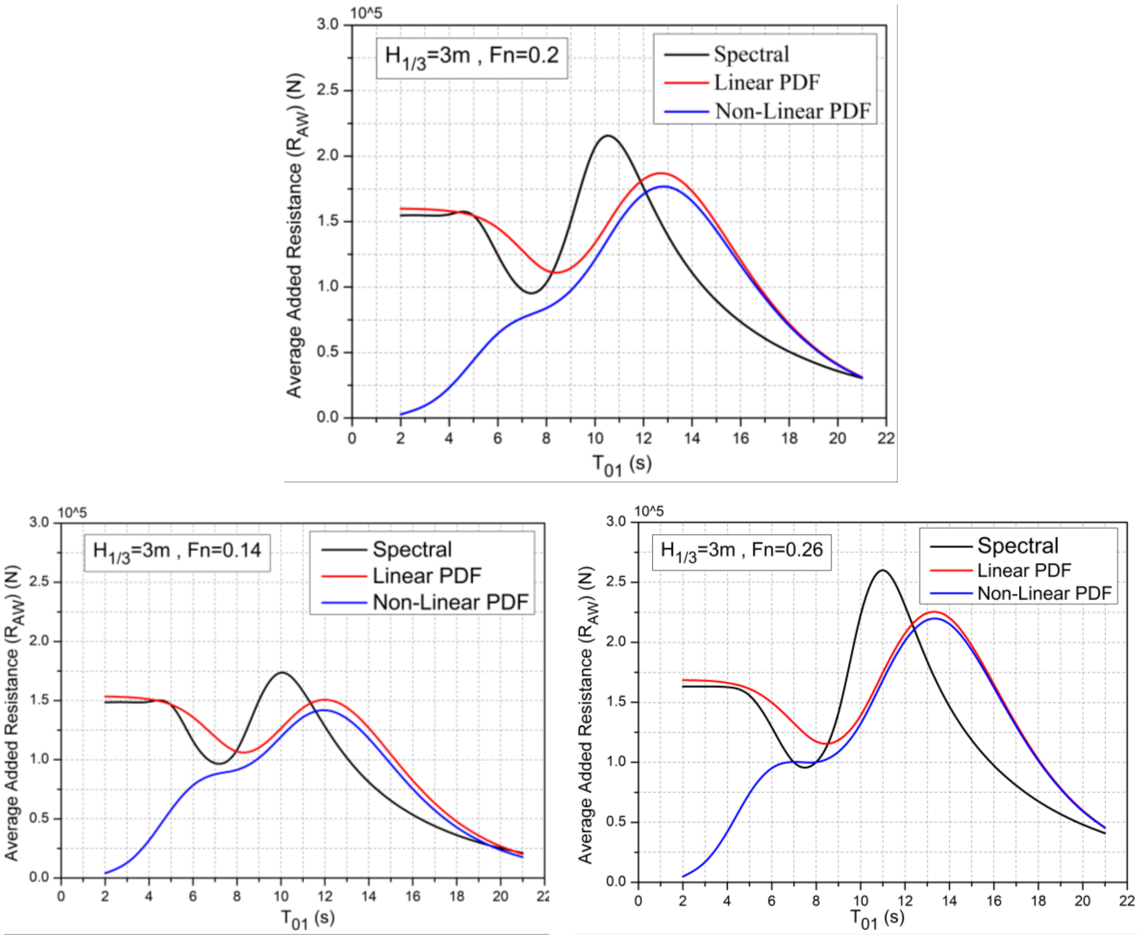

FIGURE 7.1 Comparison of average added resistances in irregular waves by a spectral method, linear pdf method, and nonlinear pdf method at $Fn = 0.14\ , 0.20, 0.26$.

But it showed a discrepancy with the conventional method based on spectral analysis i.e., wave period of the maximum added resistance was evaluated longer than the result of the spectrum method. The cause of peak and wave period difference is the discrepancy of joint probability density function with the distribution of wave heights and wave periods in the peak of the distribution when compared with the numerical simulations of waves under linear assumptions from the given wave spectrum. Further improvement in the method was needed. We estimated the improved results with modified joint probability density function with the distribution of wave heights and wave periods with the RIOS containership ship hull type.

7.3.2 Short-term predictions of added resistance for RIOS containership (head seas)

The added resistance in head seas irregular waves is calculated by the conventional Spectrum method (SPE) according to Eq. 7.1, the linear PDF method (Eq. 7.2 with $C(s) = 1$) and the nonlinear PDF method (Eq. 7.2 with $C(s)$ of Eq. 3.12). The probability density function $p(H, T|H_{1/3}, T_{01})$ is obtained from Eq. 7.6, 7.7, 7.8 of different Longuet-Higgins model. The frequency response transfer function of added resistance in oblique waves is estimated by the potential-based calculation based on Enhanced Unified Theory (EUT). The JONSWAP spectrum approximated by the significant wave height $H_{1/3}$ and mean wave period T_{01} is used.

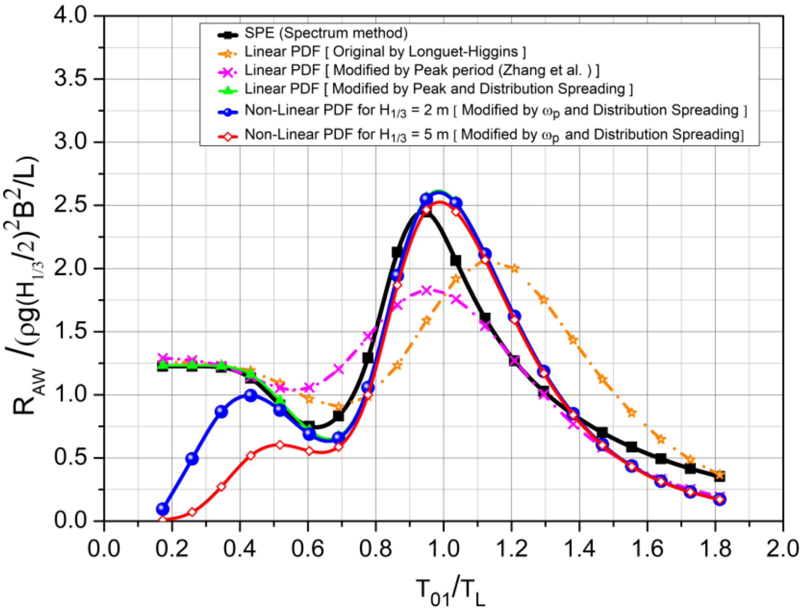

FIGURE 7.2 Comparison among the short-term prediction calculation results using conventional spectral method , original and modified linear PDF method and proposed non-linear PDF method in different significant wave heights.

When Eq. 7.6 expressing the probability density of waves by Longuet-Higgins is applied to Eq. 7.2 with $C(s) = 1$ describing the added resistance as the linear PDF method, the wave period of the maximum added resistance (orange star mark broken line) is evaluated longer than the result of the SPE method (black square mark line) by Eq. 7.1 as shown in Fig. 7.2. Here, T_L is the wave period of which wavelength corresponds to the ship length L and the ratio T_{01}/T_L is used as non-dimensionalized value. T_L is defined as Eq. 7.12.

$$T_L = \sqrt{\frac{2\pi}{g}L}. \tag{7.12}$$

On the other hand, when applying Eq. 7.7 formulating the wave probability density with the carrier wave period as the spectrum peak period by Zhang et al. to Eq. 7.2 as the linear PDF method, the wave period of the maximum added resistance becomes the same as the result of the SPE method. However, the tail in long-period regions ($T_{01}/T_L > 1.2$) and the maximum value is smaller than in the SPE method and in $0.5 < T_{01}/T_L < 0.8$ larger than in the SPE method. Furthermore, when the tail spread of the probability density function is reduced in addition to the correction of the carrier wave period described by Eq. 7.8 the maximum resistance is improved. The nonlinear PDF results were obtained by Eq. 7.2 with Eqs. 7.4 and 7.8. Fig. 7.2 shows that the added resistance decreases in the region of $T_{01}/T_L < 0.5$ than that of the linear method where the wave steepness is relatively higher. It is also shown that the rate of decrease increases as the wave height increases by comparing cases of 2m and 5m significant wave height.

7.3.3 Validation of short-term prediction results with experimental and CFD results in long crested irregular waves

To validate these prediction methods, we have compared with the results of CFD, and tank experiments as shown in Fig. 7.3. The top and bottom of vertical bar overladed under the circular marker indicate the maximum and minimum of experimental results. The quantitative difference between model tests and CFD simulations is at acceptable level of accuracy which is less than about ±10%. Hence, CFD simulations has been found to be a reliable result and the results at $T_{01}/T_L = 0.43, 0.52$ for $H_{1/3} = 2\mathrm{m}$ and at $T_{01}/T_L = 0.52$ for $H_{1/3} = 5\mathrm{m}$ are also reliable.

The objects of comparison are the results of the SPE method, and the nonlinear PDF method modified by peak and distribution spreading. The SPE method shows a better agreement with the experimental results and CFD results, while the non-linear PDF method shows the results in the acceptable range of accuracy with the CFD results showing underestimated values in $T_{01}/T_L \leq 1$ and overestimated values in the range $T_{01}/T_L > 1$ for two different significant wave heights. This argues that the proposed nonlinear PDF method is valid and can respond for the difference of wave height. The agreement at $T_{01}/T_L = 0.43,\ 0.52$ for $H_{1/3} = 2\mathrm{m}$ and at $T_{01}/T_L = 0.52$ for $H_{1/3} = 5\mathrm{m}$ complements this argument. In this sense, proposed nonlinear PDF method of calculating the added resistance in long crested irregular waves is reasonable and corresponds to wave-height non-linearity.

In overall, the added resistance results by the spectral method are in better agreement with the CFD and experimental results than the PDF method. This is because there are still deviations between the wave probability distributions from modified Longuet-Higgins model and CFD and experiment regarding the peak period and distribution spread. The proposed PDF model should be further improved.

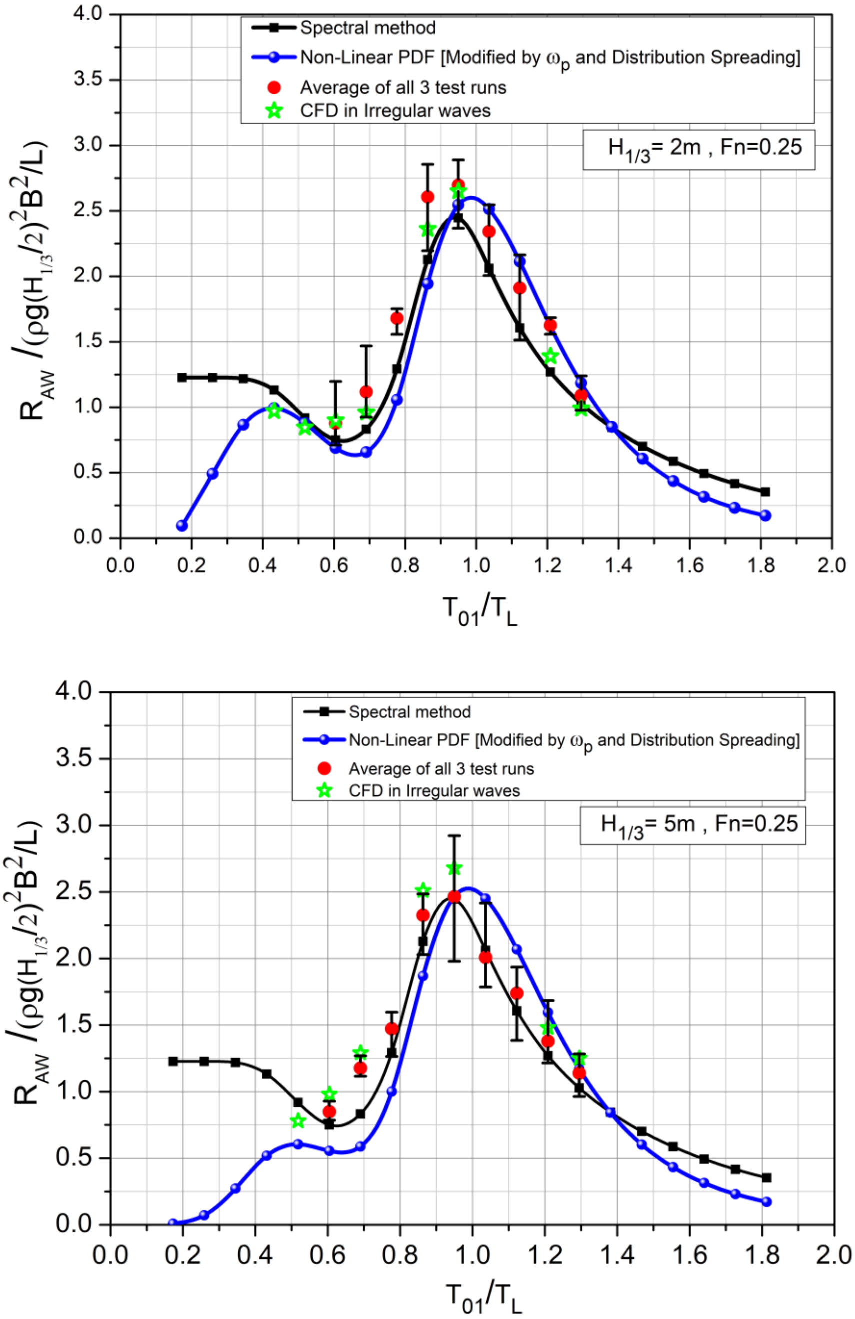

FIGURE 7.3 Comparison among the irregular wave resistance test and CFD numerical results of the non-dimensioned added wave resistance with the short-term prediction calculation results using conventional spectral method and proposed non-linear PDF method.

7.3.4 Validation of short-term prediction of added resistance with CFD results in Oblique bow waves.

The added resistance in oblique irregular waves is calculated by the conventional Spectrum method (SPE) according to Eq. 7.1, the linear PDF method (Eq. 7.2 with $C(s) = 1$) and the nonlinear PDF method (Eq. 7.2 with $C(s)$ of Eq. 3.13). The probability density function $p(H, T|H_{1/3}, T_{01})$ is obtained from Eq. 7.8 of the improved modified Longuet-Higgins model. Results has been shown in Fig. 7.4.

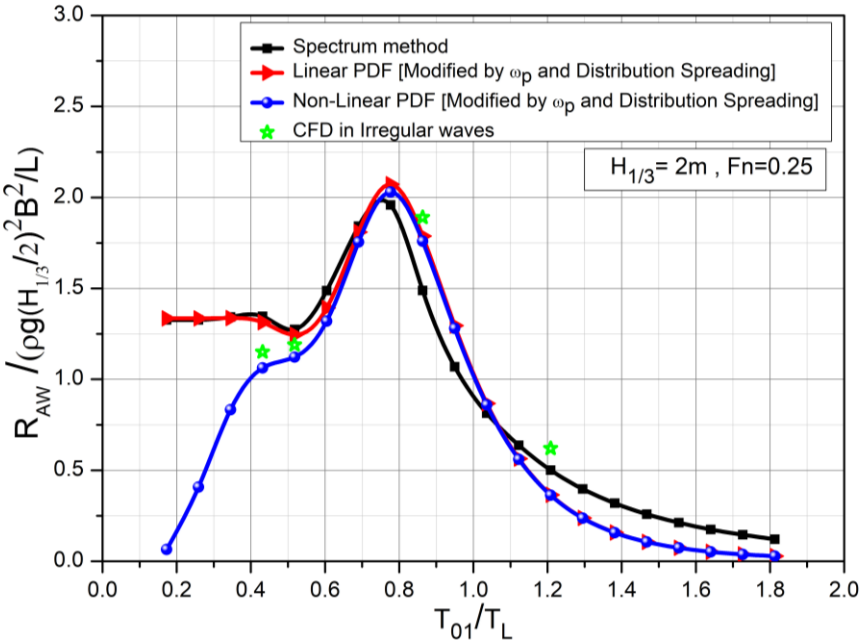

FIGURE 7.4 Comparison between CFD numerical results of the non-dimensionalized added resistance in oblique irregular waves with the short-term prediction calculation results using conventional spectrum method and non-linear PDF method.

It has been found that the SPE and PDF method based on the linear assumption give essentially the same tendency of the results shown in Fig. 7.4. This demonstrates the validity of the probability density function method in linear conditions. In the region where the normalized mean wave period is small, the nonlinear pdf method modified by peak and distribution spreading deviates significantly from the other two linear methods. It can be seen in Fig. 7.4 that the non-linearity against the wave height is sufficiently reflected in the calculation by the nonlinear PDF method. The tendency of added resistance decreases in the region of $T_{01}/T_L < 0.5$ than that of the linear method where the wave steepness is relatively higher.

To validate the proposed non-linear PDF short-term prediction method, we compared with results of SPE method and CFD in oblique irregular waves as shown in Fig. 7.4. The SPE method has been found to be a reliable result than PDF method on comparison with the CFD results showing overestimated values predicted by CFD. The reason behind overestimated values by CFD is use of mesh deformation technique. Results might be improved using overset mesh technique with adaptive grid refinement method. The PDF method is also close to the results of the SPE method, and particularly the peak positions correspond well. However, as a remarkable difference, the PDF method is smaller than the SPE method at $T_{01}/T_L < 0.78$, becomes larger at $0.78 < T_{01}/T_L < 1.06$ and it becomes smaller after $T_{01}/T_L = 1.06$. However, the agreement of CFD results at $T_{01}/T_L = 0.43,\ 0.52$ complements that the proposed nonlinear PDF method of calculating the added resistance in oblique irregular waves is reasonable and corresponds to the effect of non-linearity due to wave steepness. The non-linear probability density function method gives a nonlinearity-corrected average added resistance in obliques waves according to the magnitude of the wave steepness.

7.4 Conclusion

We proposed and validated a probabilistic method to estimate the added resistance in short-term head and oblique sea conditions that combines the nonlinearity due to wave height and wave steepness in the frequency domain with the encounter irregular wave statistics. The nonlinearity with respect to wave height and wave steepness is described as a correction function to the linear added resistance for wave height squared in the frequency domain. The statistics of irregular waves encountered are given by the joint probability density function of wave height and wave period in a short-term sea condition, which is the Longuet-Higgins density function with corrections of asymptotic wave period (mean wave period) in the probability distribution to the wave spectrum peak period and reduction in the width of the probability distribution spreading in larger wave period.

Chapter 8

General conclusions and recommendations

Finally, it has to be admitted that the modified Longuet-Higgins model using joint probability distribution in this paper still deviates from the numerical simulations of waves under linear assumptions of JONSWAP spectrum and this proposed method is highlighting the right direction and possibly alternative formulations could help in further improvements. The modified theoretical model is essentially an alternative form of Longuet-Higgins joint distribution which could not fundamentally eliminate the disparities with numerical simulations but is theoretically possible to be used in estimation of added resistance including wave height non-linearities. But until now, only few efforts have been contributed by other researcher in this topic and a little improvement has been achieved as it becomes more complex when simultaneously involving two correlated random variables in one distribution function. The findings obtained by comparing added resistance estimated by the nonlinear PDF method, the prediction by the spectrum method, the experimental data, and the CFD analysis are summarized below.

- The linearity of the added resistance to the wave height squared is no longer satisfied as wave steepness increases. The correction function applied for this nonlinearity can be expressed exponentially using the results of relative comparisons of CFD calculations.

- Comparison with a time series simulated model with JONSWAP spectrum showed a discrepancy in the peak of the distribution and various improvements are introduced in the original Longuet-Higgins model to estimate the added resistance in short term sea conditions using Probability density function method.

- The joint probability density function of wave height and wave period of the improved Longuet-Higgins model is suitable as the probability distribution of waves has been improved. Modification in the wave period range was performed. One of the improvements of asymptotic wave period (mean wave period) in the probability distribution to the wave spectrum peak period and other is the reduction in the width of the probability distribution spreading in the larger wave period range.

- The joint probability density function of the wave height and heave motion height was verified by the numerical analysis, and it is confirmed that the heave oscillations were synchronized as the average wave period increased, indicating the validity of this paper. The longer the mean wave period , the more the heave motions synchronized.

- However, the added resistance results by the spectral method are in better agreement with the CFD and experimental results than the PDF method. Hence, PDF method has scope of further improvement. With the proposed PDF method in this paper, the characteristics of nonlinearity with respect to wave height appear especially on the short-mean-wave-period region, and it is shown that as the wave height increases, the added resistance per unit wave height becomes relatively small.

- PDF method is also valid in estimation of added resistance in oblique sea conditions. It demonstrates the fair results in comparison to spectrum method and in an acceptable range of accuracy with CFD numerical results in irregular oblique waves.

- The proposed nonlinear PDF method uses CFD to determine the relative ratio of nonlinearity to linearity, which is calculated at a few representative frequencies. Therefore, it predicts the added resistance in irregular waves considering the nonlinearity with respect to wave height in less time than the direct estimation by CFD.

Appendix A

Ridge line of the probability density function

A ridge can be defined as the position where the slope of the probability density function with respect to η is 0. i.e.

$$\frac{df(\zeta,\eta)}{d\eta} = 0 \tag{A.1}$$

A combination of ζ, η that satisfies is a ridge. Differentiating the probability density function in Eq. 5.60 with respect to η.

$$\begin{aligned}\frac{df(\zeta,\eta)}{d\eta} &= f(\zeta,\eta)\left(-\frac{2}{\eta} - 4\frac{\zeta^2}{\nu^2}\left(\frac{1}{\eta} - 1\right)\left(\frac{-1}{\eta^2}\right)\right) \\ &= f(\zeta,\eta)\frac{2}{\eta^3}\left(-\eta^2 + 2\frac{\zeta^2}{\nu^2}(1-\eta)\right)\end{aligned} \tag{A.2}$$

Therefore, from equation (A. 1)

$$\eta^2 - 2\frac{\zeta^2}{\nu^2}(1-\eta) = 0 \tag{A.3}$$

By transforming this, the equation for drawing a ridge can be obtained as follows.

$$\zeta = \frac{\nu\eta}{2\sqrt{1-\eta}} \tag{A.4}$$

Alternatively, the following equation is used as the solution to the η of equation (A. 3).

$$\eta = \frac{\zeta^2}{\nu^2}\left(-1 + \sqrt{1 + \frac{2\nu^2}{\zeta^2}}\right)$$

Also, transformed as follows:

$$\frac{\eta^2}{\zeta^2} - \frac{2}{\nu^2}(1-\eta) = 0$$

Considering the limit of $\zeta \to \infty$, we obtain the following equation.

$$\eta = 1 \tag{A.5}$$

From this, it can be seen that the ridge of the probability density function is asymptotic to a straight line of $\eta = 1$.

Appendix B

Calculation of correlation function of time series model.

Find the correlation function of the following two time series models.

$$f(t)=\sum_{n=1}^{\infty}a_n\cos\{(\omega_n-\omega_m)t-\theta_n+\varepsilon_n\}=\sum_{n=1}^{\infty}a_n\cos\{(n-m)\omega_0 t-\theta_n+\varepsilon_n\} \tag{B1}$$

$$g(t)=\sum_{n=1}^{\infty}b_n\cos\{(\omega_n-\omega_p)t-\psi_n+\varepsilon_n\}=\sum_{n=1}^{\infty}b_n\cos\{(n-p)\omega_0 t-\psi_n+\varepsilon_n\} \tag{B2}$$

Here, ω_0 is the minimum frequency when the measurement interval is T_P and is expressed by the following equation.

$$\omega_0=\frac{2\pi}{T_P}$$

m and p are integers greater than or equal to 0, and ε_n is an independent uniform random phase from $0\sim 2\pi$. Generally, m,p are arbitrary integers, but since this appendix can also be used for of "Simultaneous occurrence probability of wave and ship motion", ω_m means the average frequency of the wave and ω_p the average frequency of the ship motion and m,p are its serial number.

$$\omega_m=m\omega_0$$
$$\omega_p=p\omega_p$$

a_n,b_n,θ_n,ψ_n are values that do not change even if the time series data set (interval T_P data set) is different, but the combination of ε_n is different for each data set. At $m=p$, the average frequencies of the waves and the ship motions coincide.

- Correlation function between $f(t)$ and $g(t)$.

$$C_{fg}(\tau)=\sum_{n=1}^{\infty}\frac{1}{2}a_nb_n\cos(-(n-m)\omega_0\tau-\theta_n+\psi_n) \tag{B3}$$

- Correlation function between $f(t)$ and $\dot{g}(t)$.

$$C_{f\dot{g}}(\tau)=\sum_{n=1}^{\infty}\frac{1}{2}a_nb_n(n-m)\omega_0\sin(-(n-m)\omega_0\tau-\theta_n+\psi_n) \tag{B4}$$

- Correlation function between $\dot{f}(t)$ and $g(t)$.

$$C_{\dot{f}g}(\tau) = \sum_{n=1}^{\infty} -\frac{1}{2} a_n b_n (n-m)\omega_0 \sin(-(n-m)\omega_0\tau - \theta_n + \psi_n) \tag{B5}$$

- Correlation function between $\dot{f}(t)$ and $\dot{g}(t)$.

$$C_{\dot{f}\dot{g}}(\tau) = \sum_{n=1}^{\infty} \frac{1}{2} a_n b_n (n-p)^2 {\omega_0}^2 \cos(-(n-m)\omega_0\tau - \theta_n + \psi_n) \tag{B6}$$

✓ **Autocovariance of the $\boldsymbol{x_c}, \boldsymbol{x_s}$ is given by $\boldsymbol{c_{xcxc}}, \boldsymbol{c_{xsxs}}$.**

The autocorrelation functions of x_c is given by equations (B1) and (B2) are

$$f = g = x_c$$

$$b_n = a_n$$

$$\psi_n = \theta_n = 0$$

$$p = c$$

Equation (B3) gives the auto-covariance case where

$$C_{xcxc}(\tau) = \sum\nolimits_{n=1}^{\infty} \frac{1}{2} a_n a_n \cos\big((n-c)\omega_0\tau\big) \tag{B7}$$

From this, the auto-covariance becomes

$$c_{xcxc} = C_{xcxc}(0) = \sum\nolimits_{n=1}^{\infty} \frac{1}{2} a_n a_n \tag{B8}$$

Since this is equivalent to equation (5.13), using the wave power spectrum, c_{xcxc} can be expressed as

$$c_{xcxc} = \int_0^{\infty} E_{xx}(\omega) d\omega = m_0 \tag{B9}$$

Generally, wave information is given by wave power spectrum c_{xcxc}, not by wave amplitude a_n, so, this formula is useful for calculation of $E_{xx}(\omega)$.

The autocorrelation functions of x_s in equations (B1) and (B2) are

$$f = g = x_s$$

$$b_n = a_n$$

$$\psi_n = \theta_n = \frac{\pi}{2}$$

$$p = c$$

Equation (B3) is the case where

$$C_{xsxs}(\tau) = \sum_{n=1}^{\infty} \frac{1}{2} a_n a_n \cos\big((n-c)\omega_0 \tau\big) \tag{B10}$$

Since this is the same as equation (B7), the following series of relationships hold

$$C_{xsxs}(\tau) = C_{xcxc}(\tau)$$

$$c_{xsxs} = c_{xcxc} = \int_0^{\infty} E_{xx}(\omega) d\omega = m_0 \tag{B11}$$

In addition, The spectrum obtained by the Fourier transform of $S_{xcxc}(\omega)$ is $C_{xcxc}(\tau)$

$$S_{xcxc}(\omega) \neq S_{xx}(\omega)$$

although

$$\int_{-\infty}^{\infty} S_{xcxc}(\omega) d\omega = \int_{-\infty}^{\infty} S_{xx}(\omega) d\omega$$

✓ **Autocovariance of the $\dot{x}_c, \dot{x}_s$ is given by $c_{\dot{x}c\dot{x}c}, c_{\dot{x}s\dot{x}s}$**

The autocorrelation functions of $\dot{x}_c$ in equations (B1) and (B2) are

$$f = g = x_c$$

$$b_n = a_n$$

$$\psi_n = \theta_n = 0$$

$$p = c$$

Equation (B6) with

$$C_{\dot{x}c\dot{x}c}(\tau) = \sum_{n=1}^{\infty} \tfrac{1}{2} a_n a_n (n-c)^2 {\omega_0}^2 \cos\big((n-c)\omega_0 \tau\big) \tag{B12}$$

From this, the auto-covariance becomes

$$c_{\dot{x}c\dot{x}c} = C_{\dot{x}c\dot{x}c}(0) = \sum_{n=1}^{\infty} \tfrac{1}{2} a_n a_n \, (n-c)^2 {\omega_0}^2 \tag{B13}$$

By the way, if we multiply the wave power spectrum of equation (5.12) by $(\omega - \omega_c)^2$ and integrate with respect to ω.

$$\int_0^{\infty} (\omega - \omega_c)^2 E_{xx}(\omega) d\omega = \int_0^{\infty} (\omega - \omega_c)^2 2 S_{xx}(\omega) d\omega$$

$$= \int_0^{\infty} (\omega - \omega_c)^2 2 \sum_{n=1}^{\infty} \frac{1}{4} {a_n}^2 \{\delta(\omega - n\omega_0) + \delta(\omega + n\omega_0)\} \, d\omega$$

$$= \sum_{n=1}^{\infty} \frac{1}{2} {a_n}^2 \int_0^{\infty} (\omega - \omega_c)^2 \{\delta(\omega - n\omega_0) + \delta(\omega + n\omega_0)\} d\omega$$

$$= \sum_{n=1}^{\infty} \frac{1}{2} {a_n}^2 (n\omega_0 - \omega_c)^2$$

$$= \sum_{n=1}^{\infty} \frac{1}{2} {a_n}^2 (n-c)^2 {\omega_0}^2$$

which is the same as the result of Eq. (B.13). Therefore, the following equation holds.

$$c_{\dot{x}c\dot{x}c} = \int_0^\infty (\omega - \omega_c)^2 E_{xx}(\omega) d\omega \tag{B14}$$

The moment order can be divided as follows.

$$\begin{aligned} c_{\dot{x}c\dot{x}c} &= \int_0^\infty \omega^2 E_{xx}(\omega) d\omega - 2\omega_c \int_0^\infty \omega E_{xx}(\omega) d\omega + {\omega_c}^2 \int_0^\infty E_{xx}(\omega) d\omega \\ &= m_2 - 2\omega_c m_1 + {\omega_c}^2 m_0 \end{aligned} \tag{B15}$$

The autocorrelation functions of $\dot{x}_s$ in equations (B1) and (B2) are

$$f = g = x_s$$

$$b_n = a_n$$

$$\psi_n = \theta_n = \frac{\pi}{2}$$

$$p = c$$

From equation (B6), it becomes

$$C_{\dot{x}s\dot{x}s}(\tau) = \sum_{n=1}^{\infty} \frac{1}{2} a_n a_n (n-c)^2 {\omega_0}^2 \cos\big((n-c)\omega_0 \tau\big) \tag{B16}$$

Since this is the same as equation (B.12), the following series of relations hold.

$$C_{\dot{x}s\dot{x}s}(\tau) = C_{\dot{x}c\dot{x}c}(\tau)$$

$$c_{\dot{x}s\dot{x}s} = c_{\dot{x}c\dot{x}c} = \int_0^\infty (\omega - \omega_c)^2 E_{xx}(\omega) d\omega = m_2 - 2\omega_c m_1 + {\omega_c}^2 m_0 \tag{B17}$$

✓ **Cross-covariance of the two x_c and $\dot{x}_c$ is given by $c_{xc\dot{x}c}$**

The cross-correlation function of x_c and $\dot{x}_c$ is given by equations (B1) and (B2).

$$f = g = x_c$$

$$b_n = a_n$$

$$\psi_n = \theta_n = 0$$

$$p = c$$

From equation (B4), it becomes

$$C_{xc\dot{x}c}(\tau) = \sum_{n=1}^{\infty} \frac{1}{2} a_n a_n (n-c)\omega_0 \sin(-(n-c)\omega_0 \tau) \tag{B18}$$

The cross covariance becomes

$$c_{xc\dot{x}c} = C_{xc\dot{x}c}(0) = 0 \tag{B19}$$

Regarding the cross-covariance, it is the same even if the order of x_c and $\dot{x}_c$ is interchanged, and we obtain,

$$c_{\dot{x}cxc} = C_{\dot{x}cxc}(0) = 0 \tag{B20}$$

✓ **Cross covariance of the two x_c and x_s is given by c_{xcxs}**

The cross-correlation function of x_c and x_s is given by equations (B1) and (B2).

$$f = x_c$$
$$g = x_s$$
$$b_n = a_n$$
$$\theta_n = 0$$
$$\psi_n = \frac{\pi}{2}$$
$$p = c$$

using Equation (B3) ,

$$C_{xcxs}(\tau) = \sum_{n=1}^{\infty} \frac{1}{2} a_n a_n \cos\left(-(n-c)\omega_0\tau + \frac{\pi}{2}\right)$$
$$= \sum_{n=1}^{\infty} \frac{1}{2} a_n a_n \sin\big((n-c)\omega_0\tau\big) \quad \text{(B21)}$$

The Cross covariance would be as follows

$$c_{xcxs} = C_{xcxs}(0) = 0 \quad \text{(B22)}$$

Cross covariance is the same even if the order of x_c and x_s is interchanged , and we obtain the following equation,

$$c_{xsxc} = C_{xsxc}(0) = 0 \quad \text{(B23)}$$

✓ **Cross covariance of the two $\mathbf{x_c}$ and $\mathbf{\dot{x}_s}$ is given by $\mathbf{c_{xc\dot{x}s}}$**

The cross-correlation function of x_c and $\dot{x}_s$ is given by equations (B1) and (B2).

$$f = x_c$$
$$g = x_s$$
$$b_n = a_n$$
$$\theta_n = 0$$
$$\psi_n = \frac{\pi}{2}$$
$$p = c$$

Equation (B3) with

$$C_{xc\dot{x}s}(\tau) = \sum_{n=1}^{\infty} \frac{1}{2} a_n a_n (n-c)\omega_0 \sin\left(-(n-c)\omega_0\tau + \frac{\pi}{2}\right)$$
$$= -\sum_{n=1}^{\infty} \frac{1}{2} a_n a_n (n-c)\omega_0 \sin\left((n-c)\omega_0\tau - \frac{\pi}{2}\right)$$

$$= \sum_{n=1}^{\infty} \frac{1}{2} a_n a_n (n-c)\omega_0 \cos\big((n-c)\omega_0 \tau\big) \tag{B24}$$

As a result, cross covariance is,

$$c_{xc\dot{x}s} = C_{xc\dot{x}s}(0) = \sum_{n=1}^{\infty} \frac{1}{2} a_n a_n (n-c)\omega_0$$

$$= \sum_{n=1}^{\infty} \frac{1}{2} n\omega_0 {a_n}^2 - c\omega_0 \sum_{n=1}^{\infty} \frac{1}{2} {a_n}^2$$

However, by applying equations (5.13), (5.14) and (5.16), we obtain

$$c_{xc\dot{x}s} = m_1 - c\omega_0 m_0 = m_0\omega_{01} - \omega_c m_0 = m_0(\omega_{01} - \omega_c) \tag{B25}$$

is the same as in the previous example. However, $\omega_{01} = m_1/m_0$ was applied. Therefore

$$c_{xc\dot{x}s} = C_{xc\dot{x}s}(0) = m_0(\omega_{01} - \omega_c) \tag{B26}$$

Cross covariance is the same even if the order of the two x_c and $\dot{x}_s$ is interchanged , and we obtain the following equation,

$$c_{\dot{x}sxc} = C_{\dot{x}sxc}(0) = m_0(\omega_{01} - \omega_c) \tag{B27}$$

✓ **Cross covariance of the two $\dot{x}_c$ and x_s is given by $c_{\dot{x}cxs}$.**

The cross-correlation function of $\dot{x}_c$ and x_s is given by equations (B1) and (B2).

$$f = x_c$$

$$g = x_s$$

$$b_n = a_n$$

$$\theta_n = 0$$

$$\psi_n = \frac{\pi}{2}$$

$$p = c$$

From Equation (B5) , we get

$$C_{\dot{x}cxs}(\tau) = \sum_{n=1}^{\infty} -\frac{1}{2} a_n a_n (n-c)\omega_0 \sin\left(-(n-c)\omega_0\tau + \frac{\pi}{2}\right)$$

$$= \sum_{n=1}^{\infty} -\frac{1}{2} a_n a_n (n-c)\omega_0 \cos\big((n-c)\omega_0\tau\big) \tag{B28}$$

From this, the cross covariance becomes

$$c_{\dot{x}cxs} = C_{\dot{x}cxs}(0) = -\sum_{n=1}^{\infty} \frac{1}{2} a_n a_n (n-c)\omega_0$$

$$= -\sum_{n=1}^{\infty} \frac{1}{2} n\omega_0 {a_n}^2 + c\omega_0 \sum_{n=1}^{\infty} \frac{1}{2} {a_n}^2$$

but by applying equations (5.13), (5.14) and (5.16), we obtain

$$c_{\dot{x}cxs} = -m_1 + c\omega_0 m_0 = -m_0\omega_{01} + \omega_c m_0 = -(\omega_{01} - \omega_c)m_0$$

is. Therefore, the

$$c_{\dot{x}cxs} = C_{\dot{x}cxs}(0) = -(\omega_{01} - \omega_c)m_0 \tag{B29}$$

Cross covariance is the same even if the order of the two $\dot{x}_c$ and x_s is interchanged , and we obtain the following equation,

$$c_{xs\dot{x}c} = C_{xs\dot{x}c}(0) = -(\omega_{01} - \omega_c)m_0 \tag{B30}$$

✓ **Cross covariance of the two $\dot{x}_c$ and $\dot{x}_s$ is given by $c_{\dot{x}c\dot{x}s}$**

The cross-correlation function of $\dot{x}_c$ and $\dot{x}_s$ is given by equations (B1) and (B2).

$$f = x_c$$

$$g = x_s$$

$$b_n = a_n$$

$$\theta_n = 0$$

$$\psi_n = \frac{\pi}{2}$$

$$p = c$$

From equation (B6) ,

$$C_{\dot{x}c\dot{x}s}(\tau) = \sum_{n=1}^{\infty} \frac{1}{2} a_n a_n (n-c)^2 \omega_0{}^2 \cos\left(-(n-c)\omega_0\tau + \frac{\pi}{2}\right)$$

$$= \sum_{n=1}^{\infty} \frac{1}{2} a_n a_n (n-c)^2 \omega_0{}^2 \sin\big((n-c)\omega_0\tau\big) \tag{B31}$$

From this, the cross covariance becomes

$$c_{\dot{x}c\dot{x}s} = C_{\dot{x}c\dot{x}s}(0) = 0 \tag{B32}$$

and $\dot{x}_c$ and $\dot{x}_s$ are the same even if the order of the two is interchanged, we obtained ,

$$c_{\dot{x}s\dot{x}c} = C_{\dot{x}s\dot{x}c}(0) = 0 \tag{B33}$$

✓ **Cross covariance of the two x_s and $\dot{x}_s$ is given by $c_{xs\dot{x}s}$**

$x_s$and $\dot{x}_s$ in equations (B1) and (B2) are the cross-correlation functions of

$$f = x_c$$

$$g = x_s$$

$$b_n = a_n$$

$$\theta_n = \psi_n = \frac{\pi}{2}$$

$$p = c$$

Equation (B4) with

$$C_{xs\dot{x}s}(\tau) = \sum_{n=1}^{\infty} -\frac{1}{2} a_n a_n (n-c)\omega_0 \sin\big((n-c)\omega_0\tau\big) \tag{B34}$$

From this, the cross covariance becomes

$$c_{xs\dot{x}s} = C_{xs\dot{x}s}(0) = 0 \tag{B35}$$

and x_s and $\dot{x}_s$ are the same even if the order of the two is interchanged, we obtained ,

$$c_{\dot{x}sxs} = C_{\dot{x}sxs}(0) = 0 \tag{B36}$$

Bibliographies

[1] B.J. Guo, S. Steen, and G.B. Deng. (2012) Seakeeping prediction of kvlcc2 in head waves with rans. *Applied Ocean Research*, 35:56–57.

[2] Dalzell, J. F. (1974). “Cross-Bispectral Analysis: Application to Ship Resistance in Waves”, *Journal of Ship Research*, 18, 1, 62-72.

[3] Dalzell, J. F., Kim, C. H. (1979). “An Analysis of the Quadratic Frequency Response for Added Resistance”, *Journal of Ship Research*, 23, 3, 198-208.

[4] el Moctar, O., Sigmund, S., Ley, J., & Schellin, T. E. (2017). Numerical and experimental analysis of added resistance of ships in waves. *Journal of Offshore Mechanics and Arctic Engineering*, 139(1), 1–9.

[5] Gao, Q., Song, L., & Yao, J. (2021). Rans prediction of wave-induced ship motions, and steady wave forces and moments in regular waves. *Journal of Marine Science and Engineering*, 9(12)

[6] Gerritsma, J., & Journée, J. M. J. (1978). Added resistance in oblique waves. Part 2, pp.70.

[7] Ghadimi, P., Karami, S., & Nazemian, A. (2021). Numerical simulation of the seakeeping of a military trimaran hull by a novel overset mesh method in regular and irregular waves. *Scientific Journals Maritime University of Szczecin, Zeszyty Naukowe Akademia Morska w Szczecinie*, 65(137), 1–13.

[8] Faltinsen, O.M. (1990) Sea Loads on Ships and Offshore Structures. *Cambridge University Press*, 1-5.

[9] Hirayama, T., & Wang, X. (1993). Simple Estimation of Wave Added Resistance from Experiments in Transient and Irregular Water Waves. *Journal of the Society of Naval Architects of Japan*, 1993(174), 275–287.

[10] Hironori Yasukawa, Akinori Matsumoto, Osamu Ikezoe.(2016) “Wave Height Effect on added Resistance of full hull ships in waves” *Transactions of the Japan Society of Naval Architects and Ocean Engineers*, 23, p. 45-54, (in Japanese)

[11] Hsu, F. H., Blenkarn, K. A. (1970). “Analysis of Peak Mooring Force Caused by Slow Vessel Drift Oscillation in Random Seas”, *Offshore Technology Conference* 1159, I135-I146.

[12] ITTC, 2011. ITTC - *Recommended Procedures and Guidelines : Practical Guidelines for Ship CFD Applications.*

[13] ITTC, 2017a. *Recommended Procedures and Guidelines* - *Seakeeping Experiments.*

[14] Islam, H., Rahaman, M., & Akimoto, H. (2019). Added Resistance Prediction of KVLCC2 in Oblique Waves. *American Journal of Fluid Dynamics*, 9(1), 13–26.

[15] Jawa, S., Minoura, M., & Idomoto, Y. (2022). Short-Term Prediction of Nonlinear Added Resistance in Head Sea with Probability Density Function Method. *In The 32nd International Ocean and Polar Engineering Conference* (p. ISOPE-I-22-508).

[16] KCS added resistance for variable heading. *SNAME 5th World Maritime Technology Conference*, WMTC 2015, 1–15.

[17] Kim, B. S., & Kim, Y. (2018). CFD application for prediction of ship added resistance in waves. *13th ISOPE Pacific/Asia Offshore Mechanics Symposium*, PACOMS 2018, 4(3), 9–15.

[18] Kobayashi, H., Kume, K., Orihara, H., Ikebuchi, T., Aoki, I., Yoshida, R., Yoshida, H., Ryu, T., Arai, Y., Katagiri, K., Ikeda, S., Yamanaka, S., Akibayashi, H., & Mizokami, S. (2021). Parametric study of added resistance and ship motion in head waves through RANS: Calculation guideline. *Applied Ocean Research*, 110(October 2019), 102573.

[19] Kobayashi, M. (2007). Consideration on the added resistance and speed drop of a ship with forward speed in irregular waves. *Conf Proc Soc Nav Archit Jpn*, 4, 251–254. (in Japanese).

[20] Kashiwagi M (1992) Added resistance, wave-induced steady sway force and yaw moment on an advancing ship. *Schiffstechnik* 39(1):3-16

[21] Kunpeng, C., Fan, Y., & Yunlong, D. (2021). RANS CFD seakeeping simulation for an 82k DWT vessel in head and oblique waves. Journal of Physics: *Conference Series*, 1834(1).

[22] Kuroda, M., Takagi, K. (2018). "Slowly-varying Added Resistance in Irregular Waves in Consideration of Higher Order Components", *Journal of the Japan Society of Naval Architects and Ocean Engineers*, 28, 37-43.

[23] Lagemann, B. (2019). Efficient seakeeping performance predictions with CFD.

[24] Lang, X., Mao, W., 2020. A semi-empirical model for ship speed loss prediction at head sea and its validation by full-scale measurements. *Ocean Eng*. 209, 107494.

[25] Lee, S. H., Paik, K. J., & Lee, J. H. (2022). A study on ship performance in waves using a RANS solver, part 2: Comparison of added resistance performance in various regular and irregular waves. *Ocean Engineering*, 263(June), 112174.

[26] Lee, J. H., Kim, Y., Kim, B. S., & Gerhardt, F. (2021). Comparative study on analysis methods for added resistance of four ships in head and oblique waves. *Ocean Engineering*, 236, 109552.

[27] Lee, J, Park, D-M, Kim, Y, 2017. Experimental investigation on the added resistance of modified KVLCC2 hull forms with different bow shapes. *Proc. Ins. Mech. Engineers, Part M: Journal of Engineering for the Maritime Environment* 231 (2), 395–410.

[28] Ley, Jens & Sigmund, Sebastian & el Moctar, Ould. (2014). Numerical Prediction of the Added Resistance of Ships in Waves. *Proceedings of the International Conference on Offshore Mechanics and Arctic Engineering - OMAE*. 2. 10.1115/OMAE2014-24216.

[29] Liu, S., & Papanikolaou, A. D. (2011). Time-domain hybrid method for simulating large amplitude motions of ships advancing in waves. *International Journal of Naval Architecture and Ocean Engineering*, *3*(1), 72–79. https://doi.org/10.2478/jnaoe-2013-0047

[30] Longuet-Higgins, M. S., 1975. On the joint distribution of the periods and amplitudes of sea waves, *J. Geophysics. Res.*, 80(18): 2688 - 2694.

[31] Longuet-Higgins, M. S. (1983). "On the Joint Distribution of Wave Periods and Amplitudes in a Random Wave Field", *Proc. of the Royal Society of London, Series A, Mathematical and Physical Sciences*, A.389, 241-258.

[32] Mancini, S., De Luca, F., Ramolini, A. (2017). Towards CFD guidelines for planing hull simulations based on the Naples Systematic Series. In: *7th International Conference on Computational Methods in Marine Engineering, MARINE* 2017, pp. 1071–1085.

[33] M. Kashiwagi (1997). Numerical Seakeeping Calculations Based on the Slender Ship Theory, *Ship Technology Research (Schiffstechnik)*, Vol.4, No.4, pp.167～192.

[34] M. Kashiwagi, S. Mizokami, H. Yasukawa, Y. Fukushima (2000). Prediction of Wave Pressure and Loads on Actual Ships by the Enhanced Unified Theory, *Proc. of 23rd Symposium on Naval Hydrodynamics*, pp.95～109.

[35] Mousavi, S. M., Khoogar, A. R., & Ghasemi, H. (2020). Time domain simulation of ship motion in irregular oblique waves. *Journal of Applied Fluid Mechanics*, 13(2), 549–559.

[36] NUMECA. Theoretical manual fine/marine. *https://www.numeca.com/product/finemarine*.

[37] Ochi,M.k (1998), "Ocean Waves - The Stochastic Approach" *Cambridge University Press,*

[38] Park, D. M., Kim, Y., Seo, M. G., & Lee, J. (2016). Study on added resistance of a tanker in head waves at different drafts. *Ocean Engineering*, 111, 569–581.

[39] Park, D. M., Lee, J. H., Jung, Y. W., Lee, J., Kim, Y., & Gerhardt, F. (2019). Experimental and numerical studies on added resistance of ship in oblique sea conditions. *Ocean Engineering*, 186, 106070.

[40] Peng, G. S., Gao, Y., Wen-Hua, W., Lin, L., & Huang, Y. (2020). Numerical Method to

Simulate Self-Propulsion of Aframax Tanker in Irregular Waves. *Mathematical Problems in Engineering*, 2020.

[41] P. Queutey and M. Visonneau (2007). An interface capturing method for free-surface hydrodynamic flows. Comput. Fluids, 36(9):1481–1510.

[42] Rahaman, M. M., Islam, H., Akimoto, H., & Islam, M. R. (2017). Motion predictions of ships in actual operating conditions using potential flow-based solver. *Journal of Naval Architecture and Marine Engineering*, 14(1), 65–76.

[43] Sadat-Hosseini, H., Wu, P. C., Carrica, P. M., Kim, H., Toda, Y., & Stern, F. (2013). CFD verification and validation of added resistance and motions of KVLCC2 with fixed and free surge in short and long head waves. *Ocean Engineering*, 59, 240–273.

[44] Sanada, Y., Kim, D. H., Sadat-Hosseini, H., Stern, F., Hossain, M. A., Wu, P. C., Toda, Y., Otzen, J., Simonsen, C., Abdel-Maksoud, M., Scharf, M., & Grigoropoulos, G. (2022). Assessment of EFD and CFD capability for KRISO Container Ship added power in head and oblique waves. *Ocean Engineering*, 243(January 2021), 110224.

[45] Seo, M. G., Yang, K. K., Park, D. M., & Kim, Y. (2014). Numerical analysis of added resistance on ships in short waves. *Ocean Engineering*, 87, 97–110.

[46] Seo, M. G., Ha, Y. J., Nam, B. W., & Kim, Y. (2021). Experimental and numerical analysis of wave drift force on KVLCC2 moving in Oblique waves. *Journal of Marine Science and Engineering*, 9(2),

[47] Sigmund, S., & el Moctar, O. (2018). Numerical and experimental investigation of added resistance of different ship types in short and long waves. *Ocean Engineering*, 147(October 2017), 51–67.

[48] Stocker, M. R. (2016). Surge free added resistance tests in oblique wave headings for the KRISO container ship model. *In The University of lowa.*

[49] Tsujimoto, M., Shibata, K., Ohmatsu, S., Kuroda, M., & Fujiwara, T. (2008). Development of a Practical Calculation Method for Added Resistance in Short Waves.

[50] Valanto, P. and Hong, Y.P. (2015). Experimental Investigation on Ship Wave Added Resistance in Regular Head, Oblique, Beam, and Following Waves, *Proceedings of the Twenty-fifth International Ocean and Polar Engineering Conference*

[51] WANG Xujie, ZHANG Ri, ZHAO Jing, et al. (2022) Study on Wave Added Resistance of Ships in Oblique Waves Based on Panel Method[J]. *Journal of Ocean University of China*, , 21(3): 773-781.

[52] J. Wackers, B. Koren, H. C. Raven, A. van der Ploeg, A. R. Starke, G. B. Deng, P. Queutey, M. Visonneau, T. Hino, and K. Ohashi.(2011) Free-surface viscous flow solution methods for ship hydrodynamics. *Archives of Computational Methods in Engineering*, 18:1–41.

[53] Yoo, S. O., Kim, T., & Kim, H. J. (2020). "A numerical study to predict added resistance of ships in irregular waves". *International Journal of Offshore and Polar Engineering*, 30(2), 161–170.

[54] Yoshida, J., Wang, X., Ohtaki, M., & Kashiwagi, M. (2016). Nonlinear effects on ship motions Date deposited : Nonlinear Effects on Ship Motions and Added Resistance in Large-amplitude Waves. March 2016, 0–8.

[55] Zhang, H. D., & Guedes Soares, C. (2016). Modified joint distribution of wave heights and periods. China *Ocean Engineering*, 30(3), 359–374

[56] Zhang, H. D., Cherneva, Z. and Guedes Soares, C., 2013b. Joint distributions of wave height and period in laboratory generated nonlinear sea states, *Ocean Eng.*, 74, 72–80.

[57] Ochi M K and Motter E 1974 Prediction of extreme ship responses in rough seas of the *North Atlantic Naval Ship Research and Development Center Ship Performance Department* Bethesda USA Paper No 20 pp 199-209

[58] Umeda N, Usada, S, Mizumoto, K and Matsuda A 2016 Broaching probability for a ship in irregular stern-quartering waves theoretical prediction and experimental validation *J Mar Sci Technology* 21 pp 23- 37

Publication List

Please refer to https://www.researchgate.net/profile/Sahil-Jawa

Journal Publication

Jawa, S., & Munehiko, M. (2023). Validation of short-term prediction of added resistance in head seas considering wave steepness nonlinearity with probability density function method. *Ocean Engineering*, Vol. 278, No. 14353.
https://doi.org/10.1016/j.oceaneng.2023.114353

Proceedings in International Conference

i. Jawa, S., Minoura, M., & Idomoto, Y. (2022). Short-Term Prediction of Nonlinear Added Resistance in Head Sea with Probability Density Function Method. *In The 32nd International Ocean and Polar Engineering Conference* (p. ISOPE-I-22-508).

ii. Jawa, S., Munehiko, M. (2023). Short-Term Prediction of Added Resistance in Oblique Seas Considering Wave Steepness Nonlinearity with Probability Density Function Method. In *The 33rd International Ocean and Polar Engineering Conference* (p. ISOPE-I-23-172).